STATE OF CALIFORNIA • DEPARTMENT OF TRANSPORTATION

TECHNICAL REPORT DOCUMENTATION PAGE

TR-0003 (REV 04/2024)

1. REPORT NUMBER	2. GOVERNMENT ASSOCIATION NUMBER	3. RECIPIENT'S CATALOG NUMBER
CA 25-3303		UCD 25-101

4. TITLE AND SUBTITLE	5. REPORT DATE
ASSESSMENT AND SHEAR STRENGTHENING OF EXISTING CAST-IN-PLACE AND PRECAST CONCRETE BRIDGE GIRDERS	01/21/2025
	6. PERFORMING ORGANIZATION CODE

7. AUTHOR	8. PERFORMING ORGANIZATION REPORT NO.
B. Grayson-Wallace, A. Aljasar, E. Vasquez, S. K. Kunnath, L. Cheng, J. Bolander	UCD 25-101

9. PERFORMING ORGANIZATION NAME AND ADDRESS	10. WORK UNIT NUMBER
University of California One Shields Ave. Davis, CA 95616	
	11. CONTRACT OR GRANT NUMBER 65A0732

12. SPONSORING AGENCY AND ADDRESS	13. TYPE OF REPORT AND PERIOD COVERED
California Department of Transportation Sacramento, CA 95819	Final Report (2019 - 2023)
	14. SPONSORING AGENCY CODE

15. SUPPLEMENTARY NOTES

16. ABSTRACT

This research study investigated the feasibility of two shear-strengthening techniques to assess their effectiveness in enhancing the shear capacity of existing reinforced concrete girder bridges. The first scheme consisted of using Near-Surface-Mounted (NSM) bars while the second scheme comprised Partially Embedded Bars (PEB) in the web of the girder. First, a preliminary series of pull-out tests were carried out to examine various options to enhance the anchorage and/or bond of the NSM bars and PEB to the existing concrete. In the case of the NSM approach, none of the anchorage improvement techniques resulted in significant strength gain. For PEB, specimens with sand-coated CFRP bars bonded with the epoxy performed better than the specimens with other strengthening materials. Next, a finite element (FE) study was carried out using the commercial software ATENA to investigate the two strengthening schemes. The model was validated by comparing the simulated response to the findings from the control tests. The validated model was then used to predict the shear enhancement due to the two proposed strengthening schemes. The experimental program comprised three-point load bending tests to failure of full-scale RC T cross-section girders strengthened in shear using the two strengthening schemes. Findings from the experimental study indicate that NSM is not likely to be effective for large-scale girders where 3D effects cause failure to occur locally due to local side cover detachment. Results from the next phase of testing demonstrated that the PEB method is an effective shear-strengthening technique. An increase of 53% and 30% was observed in the shear capacity of the strengthened specimen compared to the control specimen. Hence, it is recommended that shear-deficient reinforced concrete girders be strengthened with partially embedded bars as added shear reinforcement.

17. KEY WORDS	18. DISTRIBUTION STATEMENT
CFRP Bars, Large-Scale Testing, RC Girder, Shear Strengthening	No restrictions

19. SECURITY CLASSIFICATION *(of this report)*	20. NUMBER OF PAGES	21. COST OF REPORT CHARGED
Unclassified	129	

DISCLAIMER STATEMENT

This document is disseminated in the interest of information exchange. The contents of this report reflect the views of the authors who are responsible for the facts and accuracy of the data presented herein. The contents do not necessarily reflect the official views or policies of the State of California or the Federal Highway Administration. This publication does not constitute a standard, specification or regulation. This report does not constitute an endorsement by the Department of any product described herein.

For individuals with sensory disabilities, this document is available in alternate formats. For information, call (916) 654-8899, TTY 711, or write to California Department of Transportation, Division of Research, Innovation and System Information, MS-83, P.O. Box 942873, Sacramento, CA 94273-0001.

ASSESSMENT AND SHEAR STRENGTHENING OF EXISTING CAST-IN-PLACE AND PRECAST CONCRETE BRIDGE GIRDERS

A Technical Report Submitted to the California Department of Transportation
under Contract 65A0732

Ahmed Aljasar, Brendan Grayson-Wallace and Emmanuel Vasquez
Graduate Student Researchers
Sashi Kunnath, Dawn Cheng and John Bolander
Professors of Structural Engineering

January 2025

Department of Civil and Environmental Engineering
Structural Engineering and Structural Mechanics
University of California at Davis

Abstract

This research study investigated the feasibility of two shear-strengthening techniques to assess their effectiveness in enhancing the shear capacity of existing reinforced concrete girder bridges. The first scheme consisted of using Near-Surface-Mounted (NSM) bars while the second scheme comprised Partially Embedded Bars (PEB) in the web of the girder. Whereas the NSM approach is an existing method with numerous applications in strengthening of structural components, PEB is a variation of an existing method referred to as Embedded Through Section (ETS). In the proposed PEB method, shear strengthening is achieved by inserting steel or FRP bars into holes bored through the partial depth of the girder web and then bonded with an epoxy adhesive.

Prior to load testing using the two strengthening schemes, a preliminary series of pull-out tests were carried out to examine various options to enhance the anchorage and/or bond of the NSM bars and PEB to the existing concrete. In the case of the NSM approach, the anchorage methods selected from the literature were: providing a T-anchor at bar ends, introducing multiple horizontal grooves filled with epoxy, and extending the FRP bar into the top flange of the girder. Results of the pull-out tests showed that none of the approaches resulted in significant strength gain to be recommended as a viable enhancement to the bond properties. For PEB, the pull-out test campaign comprised thirty rectangular concrete blocks with embedded uncoated traditional Steel (Grade 60 ksi), uncoated High Strength Steel (HSS) Grade 80 ksi, and sand-coated and smooth carbon fiber reinforced polymer (CFRP) bars bonded with either epoxy or grout. Findings from the testing revealed that the specimens with sand-coated CFRP bars bonded with the epoxy performed remarkably better than the specimens with other strengthening materials.

Next, a finite element (FE) study was carried out to investigate the two strengthening schemes and gain insight into the potential shear enhancement resulting from using NSM and PEB. The commercial software ATENA software was utilized in this study since it was developed to specifically simulate the behavior of reinforced concrete structures including concrete cracking, crushing, and reinforcement yielding. Another feature of the software that was also appealing for the present study was the ability to model reinforcing steel and CFRP bars as discrete bars. A detailed model of the specimen was developed using 3D continuum elements for

concrete and discrete truss elements for both steel and FRP bars. The model was validated by comparing the simulated response to the findings from the control tests. The validated model was then used to predict the shear enhancement due to the two proposed strengthening schemes.

An experimental program comprised of three-point bending tests to failure of full-scale RC girders with T cross-sections strengthened in shear using the two strengthening schemes was carried out. In all, three NSM tests were carried out: the first two tests using #4 CFRP bars spaced at 10 inches center-to-center, and the third test with #4 CFRP bars at 5 inches on center. While the first test had #3 grade 40 stirrups at 10 inches, the remaining two tests utilized #4 Grade 60 stirrups. Of the three tests, the first test produced the best results with a shear capacity gain of about 25% whereas the phase II tests had negligible shear enhancement. Findings from the phase II study indicate that NSM is not likely to be effective for large-scale girders where 3D effects cause failure to occur locally due to local side cover detachment.

The girders strengthened in shear with the PEB technique utilized CFRP bars and epoxy adhesive using two options. The primary goal of the first option was to evaluate the effectiveness of the PEB method as a shear-strengthening technique, whereas the second option investigated the effect of increasing the shear reinforcement ratio on the shear capacity gain associated with employing the PEB method. Results from the two tests demonstrated that the PEB method is an effective shear-strengthening technique. An increase of 53% and 30% was observed in the shear capacity of the strengthened specimen compared to the control specimen.

Based on the findings from the experimental study, it is recommended that shear-deficient reinforced concrete girders be strengthened with partially embedded bars as added shear reinforcement. An approximate procedure is proposed to determine the shear enhancement using PEB but additional testing and associated numerical studies are needed to improve the proposed expression.

Acknowledgments

This research was funded by the California Department of Transportation under Contract No. 65A0732. The UCD Research Team extends their sincere thanks to Caltrans Project Managers Pat Hipley, Alaoua Kartoum and Foued Zayati and Project Consultant Abdeldjelil Belarbi for their input and assistance throughout the project.

Table of Contents

List of Figures

List of Tables

1.0 INTRODUCTION

1.1 Background

It is estimated that several hundred bridges on major state highways in California are structurally inadequate to carry many of the permit loads that are routinely requested for transport on Caltrans roadways. This results in time consuming and costly detours for many vehicles carrying these loads. Most of these deficient bridges have pre-cast concrete "T", "I" or cast-in-place concrete box girder superstructures. They are primarily deficient in shear in terms of their ability to carry permit loads. One of the goals of Caltrans is to strengthen all of these bridges to adequately carry AASHTO LRFD "P-15" loading. There is presently no design or construction procedure to increase shear capacity (through retrofit) of typical girders found in the majority of Caltrans bridges. The only alternatives available at this time are complete bridge replacement or possibly the replacement of the superstructure only. Both of these alternatives are costly, time consuming and disruptive to the traveling public and the transportation of goods.

Many methods have been proposed by various researchers for shear strengthening of reinforced concrete girders. However, it is necessary to carefully assess the pros and cons of each approach and to select methods that are suitable for California bridges. A review of some of the available methods is discussed in this section and a plan for assessing feasible solutions is proposed through analysis and experimental testing.

1.2 Shear Strengthening Schemes

Traditional techniques for shear strengthening of concrete bridge girders include the uses of external supplemental steel stirrups, concrete section enlargement, and externally bolted steel plates. Other shear strengthening techniques involve the application of prestressing technologies or the use of novel reinforcing materials, such as fiber reinforced polymer (FRP) composites and shape memory alloys (SMAs). The relative advantages of a given technique depend on the bridge configuration (e.g., I-/T-girders versus closed-cell box girders) and project specific

constraints. Factors that influence the choice of strengthening technique include strengthening efficiency, constructability, speed of construction, material and labor costs, risk of damage to existing girders, impact on traffic, durability and maintenance requirements, effects on superstructure dead load and vertical clearance of the bridge, and impact on girder inspection over the remaining service life of the bridge. An extensive literature survey on shear strengthening schemes was conducted and the findings published in a peer-reviewed journal (Grayson-Wallace et al. 2022).

The FRP-based near-surface mounted (NSM) strengthening technique gained interest among researchers starting in the early 2000's. This method uses prefabricated FRP rods (circular or square cross section) or strips (rectangular cross section) as additional open stirrups by adhering them to the beam web in shallow grooves as shown in Figure 1. The existing FRP rods or strips are typically 6 mm to 12 mm (diameter or width) and the grooves approximately twice the size of the reinforcement, as illustrated in Figure 1.1. The NSM technique has been shown to delay or prevent debonding failure (a known issue with Externally Bonded FRP strips) and achieve higher capacities with less material and also exhibit more dispersed shear crack patterns.

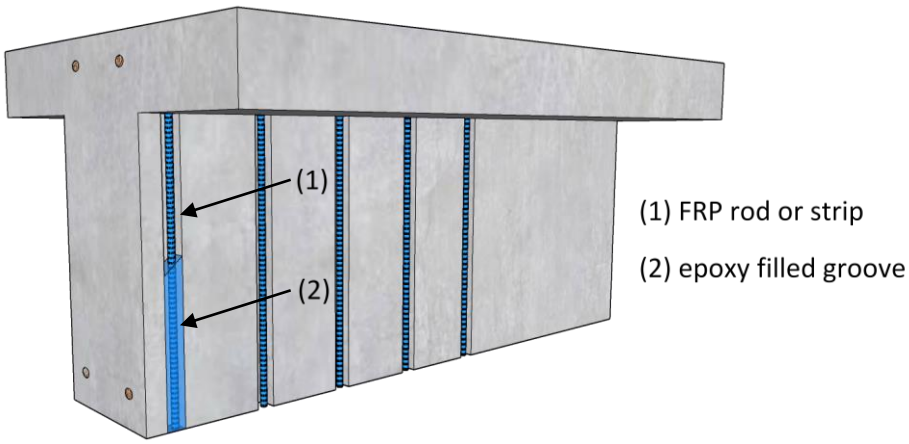

Figure 1.1 Near-Surface-Mounted (NSM) FRP Bars

A second strengthening scheme considered in the study is embedding bars through the web of the section as shown in Figure 1.2. Shear strengthening, through this technique, is achieved

through the insertion of steel (or FRP) bars into holes bored through the web and then bonded with an epoxy adhesive.

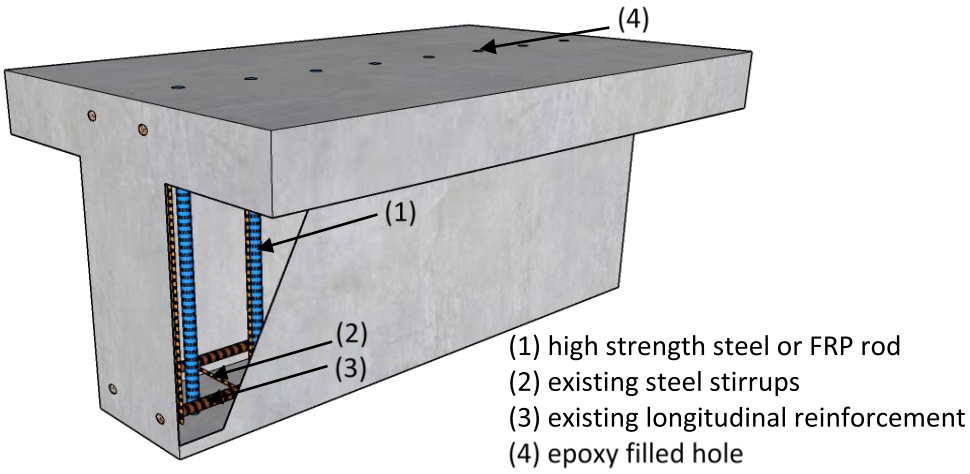

Figure 1.2 Partially Embedded Bar (PEB) through Web

This method requires the use of non-destructive tools to identify and mark the locations of existing longitudinal and transverse reinforcement along the span of the girder within its centerline. Then either a water-based concrete coring machine or a dry system with vacuum attachment is used to drill holes at the selected locations where the steel (or FRP bars) will be embedded. The holes are typically vertical but can also be oriented at any angle (e.g., 45 degrees) and drilled through the entire depth of the girder. After the bar is embedded, the drilled hole is filled with epoxy to assure bonding between the newly inserted steel (or FRP) rebar and the surrounding concrete.

The ETS approach has several advantages compared to other shear strengthening methods – it provides a strong mechanical connection, does not require anchorage, is less prone to corrosion issues, is relatively a lower-weight solution, has no impact on vertical clearance of the bridge, and does not impede bridge inspection. It will be necessary for sections of the wearing surface to be removed if the drilling & installation is done from the deck surface which will impact traffic. Drilling can also result in accidental damage to existing reinforcement.

1.3 Objectives and Scope of Study

The primary objective of the proposed research is to assess the feasibility of two shear-strengthening techniques and to evaluate their effectiveness in enhancing the shear capacity of existing reinforced concrete bridges. The research objectives will be achieved through the following series of tasks:

(a) Selection of prototype bridge – This task is critical to the project since the goal is to test a specimen whose depth represents either a full-scale or near full-scale bridge girder. The effects of using a scaled model in the context of investigating shear capacity is not fully known. Once a prototype bridge is identified, the development of an appropriate test specimen should consider a configuration that induces shear failure prior to flexural yielding of the specimen.

(b) Selection of strengthening materials and anchorage schemes – Whereas with NSM, only FRP bars are to be used, in the case of partially embedded bars (PEB) both steel and FRP are available options. Additionally, the choice of the bonding material is important. Hence a preliminary set of pull-out tests were carried out to establish the most suitable anchorage scheme (for NSM) and bar material and bonding agent for PEB.

(c) Design of the experimental setup – Considering the physical constraints in the laboratory, it is essential that the test of the selected prototype bridge girder can be accomplished wherein the girder fails under the imposed shear. This task includes the design of the reaction system subjected to the limitations of the strong floor in the laboratory.

(d) Numerical studies – A finite element (FE) model of the specimen to be tested will be developed using a commercial software. The FE model will be first validated with control

tests (unstrengthened specimens in Phase I testing) and these models will be used to predict the shear enhancement provided by the proposed strengthening schemes.

(e) Control tests – This will comprise two control tests, one for each batch of concrete. The shear capacity of the unstrengthened girders will be established through this phase of testing.

(f) Strengthening Scheme I – This will include tests of the first strengthening scheme utilizing the Near-Surface-Mounted (NSM)) method. A total of three tests will be carried out to investigate two variables, described later in the report.

(g) Strengthening Scheme II – This will include tests of the second strengthening scheme utilizing partially embedded bars in the web of the girder. Two tests will be carried out to investigate the effect of existing stirrups on the shear enhancement.

2.0 PRELIMINARY PULL-OUT TESTING

One of the issues related to Near-Surface-Mounted (NSM) bars is the anchorage of the FRP bars to the existing concrete. Hence, project investigators decided to consider possible schemes to enhance the bond and anchorage of the FRP bars. Prior to selecting a scheme for the large-scale testing, it was deemed necessary to conduct preliminary pull-out tests to examine the effectiveness of each anchorage scheme. Likewise, when using the partially embedded bars in the web of the girder, several options exist – both in terms of the material type (steel or FRP) and the type of epoxy to be used to anchor the bar into the girder. As with the investigation of the anchorage using pull-out tests, it was decided that direct pull-out tests using different bar types and different epoxy material be carried out to determine the most effective strengthening option.

2.1 Near-Surface-Mounted FRP Bars

The key issue targeted by this testing is whether additional bond capacity can be gained by the inclusion of anchorage. The anchorage methods selected from the literature for testing are: providing a T-anchor at bar ends; introducing multiple horizontal grooves filled with epoxy; and extending the FRP bar into the top flange of the girder. Within each method, several variations were tested to gain a basic understanding of each method's controlling factors. Details of the different enhancement schemes and results of the pull-out tests are outlined in the next section.

2.1.1 Specimen Details

The experimental setup was consistent with previous work conducted at UC Davis as well as papers in the literature. 18 of the 24 blocks were rectangular with dimensions of 13.78 x 11.81 in. with a thickness of 5.91 in. The remaining 6 blocks were modified to an L-shape to include a 5.91 x 5.91 x 11.81 in. flange section. Previous work at UC Davis has shown that sand-coated, spirally wound CFRP rods attained consistent and favorable results, so they were selected for this experiment as well. Normal-strength concrete with a specified 28-day concrete compressive strength of 4,000 psi was used which resulted in an average concrete strength of 5,000 psi over the duration of testing which was reasonably consistent with the concrete to be used in the girder

testing. The grooves were cut in the long direction (13.78 in) to allow for the bonded length to be varied from 5.91 in. to 9.84 in while maintaining adequate edge distance. The bar diameter selected was 3/8 in, and the groove size was set at twice the bar diameter based on the work of Lee and Cheng (2013). Testing done at UC Davis by Wang and Cheng (2021) showed that a 3-part epoxy was very effective for NSM reinforcement, so Magmaflo CF 3-part epoxy was selected for this study. Details of the pull-out specimens are listed in Table 2.1 and schematic drawings of each anchorage type is shown in Figure 2.1.

Table 2.1: Pull-out Tests – specimen details

Label	*Bond Length (in)*	*Anchor Type*	*Variable/Detail*
C-9.8	9.84	-	
C-5.9	5.91	-	
PC-9.8	9.84	-	Precast groove
L-9.8-2.0	9.84	Flange (1.97 in embed)	Anchor type, bond length
L-9.8-3.1	9.84	Flange (3.15 in embed)	Anchor type, bond length Anchor type & length
L-5.9-2.0	5.91	Flange (1.97 in embed)	Bond length
T-F	9.84	T – loose fibers	
T-P	9.84	T – dowel	Anchor type
R-2-6.7	9.84	Ribbed (2 @ s=6.7)	Anchor type, rib quantity
R-3-4.1	9.84	Ribbed (3 @ s = 4.1)	Anchor type, rib spacing
R-3-3.0	9.84	Ribbed (3 @ s = 3.0)	Anchor type, rib spacing
PR-2-6.7	9.84	Ribbed (2 @ s = 6.7)	Anchor type, precast

The sand-coated, spirally wound CFRP rods used were from the Aslan 200 series. Its material properties were previously determined by (Wang and Cheng 2021), from their work the rods were tested to have an elastic modulus of 18700 ksi, an ultimate tensile strength of 344 ksi (with standard deviation of 12.12), and an ultimate tensile strain of 1.84%. The three-part epoxy (resin, curing agent, aggregate) used was Magmaflo CF by Pilgrim, and according to the manufacturer it has a shear strength of 7.6 ksi, a tensile strength of 2.15 ksi, a compressive 17.7 ksi, and an elastic modulus of 1800 ksi.

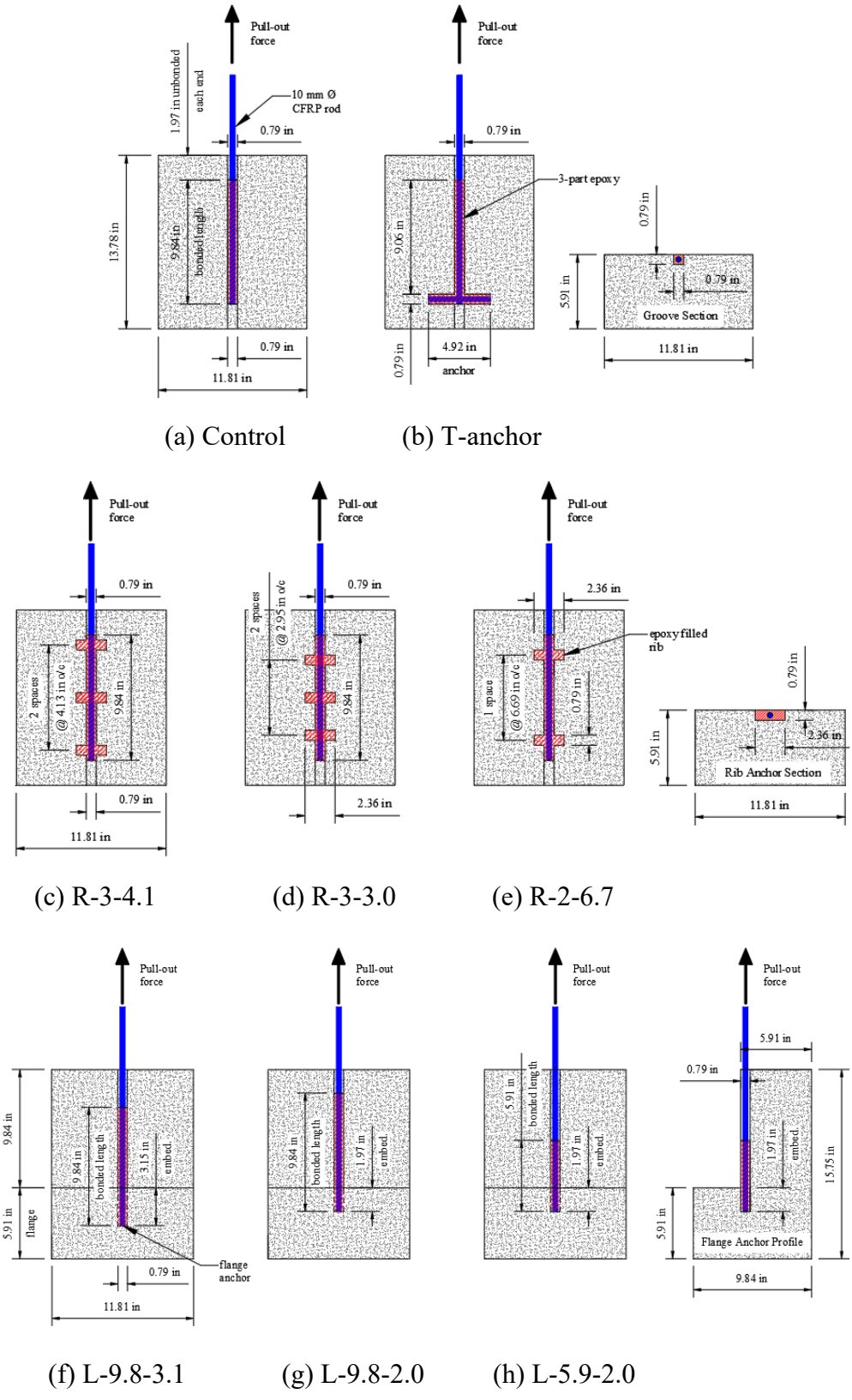

(a) Control (b) T-anchor

(c) R-3-4.1 (d) R-3-3.0 (e) R-2-6.7

(f) L-9.8-3.1 (g) L-9.8-2.0 (h) L-5.9-2.0

Figure 2. 1: Schematic drawings of NSM anchors

The concrete was poured in one batch. The design 28-day strength was 4,000 psi and the day-of compressive strength was about 5,000 psi. The concrete was formed as blocks in one batch and grooves were cut after 14 days of curing. The grooves were cut with a multi-blade circular saw similar to a dado blade. This saw allowed for very accurate and consistent width and depth to be achieved on all straight grooves. The grooves were extended to the full length of the blocks, except in the case of the L-blocks. For the shorter transverse portions of the T-anchors and ribbed groove blocks, an electric hammer chisel and hand chisel were used. The partial depth flange anchors were cut with an 18 in. long, 3/4 in. diameter impact drill bit held inside of and parallel to the groove to drill the embedded section of groove. The precast grooves were formed using 3/4 in. square wooden strips nailed and glued into the forms to mimic the geometry of the corresponding cut groove specimens.

There are no commercially available T-anchors for NSM CFRP to the best of the author's knowledge. To form the T-shapes, two different approaches were tested. The first was to use a wood dowel to create the top of the T (specimen T-P) and then wrapping loose FRP strips around it to bond it to the straight rod. The second was to not use a dowel and lay the FRP strips directly into the grooves (specimen T-F). Figure 2.2 shows how both methods were fabricated. The strain gages limited the bond length between the rod and the FRP strips. The rod was cleaned with a stiff brush and alcohol to remove debris, but the sand-coating was not removed. Then the FRP strips and the rod were coated with a conventional wet lay-up epoxy. The strips were then wrapped around the rod. For the doweled T-shape the last step was to wrap the strips around the dowel as shown in Figure 2.2 b.

Prior to installation, the grooves were cleaned with a wire brush, flushed with water, and then dried/dusted with compressed air. Then the bonded lengths were blocked off with plumbers putty to prevent the epoxy from spilling out of the designed length. Next, the grooves were filled halfway with epoxy and the rods were pressed in while gently moving them back and forth to prevent air pockets from forming beneath them. The grooves were then filled level with the surface of the concrete. The L-shaped blocks had mostly the same procedure, but for filling the hole inside the corner the second lift of epoxy was troweled in and the block was vibrated with a rubber mallet to settle the epoxy.

a) b) c) d)

Figure 2. 2: T-anchor fabrication: (a) wood dowel for T-shape; (b) wrapping FRP strips around dowel; (c) finished doweled-T; (d) loose fiber version

2.1.2 Results of Testing

The pullout tests were conducted in a typical tensile loading frame. The NSM bars were extended 3 feet beyond the end of the block and encased in a steel pipe to ensure the FRP was not crushed by the loading grips. Since NSM is embedded in the surface of the block, there is some eccentricity introduced which slightly bends the rods. To counteract this, four steel rods were used to restrain the blocks from flexing in the out of plane direction. The concrete block was hung by the NSM rod and the load was resisted by two C channels supporting the top face of the concrete, creating a compression support. The test frame is shown in figure 2.3 below, with a schematic view of the loading in Figure 2.3 (b). The free end (end opposite loading) slip of the bar was measured using an LVDT in contact with the end of the bar. Each bar had 4 strain gauges spaced at equal distances along its bonded length to calculate the average slip for each segment of the bar. In addition to the slip and strain, the load was collected using a National Instruments (NI) data acquisition system with LABVIEW software at a sampling rate of 200 Hz for all data channels.

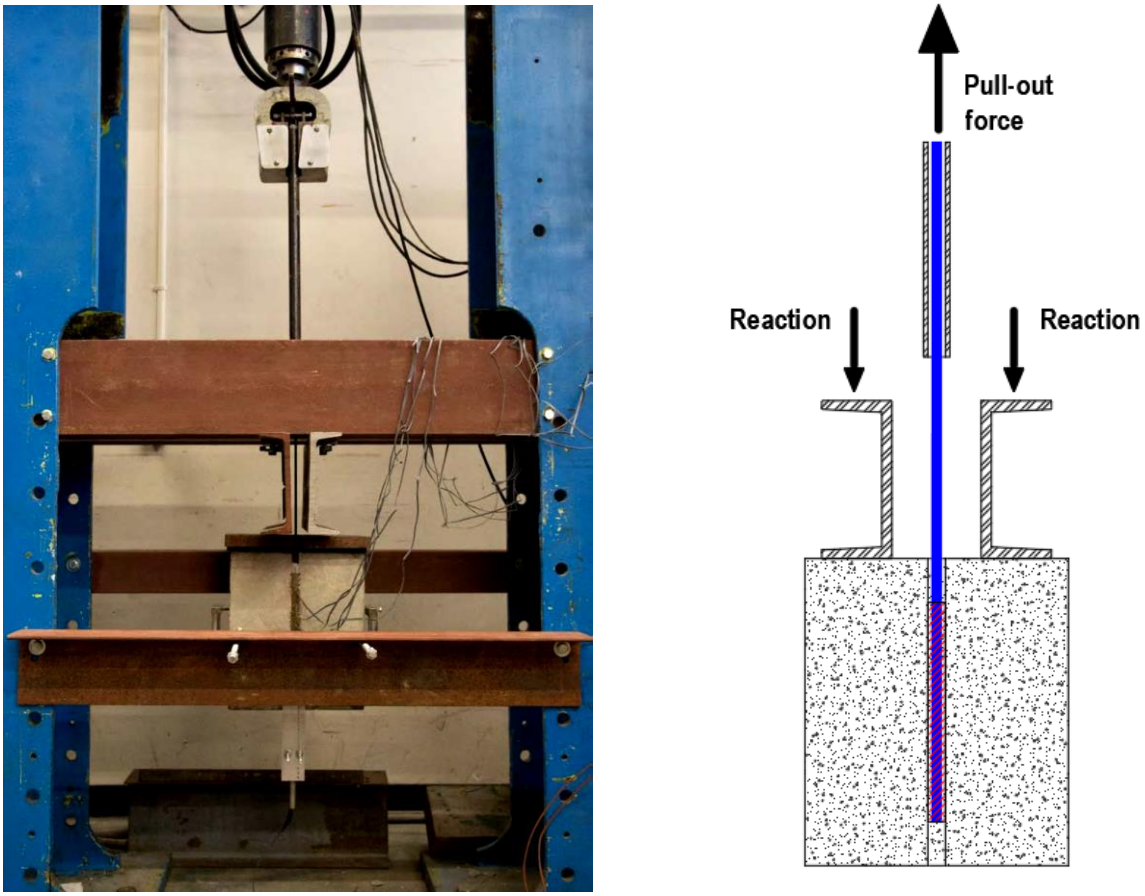

(a) Testing frame (b) Loading schematic

Figure 2.3: Set-up for pull-out testing

The 24 test specimens were labeled according to their test parameters. The first letter refers to the test group: C for control, P for precast, R for ribbed, L for L-shaped block, and T for T-anchor. The second term refers to the bonded length, number of ribs, or type of T fabrication. The third term for the ribs and L refers to either the rib spacing or flange embedment. It is worth noting that the main focus of the presented experimental program was to evaluate the effectiveness of the available strengthening materials (reinforcing bar and bonding agents) and not to assess the local bond law and its dependence on the investigated parameters. Thus, the influence of the parameters analyzed was restricted to the average bond stress which is defined as:

$$\tau = \frac{P}{\pi d_b l_b} \tag{2.1}$$

where P is the pull-out force, d_b is the bar diameter and l_b is the embedded length of the bar. In the equation above the average bond stress is assumed to be constant along the embedded length (which is not entirely accurate due to the non-uniform variation of bond stresses along the embedded length). A summary of the pullout forces and stresses from each set are listed in Table 2.2 and an example of each failure mode is in Figure 2.4 below.

Table 2.2: Results of pull-out testing

Specimen/Set	Pmax (kip)	Slip (in)	τ_{max} (ksi)	Failure Mode
C-9.8	20.1	0.0573	3.29	EP/CC
PC-9.8	17.2	0.1340	2.51	EP/CC*
PR-2-6.7	18.7	0.0398	3.41	EP/CC, ES
R-2-6.7	18.3	0.2362	3.41	EP/CC, ES, DB*
R-3-4.1	16.6	0.0738	2.92	EP/CC, ES, DB
R-3-3.0	21.2	0.0817	3.95	EP/CC, ES
T-P	17.5	0.1528	3.25	EP/CC, ES
T-F	17.3	0.0531	3.51	ES, EP/CC
L-9.8-2.0	19.0	0.0470	2.76	DB, ES
L-9.8-3.1	19.5	0.0522	2.04	EP/CC, ES, DB
C-5.9	11.0	0.0212	2.87	DB
L-5.9-2.0	9.4	0.0232	2.06	DB

Notes: ES: Epoxy splitting (marked by a longitudinal crack parallel to bond length); EP/CC: Cohesive concrete and epoxy failure; DB: Debonding of FRP bar from epoxy.
* indicates a defective bar where sand coating caused premature debonding.

The pullout tests had mixed results, with no method causing a significant increase in the capacity of the NSM bars. The precast grooves, though not common for NSM applications, did not have a significant effect on the performance of the NSM method. The lower average pullout force (P_{max}) of the PC-9.8 series is explained by a low-quality sand coating causing premature debonding of one of those tests. The T-anchors by contrast, had a negative effect on the pullout force. This was likely due to the strain gauges limiting the bonded length between the wet lay-up and the CFRP rods. If the fabric and rod bond was not fully developed due to its short length,

then there was insufficient load transfer between the rod and the epoxy groove filler which effectively reduced the bonded length of the NSM. There was high variability in the ribbed specimen pullout forces, with R-2-6.7-a and R-3-3.0-b producing the highest pullout forces of any tests, but the other ribbed tests had significantly lower results. There was another CFRP rod with minimal sand coating that caused premature debonding of one of the specimens, but even discounting that test, the increase in shear capacity was too small (<20% increase) to justify the ribbed method as a viable anchorage method. Lastly, the L-shaped blocks were designed to test partial depth flange anchors, as full depth anchors have already been shown to be effective in the literature. The presence of the flange did influence the failure mode, by changing from an epoxy concrete cohesive failure to a more debonding controlled failure. The pullout forces of the L-shaped blocks were lower than the controls, but that was most likely due to voids in the anchored portion. One of the L-9.8 blocks was cut in half after testing and several air pockets were found in the anchored section meaning the anchored section was not fully bonded.

(a) (b) (c)

(d) (e) (f)

Figure 2.4: Typical failure modes – (a) Control (EP/CC); (b) Precast groove (EP/CC & DB); (c) R-2-170 (ES & DB); (d) R-3-105 (DB & ES); (e) R-3-75 (EP/CC & ES); (f) T-anchor (DB, EP/CC & ES)

Figure 2.5 presents the bond force-slip relationships obtained for a specimen from each of the different sets. Sections of horizontal slips are generally indicative of a local failure, either debonding or a cohesive failure, which precedes a total loss of strength. In the cases where the epoxy remains intact, there can be some bond friction that provides a small amount of residual capacity, but most of these specimens suffered significant epoxy damage. The observed bond force-slip patterns agree reasonably well with findings reported in existing literature.

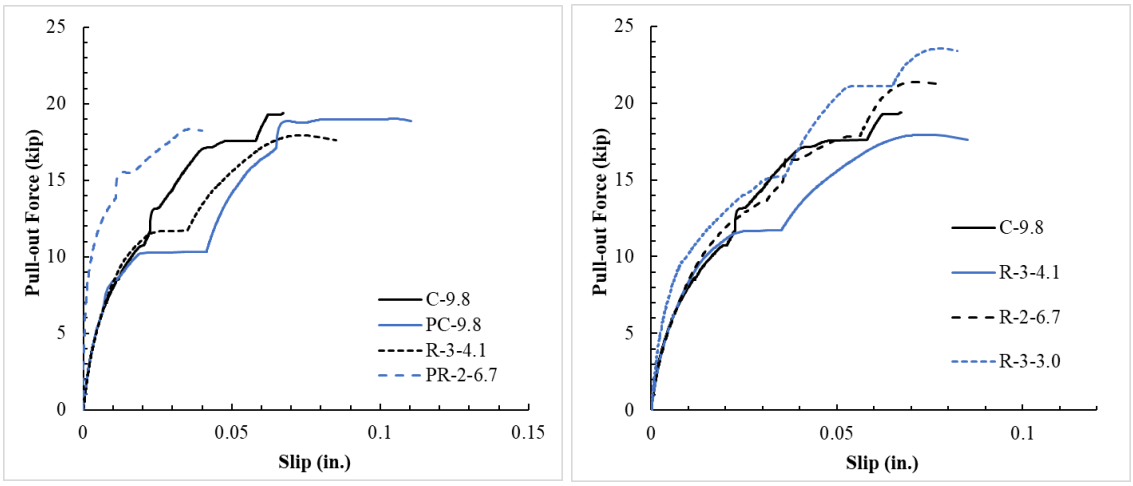

(a) (b)

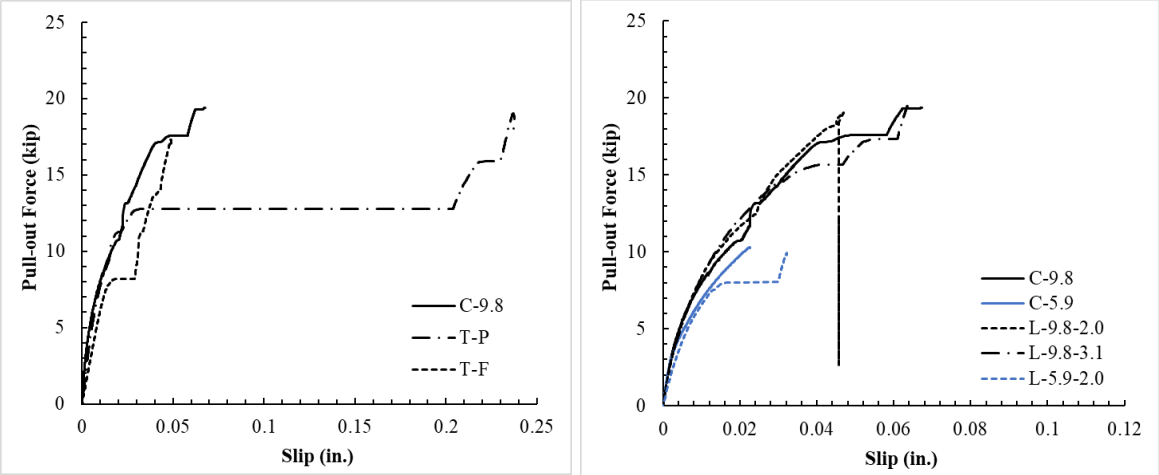

(c) (d)

Figure 2.5: Bond-slip relationships for tested bars: (a) precast grooves; (b) ribbed anchors, (c) T-anchors, (d) partial depth flange anchors

Findings from the pull-out testing can be summarized as follows:

- The use of precast grooves in lieu of cut grooves did not have a significant effect on the bond performance.
- The T-anchors had consistently lower pullout forces then the control. This was due to debonding between the rod and end anchor segments, as the bond length was limited by the presence of strain gages.
- The flange anchors had pullout forces similar to the controls but were effective at redistributing the shear stresses along the bond length.
- The ribbed anchors showed the best results, however, the average increase was not significant enough to be recommended as a viable enhancement to the bond properties

2.2 Partially Embedded Bars

As previously stated, the main purpose of this experimental program is to evaluate the effectiveness of different candidate bars and bonding materials to be used in large-scale testing later. With that in mind and given the available test data in the literature, many of the controlling parameters (e.g., concrete compressive strength, f_c', bar and hole diameter, and the embedment

depth), which have a direct influence on the bond behavior between the tested bars and surrounding concrete were kept constants for all the tested specimens. Thus, the variables investigated in this laboratory study included only the following: bar material (e.g., steel grade (strength) and carbon fiber-reinforced polymer (CFRP) with different surface coating) and bonding material (e.g., chemical adhesive or cementitious grout). In all, thirty rectangular concrete blocks (comprising ten variables and three specimens each) with embedded steel and CFRP bars were tested. Specimen preparation, materials used, bars and bonding materials, and test setup and instrumentation are outlined in the next section.

2.2.1 Specimen Preparation and Details

The cross-sectional dimensions of the concrete blocks were 6.0 in. x 6.0 in. with a depth of 13.8 in. (corresponding to an unbonded length of 8.8 in. and a bonded length of 10 times the bar diameter). Normal-strength concrete with a specified 28-day concrete compressive strength of 4,000 psi was used which resulted in an average concrete strength of 5,000 psi over the duration of testing which was reasonably consistent with the concrete to be used in the girder testing. The hole diameter for the embedded bars was set at 1.5 times the bar diameter ($1.5d_b$). This is aligned with the AASHTO (2017), ACI 318 (2019), ACI 355.4 (2019), and Caltrans's Standard Specifications (2018) for an adhesive anchor (post-installed anchor with chemical adhesive). The #4 reinforcing bars with a 0.50 in. diameter were embedded 5.0 in. into concrete, which is ten times the bar diameter ($10d_b$). This embedment depth was within the acceptable range specified in ACI 355.4 and within the manufacturer's minimum and maximum values for embedment depth, which ranged from 2.75 to 10.0 in. for HILTI HIT-RE 500V3 epoxy and from 4.0 to 6.0 in. for SIKA AnchorFix 500 epoxy. Schematic drawings of the specimens are shown in Figure 2.6 and details of the pull-out specimens are listed in Table 2.3.

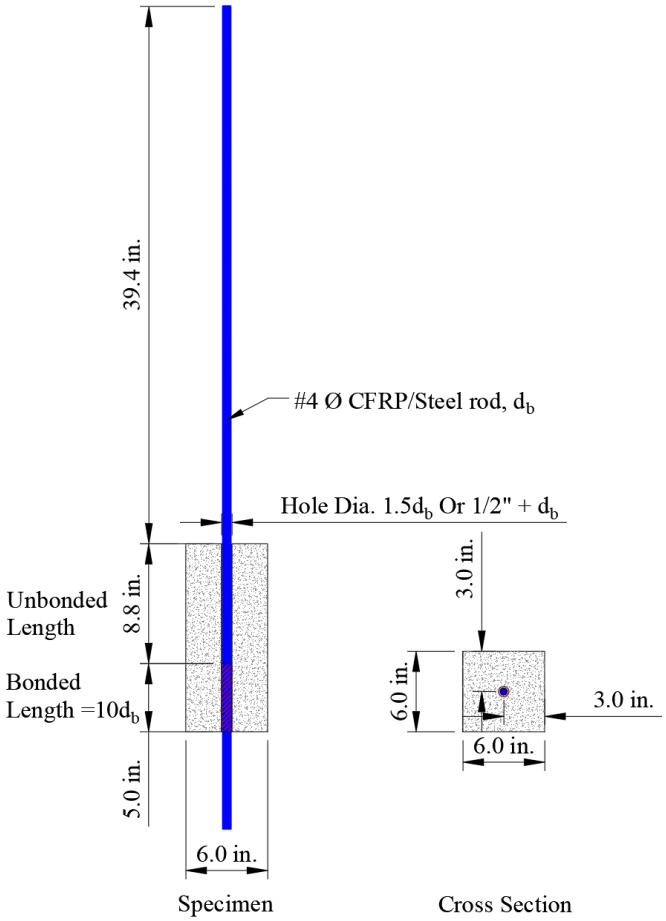

Figure 2.6: Dimensional details of pull-out specimen

Table 2.3: Specimen Details

Specimen Set	*Bar material*	*Adhesive material*
1	Grade 60 steel (Gr60)	
2	HSS Grade 80 (Gr80)	Epoxy: SIKA
3	CFRP – Smooth (SCFRP)	AnchorFix 500 (SIK)
4	CFRP - Sand-coated (SCCFRP)	

5	Grade 60 steel (Gr60)	MaterEmaco T 545DOT (MAS)
6	HSS Grade 80 (Gr80)	
7	Grade 60 steel (Gr60)	
8	HSS Grade 80 (Gr80)	Epoxy: HILTI
9	CFRP – Smooth (SCFRP)	HIT-RE 500V3 (HIT)
10	CFRP - Sand-coated (SCCFRP)	

Uniaxial tensile tests were carried out on the bars according to the standard procedures outlined in ASTM A370 (ASTM 2022) and ASTM D7205/D7205M (ASTM 2021) for the steel and CFRP bars, respectively. The stress-strain relationship for CFRP bars was essentially linear up to failure. Material properties obtained from the testing are summarized in Table 2.4. No testing was carried out on the bonding materials, instead the material properties of fully cured products reported by the manufacturers were assumed, as follows:

• Hilti HIT-RE 500 V3 epoxy had a bond strength, compressive strength, compressive modulus, tensile strength, and elongation at failure of 1.69 ksi, 12.0 ksi, 380 ksi, 7.15 ksi, and 1.1%, respectively.

• The SIKA AnchorFix 500 epoxy resin had a bond strength, compressive strength, and compressive modulus of 2.5 ksi, 10.0 ksi, and 400 ksi respectively.

• The MasterEmaco T 545DOT is a magnesium-phosphate patching and repair mortar that had a compressive strength, flexural strength, and bond strength of 5.20 ksi, 0.53 ksi, and 0.42 ksi respectively.

Undamaged blocks from the NSM pull-out specimens were chosen as test specimens for this study. At first, the concrete blocks were cut in half by using a concrete block saw, then a hole was drilled through the center of the concrete block across the entire length (14.00 in.) with a wet core drilling machine. Concrete blocks were inspected for local cracking or damage after the drilling process. The fabrication process of the specimens is illustrated in Figure 2.7.

Table 2.4: Properties of bars considered for strengthening

Bar Type	Bar Surface	Yield Strength (ksi)	Tensile Strength (ksi)	Elastic Modulus (ksi)	Ultimate Strain (%)
Steel Grade 60	Deformed	66.36	98.37	29000	15.64
Steel Grade 80	Deformed	87.85	118.14	29000	12.50
CFRP Sika Carbodur	Smooth	-	406	22500	1.80
CFRP Alson200	Sand Coated	-	300	18000	1.67

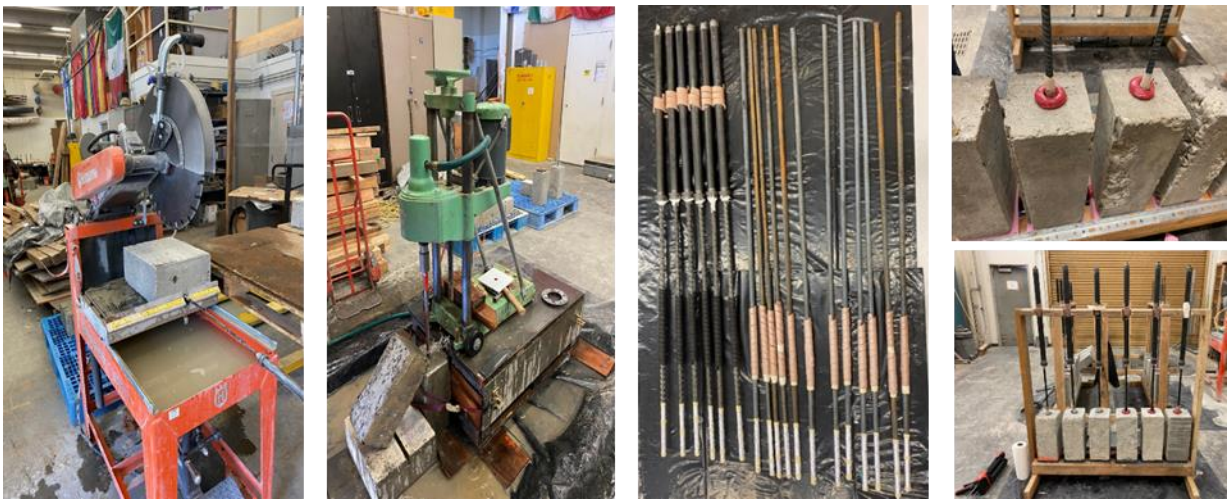

Figure 2.7: Specimen preparation

To ensure that the required embedded length ($5.0d_b$) of the bar inside the concrete is achieved, a high-density rubber foam weatherstrip tape was used to wrap the bar from the top of the concrete block to the point at which the embedment depth starts (see Fig. 2.7), thereby inhibiting any contact with the concrete, and providing the unbonded length. In addition, aluminum foil was placed on the bar starting at the bottom end of the concrete block and ending at the free end of the bar to ensure that any adhesive flowing down will not form an extra bond between the embedded bar and concrete. Furthermore, special consideration was given to the

sand-coated and smooth CFRP bars to prevent the potential slippage between the CFRP bars and the jaws of the Universal Testing Machine (UTM) and crushing the CFRP bars during the pull-out testing. CFRP bars were placed in steel tubes and a procedure outlined in ASTM D7205/D7205M (ASTM 2021) was followed.

Before the placement of bonding material and bar installation, the drill hole was cleaned using compressed air and the manufacturers' bonding material recommendations were followed. The bottom ends of the holes were blocked with tape to prevent leakage and work as a plug till the bar is penetrated through. Next, bonding material was placed to fill two-thirds of the hole. This quantity of bonding material ensured that there were no air voids at the bottom of the hole or surrounding the post-installed reinforcing bar. Afterward, the selected reinforcing bar was inserted vertically into the hole using a twisting motion to ensure that the chemical adhesive/mortar coated the entire surface area. The excess epoxy/mortar was removed from the top/bottom surface of the hole to ensure the correct bonded length. The specimens were cured for fourteen days at laboratory environmental conditions before testing.

2.2.2 Results of Testing

The test specimens were placed in a conventional tensile loading frame where the gripping end of the Steel/CFRP reinforcement bar was firmly clamped by a steel jaw, which is connected to the hydraulic jack with a built-in load cell. The load was applied in a displacement-control fashion. Two pairs of steel C channel sections were fixed on the loading frame and served as the reaction beam for the concrete block hanging below. A steel plate and rubber pad were placed between the steel C channel sections and the concrete block to ensure an evenly distributed compression force from the reaction beam to the concrete block. In addition, the concrete block was laterally supported by a pair of push bolts set at the front and back side of the concrete block to eliminate any eccentricity or torsion and ensure that only direct shear pull-out occurs (as shown in Fig. 2.8 a). A schematic view of the specimen in the testing frame is shown in Fig. 2.8 (b). A set of two linear variable differential transformers (LVDTs) was used to measure vertical displacements. The top LVDT measuring the elongation in the bar (Steel/CFRP) (see Fig. 2.8 c). The bottom LVDT was attached to the bar-free end and placed against the bottom of the concrete block to capture the relative displacement between the concrete block and Steel/CFRP

reinforcement, as presented in Fig. 2.8 (d). Experimental data including load, and displacement at the top and bottom ends were collected by using a National Instruments (NI) data acquisition system with the LABVIEW software, and the sampling rate was set as 200Hz for all the data channels.

(a) Testing frame

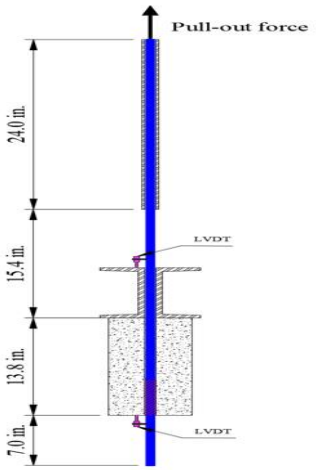

(b) Schematic view

(d) Top LVDT

(e) Bottom LVDT

Figure 2.8: Test setup

The thirty rectangular concrete blocks were divided into ten sets and each set contains three specimens that share the same bar and bonding material. The specimens were labeled to convey the parameters investigated and to facilitate understanding of the experimental results. Each specimen was labeled with two terms. The first term notes the bar material type, followed by a second term representing the used bonding material. Table 2.5 provides the peak pull-out force (e.g., pull-out capacity), slip at peak pull-out force, maximum average bond stress, and

failure mode for each tested set (reported numbers represent the average of the corresponding three specimens). It is worth noting that the main focus of the presented experimental program was to evaluate the available strengthening materials (reinforcing bar and bonding agents) options only with no intention to assess the local bond law and its dependence on the investigated parameters.

.

Table 2.5: Results of pull-out tests

Specimen/Set	P_{max} (kip)	Slip (in)	τ_{max} (ksi)	Failure Mode
Gr60-HIT	18.74	0.0012	2.39	Bar Yielded
Gr60-SIK	19.16	0.0031	2.44	Bar Yielded
Gr60-MAS	18.72	0.0004	2.38	Bar Yielded
Gr80-HIT	22.32	0.0074	2.84	Bar Rupture
Gr80-SIK	22.20	0.0116	2.83	Bar Rupture
Gr80-MAS	22.26	0.0010	2.83	Bar Rupture
SCCFRP-HIT	22.21	0.2024	2.83	Slip + Concrete Splitting
SCCFRP-SIK	25.12	0.1241	3.20	Slip + Concrete Splitting
SCFRP-HIT	2.30	0.0001	0.29	Bar Pull-out
SCFRP-SIK	2.44	1.1419	0.31	Bar Pull-out

In terms of the max pull-out or the average bond stress, specimens with either traditional steel (Grade 60) or high-strength steel (Grade 80) and sand-coated CFRP (SCCFRP) showed more consistent results regardless of the used bond materials. However, the specimens with the smooth CFRP (SCFRP) with either Sika AnchorFix 500 (SIK) or Hilti HIT-RE 500 V3 (HIT) epoxies showed poor performance as the bar deboned from the specimens with no signs of concrete cracking on the surface of the concrete blocks. This indicates that bar surface treatment has a direct effect on the bar/adhesive interaction and ultimately the bond strength, see Fig. 3.6 (c). As indicated in the table, different failure modes occur across the range of tested specimens.

Regardless of the bonding materials, specimens with either Grade 60, Grade 80, or SCCFRP exhibited excellent bar/adhesive and concrete/adhesive interactions: Specimens with Grade 60 failed as the bar yielded and specimens with Grade 80 failed as bar ruptured, in both cases the steel bars remained well attached to the concrete blocks with no visible cracks as shown in Fig. 3.6 (a). On the other hand, SCCRP specimens failed due to concrete splitting where a crack plane crossed the central hole and split the concrete block into two parts as illustrated in Fig. 3.6 (b). Even though the failure could be considered a brittle failure due to the tensile failure of the concrete, it resulted in a high pull-out force indicating that the bar/adhesive interaction was adequate to mobilize this force. In a real field application, the splitting of concrete is unlikely due to the presence of transverse and longitudinal reinforcement. Hence a decision was made to use sand-coated CFRP bars for shear strengthening since rupture of Grade 80 bars was a less desirable failure mechanism. Additionally, the bond length provided in the pullout testing was 10 d_b (5.0 in) whereas in field applications, the bond length will be significantly higher.

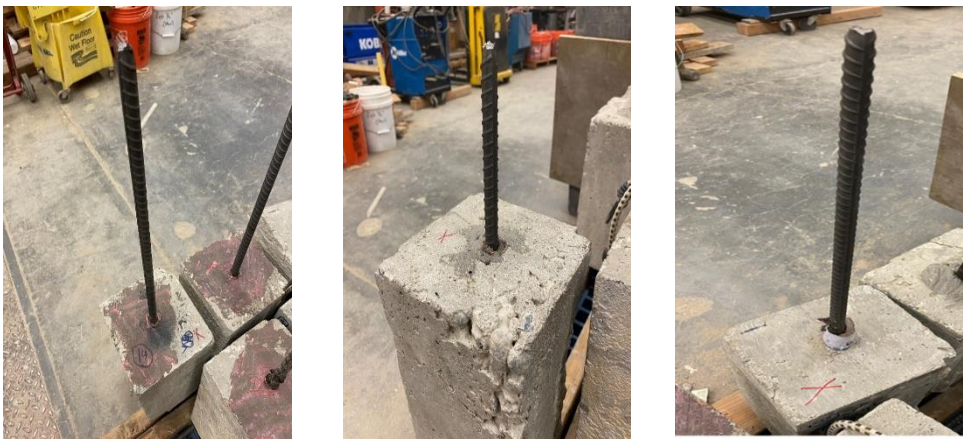

(a) G80-HIT, G80-SIK, and G80-MAS specimens (From left to right)

(b) SCCFRP with SIK (Gray-colored) and HIT (Red-colored) epoxies

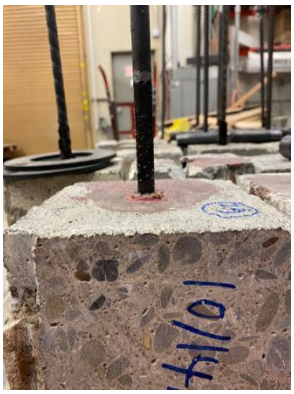

(c) SCFRP-HIT specimen

Figure 2.9: Failure modes of pull-out specimens

Figure 2.10 illustrates the bond force-slip relations obtained for the different tested sets. In general, the overall behavior of the curves consists of two main characteristics: at first, an initial increase in the bond force (linear part - ascending branch), followed by a drop once the maximum bond force has been reached or the load remains almost constant for any further increase in slip (non-linear part - descending branch). Sometimes the descending branch is short because failure occurs immediately after the descent began. The bond force-slip relations/curves match reported studies in the literature.

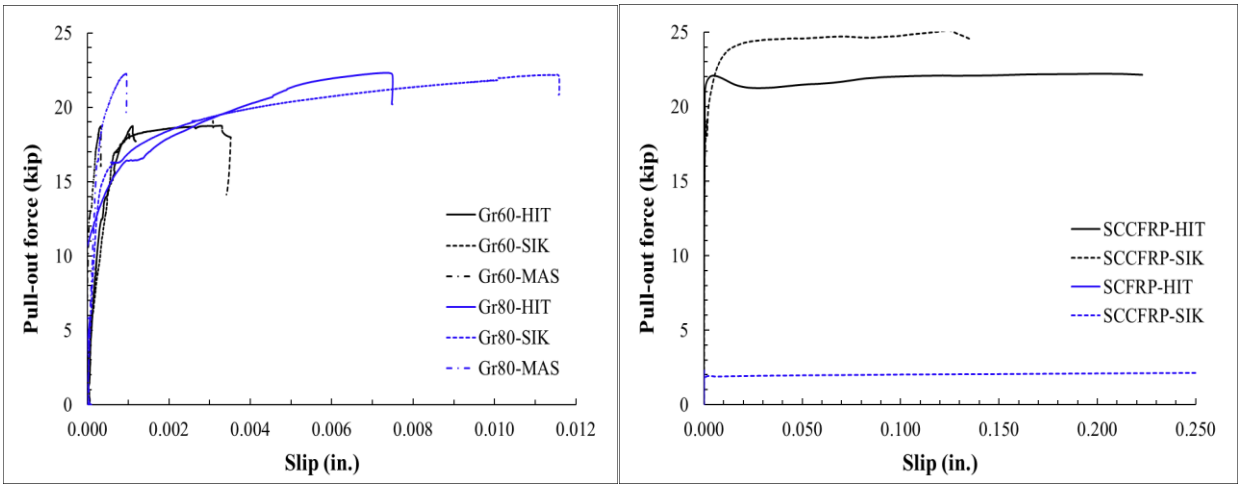

(a) (b)

Figure 2.10: Bond-slip relationships for tested bars: (a) Steel bars; (b) Sand-Coated CFRP bars

3.0 EXPERIMENTAL PROGRAM & CONTROL TESTS

In the previous section, preliminary pull-out testing provided information on the effectiveness of different approaches to enhance their shear strengthening abilities. In this section, details of the overall experimental program to evaluate the two different strengthening methods is presented.

3.1 Prototype Bridge and Experimental Model

After examining several drawings of existing cast-in-place T girder bridges in the Caltrans inventory, Donner Creek Bridge (Br #17-15 R/L) located west of Truckee in Nevada County was determined to be the best candidate for this project. The bridge carries two lanes of traffic with a narrow service lane and is on State Route 89 which is a state highway in the U.S. state of California that travels in the north–south direction, serving as a major thoroughfare for many mountain communities in the Sierra Nevada and the Cascade Range.

Based on the available as-built drawings and the Bridge Inspection Records Information System (BIRIS) document provided by Caltrans, the bridge was constructed in 1959 per the Standard Specification Division of Highways, Dated August 1954, and the special provision and designed per AASHO Dated 1953 with subsequent revisions, and Bridge Department Supplement Dated 1953 design code with H20-S16-44 (HS20) for live loading. Donner Creek Bridge is a single simply supported span with a length of 26.83 feet and a typical section of RC Tee six girders (Figure 3.1) supported by RC closed-end backfilled strutted abutments on spread footings. The total depth of the superstructure is 2.5 feet, and with a width of approximately 39.83 feet, the center-to-center distance between the internal girders is 7 feet and with overhang of 2.42 feet. In terms of the material properties of the superstructure, it was assumed that the Tee girders have a 3.0 ksi concrete compressive strength (f'_c) and reinforcing steel with yielding strength (f_y) of 40.0 ksi. All the geometry, design aspects, and material properties associated with this bridge made it a perfect fit for this project given the constraints in the testing facility at UC Davis. Additional details of the girder section including the shear and flexural reinforcement are displayed in Figures 3.2 and 3.3.

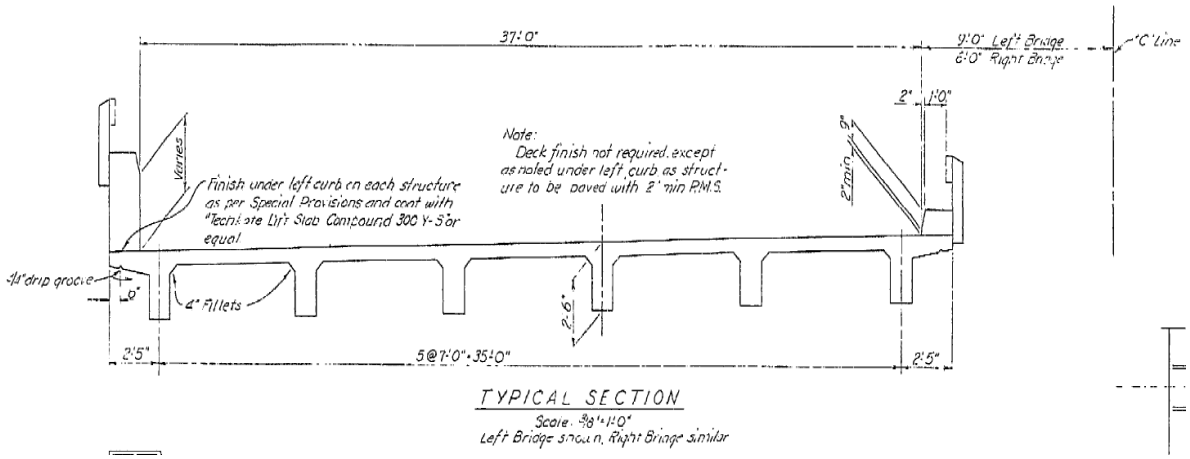

Figure 3.1: Typical Section of the selected prototype bridge

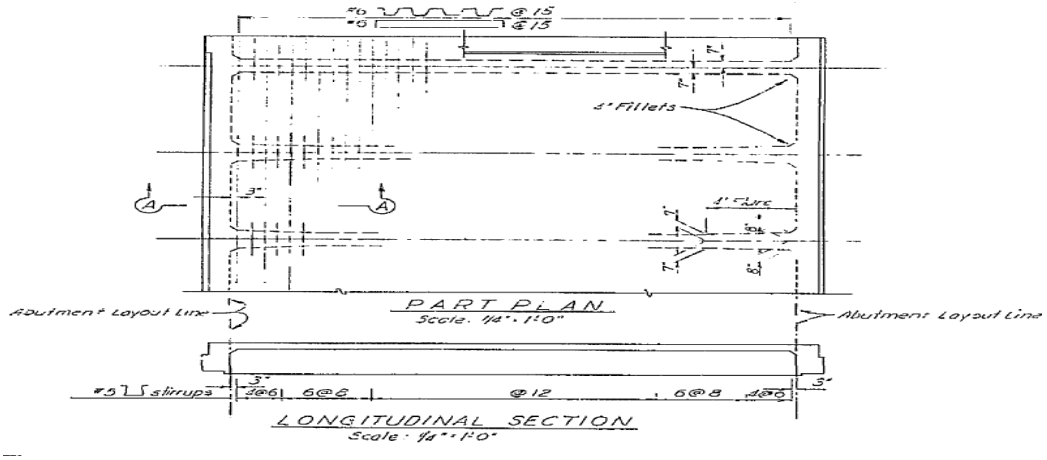

Figure 3.2: Shear reinforcement details of the selected prototype bridge

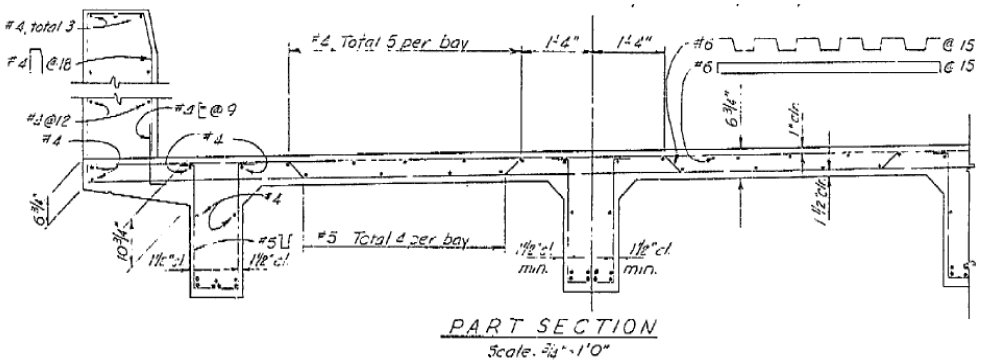

(a)

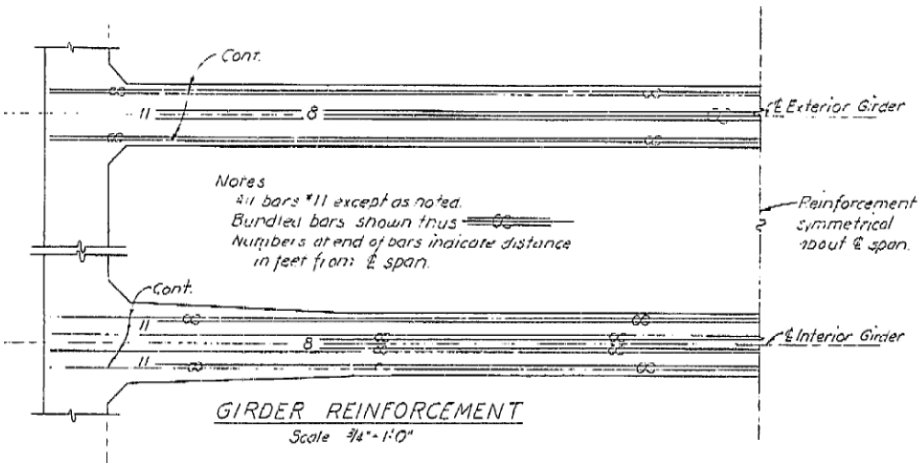

(b)

Figure 3.3: Flexural reinforcement details of the selected prototype bridge: (a) part section; (b) girder reinforcement

3.1.1 Experimental Model

The prototype bridge presented in the previous section was adapted for the proposed experimental testing by retaining the original cross-section and selecting suitable spans to facilitate two tests from a single specimen. Consequently, all constructed and tested girders in the project (a total of four, two per Phase) share the same design characteristics. Figure 3.4 presents the dimensional and reinforcement details of the constructed girders. It is worth noting that the girders were constructed with the flange on top, however, they were tested in an inverted configuration with the flange at the bottom.

As shown in the figure, the girder has a total length of 17.5 feet with spans of 6.0 feet (shear span) and 8.5 feet. The utilized span configuration was designed to work with the clamping system that is explained later in the test setup and instrumentation section of this chapter. The location of the loading point (**P** in Fig. 3.4) was such that 60% of the load was experienced by the tested region. This provided a shear span-to-effective depth ratio (a/d) of 2.67 which is bigger than the 2.50 limit at which arching effect is negligible (Collins and Mitchell 1997). The girder's flange width (b_f) and the total height (h) were 44 inches and 30 inches, respectively. The thickness of the web (b_w) and the flange (h_f) were 14 inches and 6.75 inches, respectively. The note in the figure indicated that in Phase I testing, Grade 40 #3 stirrups were

used as the existing shear reinforcement, whereas in Phase II testing, Grade 60 #4 stirrups were used as the existing shear reinforcement.

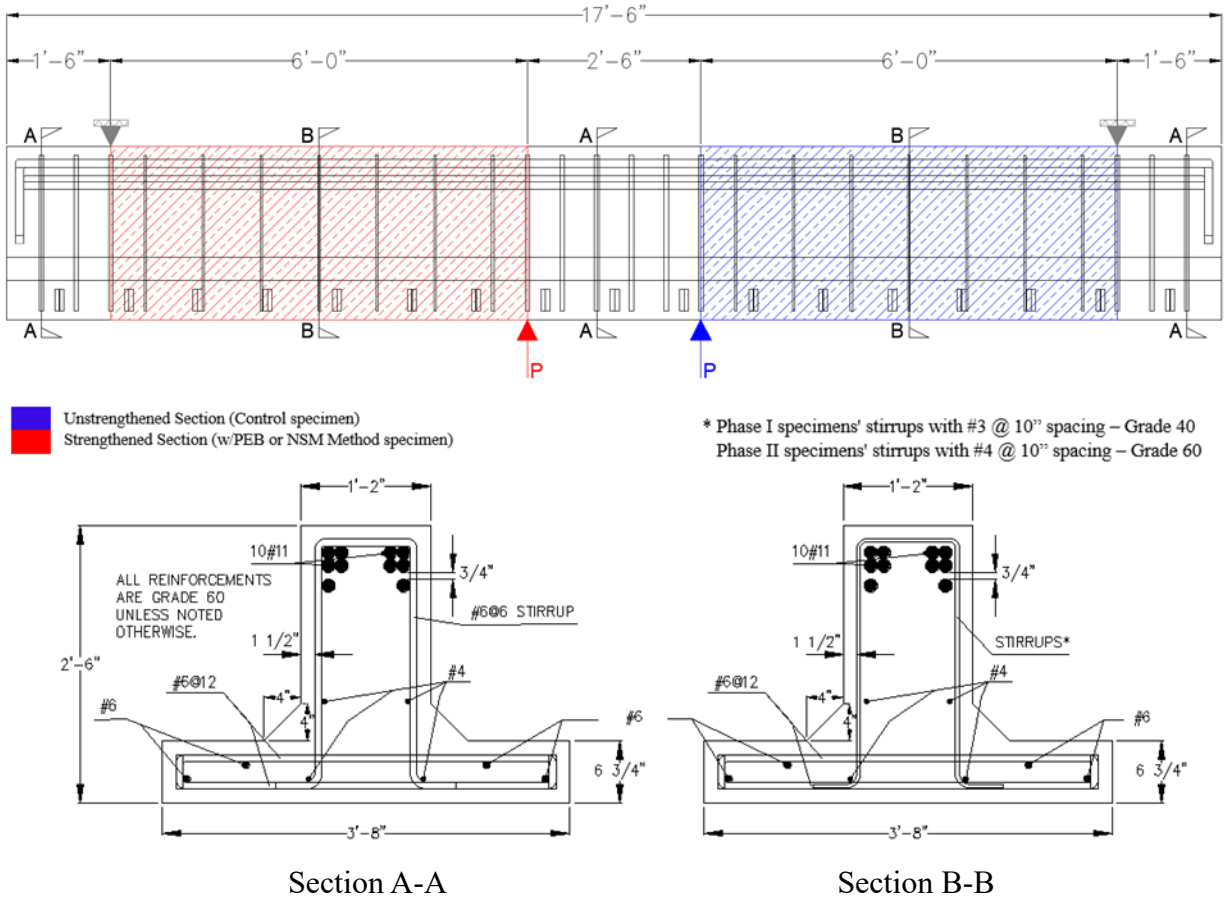

Section A-A Section B-B

Figure 3.4: General dimensional and reinforcement details of typical girder

3.2 Experimental Program

The experimental program consists of two phases. In each phase, a total of two full-scale RC T cross-section girders were constructed and tested in the structural testing facility at UC Davis. It is worth mentioning that this research is part of a project that aims to provide an assessment of the current shear-strengthening techniques of RC girders, identify the pros and cons of each approach, and select methods that are suitable for California bridges retrofit/rehabilitation. So, within each phase, a test of unstrengthened control specimen to provide a baseline for comparison, and two or three other tests with specimens shear strengthened with the Near-

Surface Mounted (NSM) strengthening technique and Partially Embedded Bars (PEB) method were executed. That ensures the consistency of the concrete properties across all the tested specimens within each phase. Table 3.1 outlines the test matrix and the specimen's details tested in the project. The following sections present a detailed description of the selection of the prototype bridge, girders design and fabrication, testing of material used and results, PEB method implementation, and test setup and instrumentation.

Table 3.1*:* Testing matrix and specimen details

Phase	*Specimen ID*	*f'c* (ksi)*	*Shear Reinforcement Bar Size & Grade*	*Strengthening Bar Size & Spacing (CFRP)*
I	Control I	4.0	#3 Grade 40	-
	PEB Scheme I			#4 @ 10"
	NSM Scheme I			#4 @ 10"
II	Control II	4.0	#4 Grade 60	-
	PEB Scheme II			#4 @ 10"
	NSM Scheme II			#4 @ 10"
	NSM Scheme III			#4 @ 5"

* Target concrete compressive strength @ 28 days

The transverse (shear) reinforcement size and strength were the main differences between the constructed girders in Phases I and II. In Phase I, the shear reinforcement was made with #3 (A_s = 0.11 in^2) ASTM A615 Grade 40 bars spaced at 10 inches which resulted in a shear reinforcement ratio of 0.15%. However, #4 (A_s = 0.20 in^2) ASTM A706 Grade 60 bars spaced at 10 inches were utilized for Phase II and resulted in a shear reinforcement ratio of 0.30%. In both Phases, the provided transverse reinforcement area (A_v) in the shear span (Section B-B) met the minimum transverse reinforcement area provision specified by AASHTO LFRD BDS (2017). Shear reinforcement with #6 (A_s = 0.44 in^2) bars spaced at 6 inches was also placed in the middle and the two ends of the girder. All longitudinal reinforcement was made with ASTM A706 Grade 60 bars, #4 and #6 (A_s = 0.44 in^2) bars for compression reinforcement in the top flange, and a

total of 10 #11 (A_s = 1.56 in^2) for flexural tension reinforcement that resulted in a longitudinal reinforcement ratio of 4.13%. The higher percentage ratio of the longitudinal reinforcement in the T girders is meant to ensure that the girder fails in shear and flexural failure is prevented.

3.3 Construction of Specimens

The girders were constructed on the strong floor of the structural testing facility at UC Davis. Figure 3.5 shows different stages of the formwork construction. As indicated previously, two girders were built and tested per Phase of this project and each girder was planned to produce two tests. To achieve the latter, PVC pipes were used to create holes through the girder's flange. The PVS pipes were placed through the girder's flange and a wooden frame was placed on top of the flange all work side by side to ensure the straightness of the made holes as they are going to be utilized by the clamping system (details provided in the Test Setup and Instrumentation section).

A ready mix of normal-weight concrete with a specified 28-day concrete compressive strength of 4,000 psi with a slump of 4 inches and water-to-cement ratio of 0.50 was used to construct all girders. Table 3.2 summarizes the concrete mix design. As the concrete arrived at the lab, concrete was checked for slump, and concrete cylinder test specimens were collected according to ASTM C143/C143M (ASTM 2020) and ASTM C192/C192M (ASTM 2019) respectively. The services of a professional concrete pouring and handling company were utilized to help with the distribution, vibration, and compaction of the concrete during the pour.

Figure 3.5: Formwork construction

Table 3.2*:* Concrete mixture (per cubic yard) used in girder's construction

Material	*Specific Gravity*	*Quantity (Ib/yd^3)*
Coarse aggregate (3/4")	2.65	1200
Fine aggregate (Con Sand)	2.63	1779
Cement (Type II/V)	3.15	440
Fly ash (ASTM C 618)	2.38	77
Admixture (Water Reducer/Type WRR)	-	17 oz
Water	1	40.0 gal

Approximately 8.0 cubic yards were delivered by one concrete mixer and sufficient to cast the two girders, cast cylinders for material testing, plus an allowance for waste. Photographs taken during the concrete pour are displayed in Figure 3.6. The two girders and concrete cylinders were cured under laboratory environmental conditions. Forms were stripped

approximately 1 week after the pour, then the PVC pipes were cut flush with the girder's flange surface. The effectiveness of the casting operation and formwork design is shown in Figure 3.7 where the specimen is seen to be free of any air pockets or delamination.

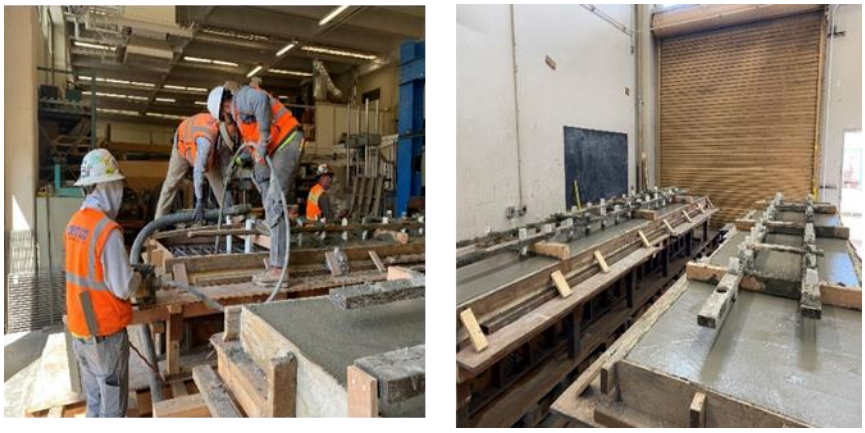

Figure 3-6: Concrete pour

Figure 3-7: Girder after removal of formwork

3.3.1 Material Characteristics

The concrete compressive strength (f_c') testing results of the tested specimens were obtained at 28 days and at the date of testing per ASTM C39/C39M (ASTM 2021). Table 3.3 summarizes the results for all specimens tested in the project. To obtain the material properties of the flexural

and shear reinforcement used in the girder's construction, uniaxial tensile tests according to the standard procedures outlined in ASTM A370 (ASTM 2022) were conducted, and the results are outlined in Table 3.4. The PEB-strengthening Sand Coated CFRP bars and Hilti HIT-RE 500 V3 epoxy adhesive used in this experimental campaign were identical to what had been used previously in the Pull-out tests reported in Chapter 2, thus no material properties are reported herein to avoid repetition.

Table 3-3: Concrete compressive strength of the tested specimens

Phase	Specimen ID	Concrete compressive strength, f'_c (ksi)	
		@ 28 days	@ Day of Testing
I	Control I	5.40	6.01
	PEB Scheme I		6.17
	NSM Scheme I		5.85
II	Control II	5.02	5.24
	PEB Scheme II		5.45
	NSM Scheme II		5.50
	NSM Scheme III		5.60

Table 3-4: Results of tensile tests of the steel reinforcement bars

Bar Size (Reinf. Type)	Yield Strength, f_y (ksi)	Tensile Strength, f_u (ksi)	Elastic Modulus, E (ksi)	Strain at yielding, ε_y (%)
#3 (Shear)	55.33	73.85	30000	0.19
#4 (Flexural/Shear)	66.36	98.65	29000	0.23
#6 (Flexural)	67.45	95.36	29000	0.25
#11 (Flexural)	68.38	92.50	29000	0.29

3.4 Test Setup and Instrumentation

The services of a professional moving and handling company were utilized to move and place the girder on concrete support blocks. Then, heavy reaction steel I-beams were placed at the ends of the girder to simulate the support conditions. Each reaction I-beam was tied to the strong floor of the laboratory using four high-strength rods connected to distribution beams which in turn are tied to the strong floor of the laboratory through high-strength DYWIDAG bars. A schematic drawing of the test setup is shown in Figure 3.8.

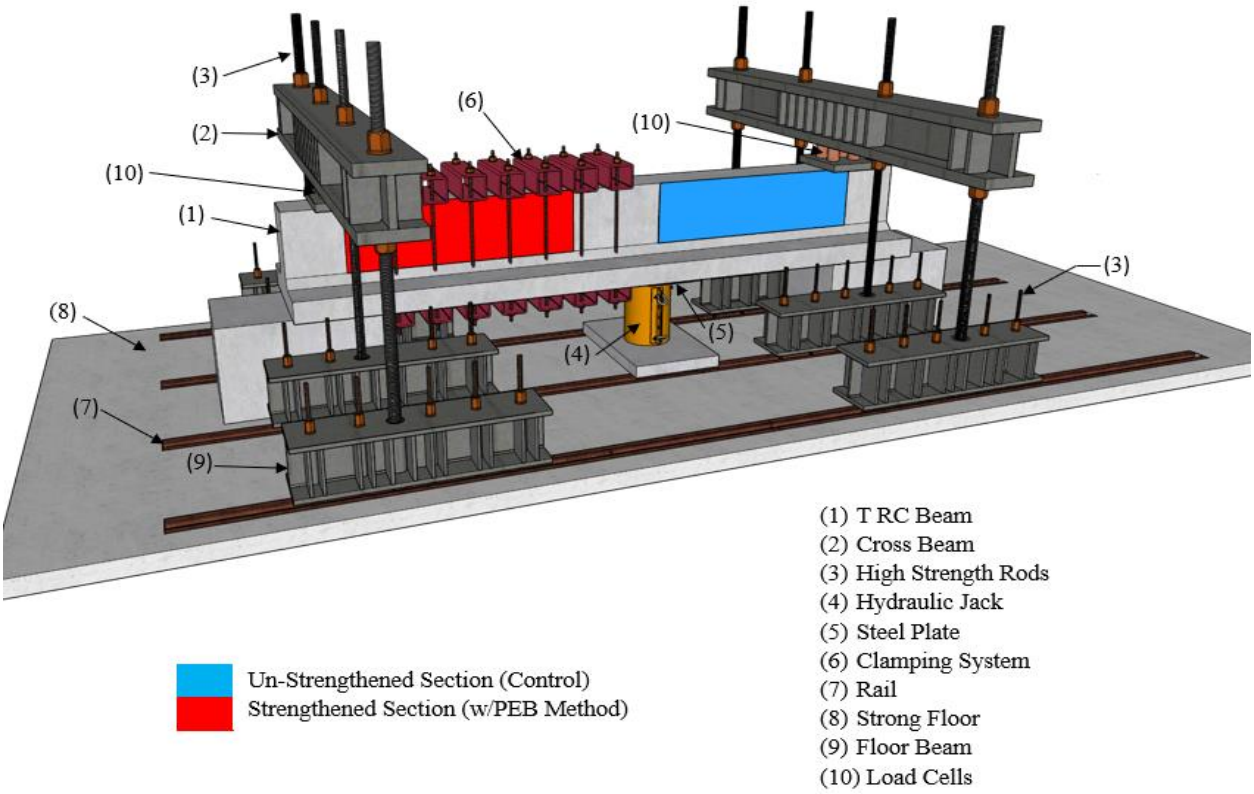

Figure 3-8: Schematic drawing of the test setup

As shown in the figure, the loading was applied to the bottom of the girder by a hydraulic jack connected to a pump equipped with a pressure transducer which can produce a maximum force of 1000 kips. The reacting forces on the girder from the applied load are resisted by the top reaction I-beams and then transferred through eight high-strength bars (four on each beam) to

distribution beams that are anchored to the floor. To measure the actual shear force acting on the critical section of the specimens, a set of four load cells was placed between the girder and the reaction I-beams. The load cells were placed on a steel plate with a thickness of 1 inch on top of the RC girder to avoid any load concentration that could damage the girder's ends. In addition, on the top of each load cell, a spherical bearing was placed to allow for the rotation of the reaction beams and ensure simply supported end conditions are achieved. In order to monitor the local strains in the steel reinforcement, each RC girder was instrumented with fourteen strain gauges: five strain gauges were bonded on selected stirrups of each tested specimen and a total of four on the longitudinal reinforcement. The strain gauge locations and labeling are identified in Figure 3.9.

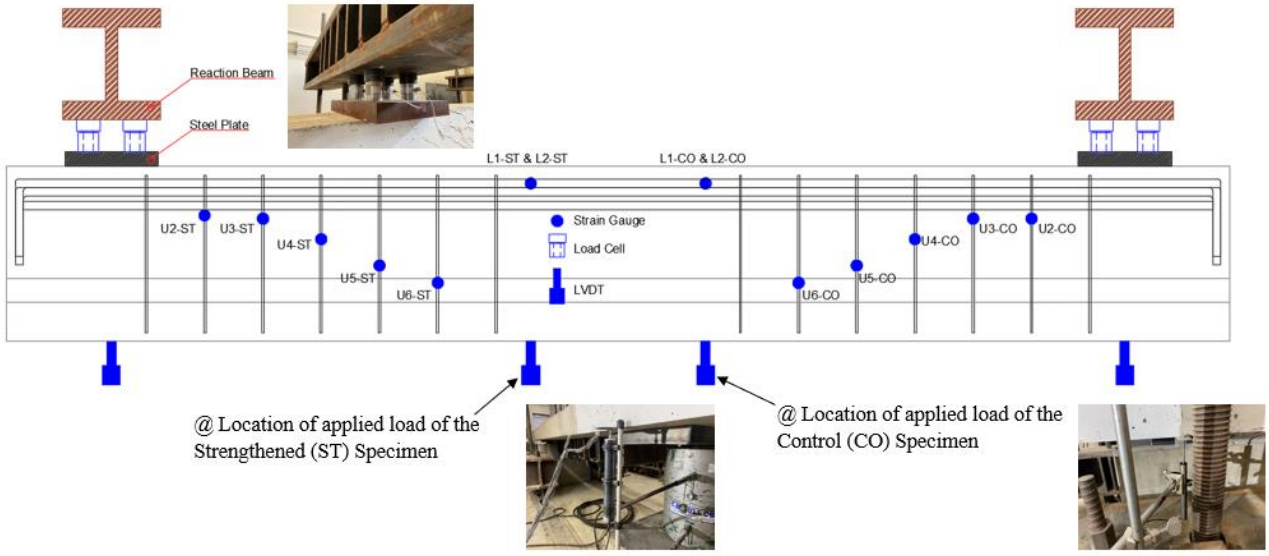

Figure 3-9: Instrumentation of the tested specimens

Additionally, linear variable differential transformers (LVDTs) were installed at three locations as shown in Fig. 3.9 to monitor the movement under the supports and at the location of the applied load. As stated previously, each girder was designed to produce two tests: at first, the unstrengthened (Control) specimen was tested until shear failure occurred then the point load (hydraulic jack) was shifted to the assigned location to conduct the second test (testing the strengthened specimen with each of the two methods). In both tests, neither the reaction I-beams nor the girder needed to be moved. However, to achieve this configuration of dual tests on a single girder, an external shear-strengthening (clamping) system was utilized to avoid any shear failure

in the untested section. The clamping system consisted of seven assemblies as shown in Figure 3.10 (only 5 are visible in the figure).

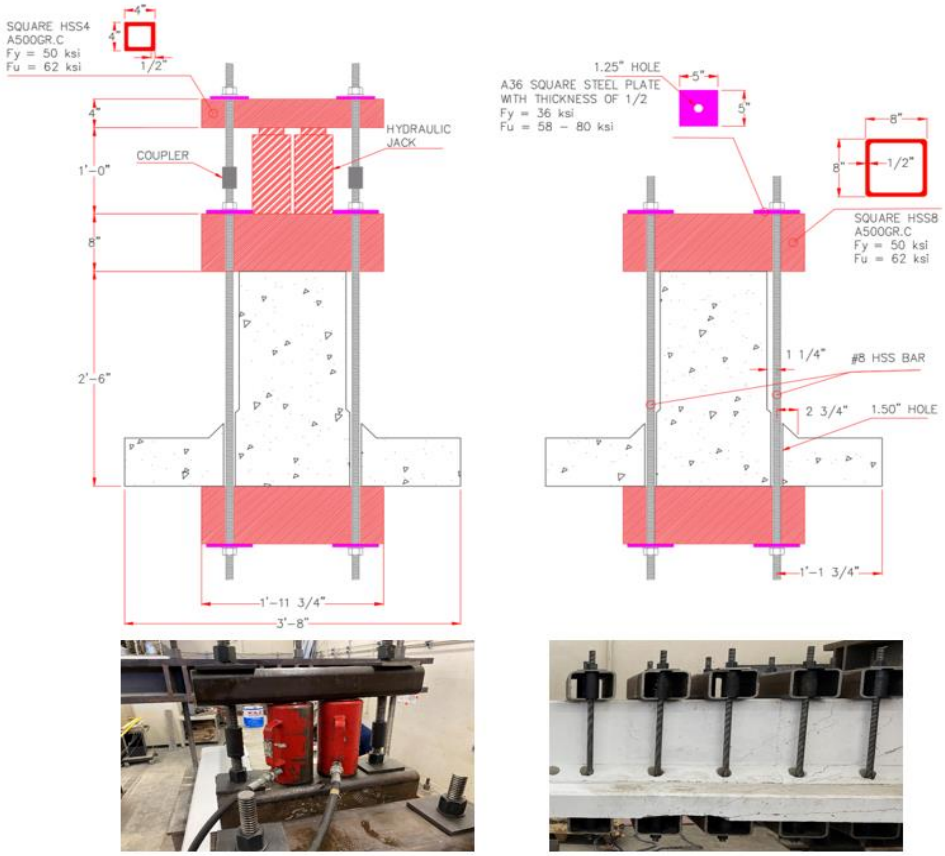

Figure 3-10: Schematic drawing and final installation of the clamping system

As shown in the figure, each assembly of the clamping system is consisted of two 8 in. x 8 in. x 1/2 in. HSS steel sections were placed on the top and bottom of the girder and connected by two #8 (diameter of 1 in.) high-strength bars having a yield strength of 150 ksi to ensure no yielding of the bars could occur through the tensioning process. Prior to conducting the first test, the clamping system was placed in the untested section, then the high-strength bars were tensioned by means of two hydraulic jacks applying force through a cross-beam (HSS steel section) as soon as the applied force reached the required force, the hex nut on top the 8 in. x 8 in. x 1/2 in. HSS steel section is hand-tightened and afterward, the pressure is released, and the hydraulic jacks are moved to the other assembly to complete the process. Once the first test is completed the clamping system shifted to the section where failure had occurred, and the process repeated again. Throughout the

whole process of tensioning the bars, the applied pressure/force through the hydraulic jacks was monitored carefully to avoid the concrete crushing of the girder or yielding the high-strength bars. Also, the strain in stirrups (shear reinforcement) was recorded to check the effectiveness of the procedure. Other successful implementations of this test configuration can be found in the work of Kim et al. (2012); Belarbi et al. (2012); and Alwash et al. (2021).

Experimental data including loads, displacements, and strains of the steel reinforcement were collected by using a National Instruments (NI) data acquisition system with the LABVIEW software, and the sampling rate was set at 200 Hz for all the data channels. The results of the control tests are reported in the next section and results of testing the strengthened specimens are reported in the next chapter.

3.5 Control Tests

In each phase of testing, two specimens were cast from the same batch of concrete. Hence two control tests were conducted to establish the baseline performance of the unstrengthened specimens for each batch of concrete. Results from the tests on the unstrengthened sections of the specimens are reported here.

3.5.1 Test #1

Figure 3-11 presents the shear force-displacement curves of the first control specimen. The force-displacement response is essentially linear up to a shear force of about 75 kip. Above this shear force level, the shear force-deflection curves turned nonlinear due to the propagation of both flexural and shear cracks. Then, at about a shear load of 178 kip a sudden drop in load was observed, which is a characteristic of shear failure – this load represented the peak shear force obtained with the unstrengthened specimen with a corresponding displacement of 0.46 inches at mid-span.

In the early stages of loading, hairline flexural cracks developed in the web near the point of load application and in the shear span region. This was followed by inclined web shear cracks at the mid-height of the web in the shear span region as the applied load increased. Upon further loading, more inclined web shear cracks appeared in the shear span zone and started to extend into two

directions: one towards the support and another torwards the point of load application going through the flange portion of the girder. As the applied load increased further, a major inclined shear crack become more distinct. The width of the crack kept increasing until failure. The compression shear failure of the specimen occurred with one distinct inclined crack at an angle of approximately 30°. Fig. 3-12 presents the crack progression of the control specimen at different shear force levels. Yielding of stirrups was evident from the recorded strains (reported later) but post-examination of the tested specimen showed no signs of rupture of the steel stirrups.

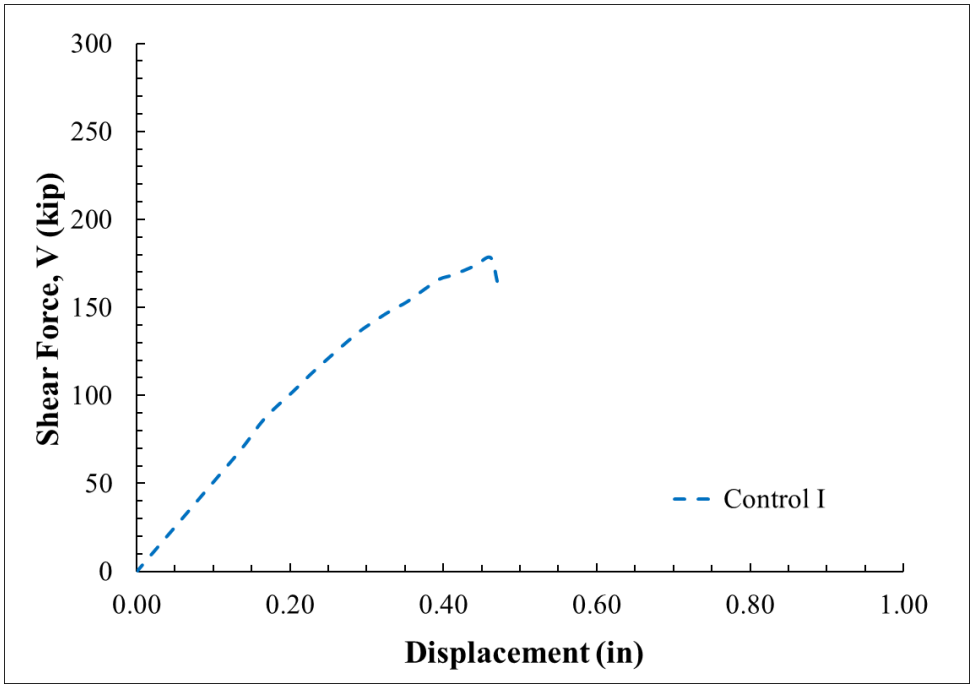

Figure 3-11: Shear force vs. displacement response of control I specimen

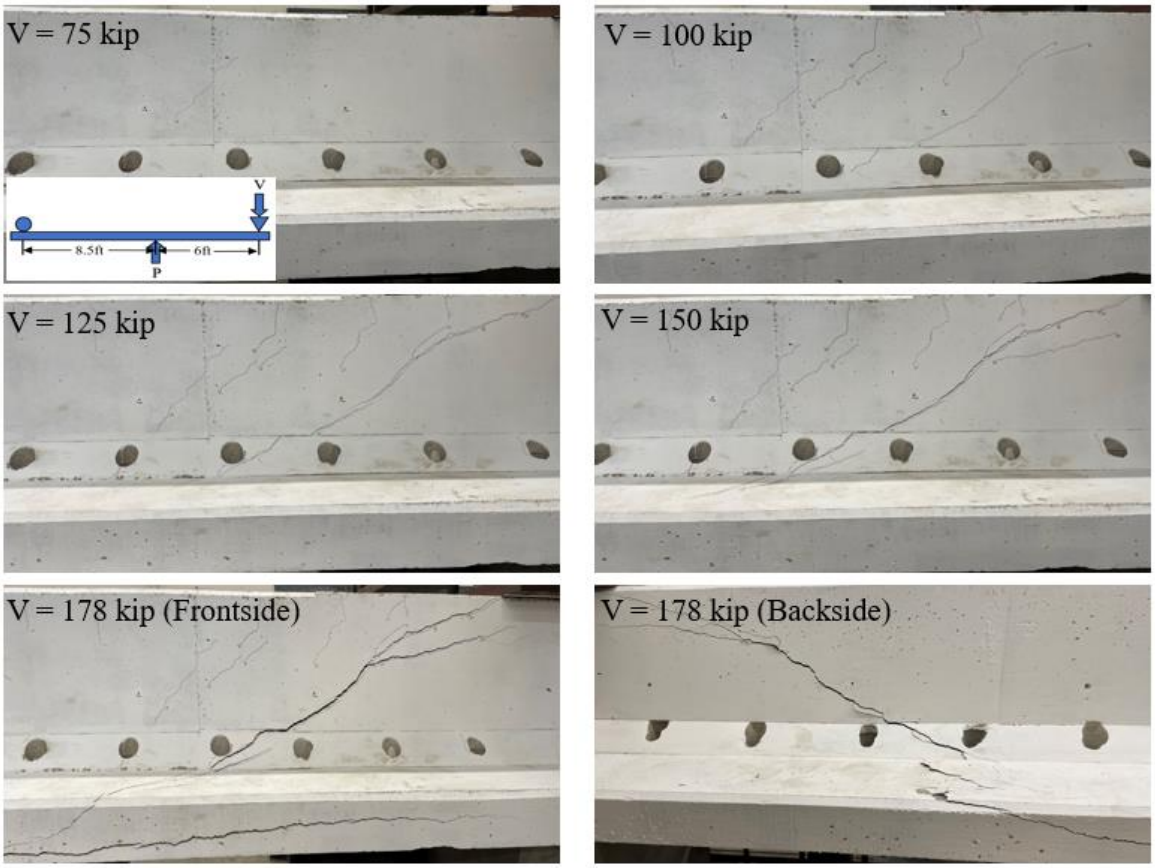

Figure 3-12: Crack development in Control I specimen

3.5.2 Test #2

Figure 3-13 shows the shear force-displacement curve of the second control specimen. The response is seen to be linear up to a shear force of about 60 kip. Above this magnitude, the shear force-deflection curves turned nonlinear due to the propagation of both flexural and shear cracks. Upon further loading, at about a shear force of 239 kip a sudden drop in load was observed. This load represented the peak shear force of the unstrengthened (Control) specimen II at a corresponding displacement of 0.91 inches at mid-span. The specimen failed in shear with two main inclined shear cracks in the girder's web, the top shear crack had an inclination of about 20° with respect to the girder's longitudinal axis whereas the bottom shear crack had an inclination of about 30°.

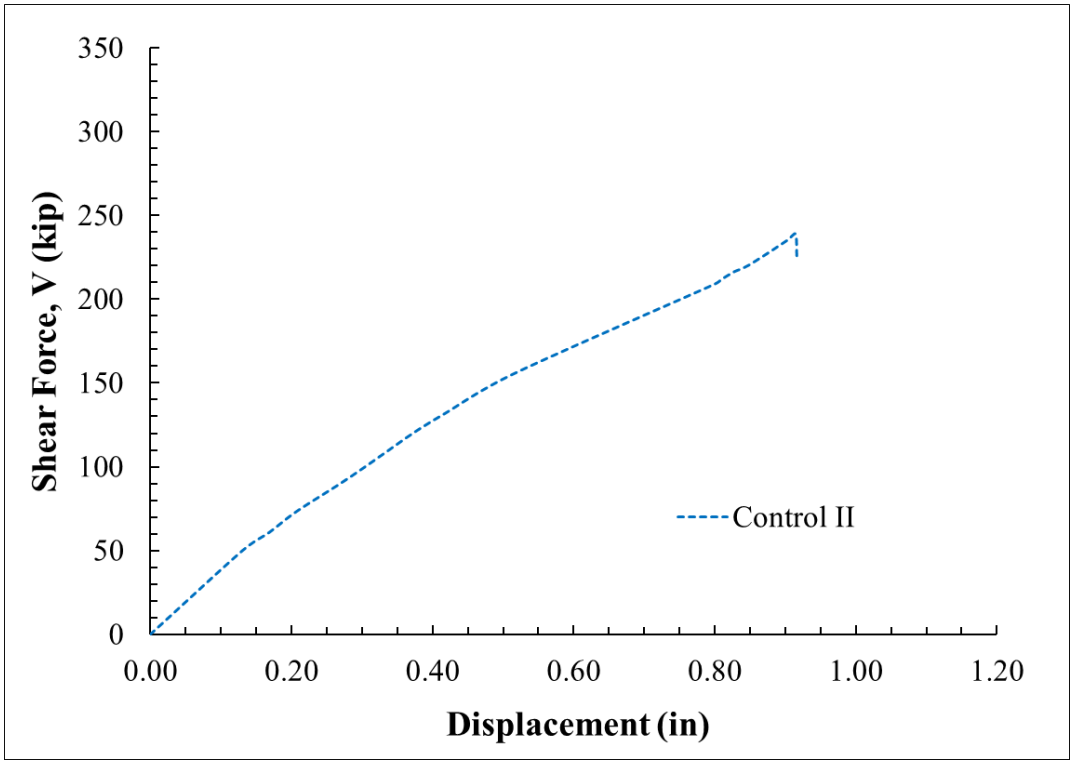

Figure 3-13: Shear force vs. displacement response of control II specimen

Both cracks merged at a point close to the support (steel plate) without propagating further towards the support. Both top and bottom shear cracks extended into the girder's fillet, however, they did not propagate further towards the flange and ended up at the point of load application in the same manner observed with the unstrengthened (Control I) specimen. Figure 3-14 displays the crack development in Control II specimen at different shear force levels. As in the case of the Control I specimen, hairline flexural cracks developed in the web at the point of load application and in the shear span regions during the early stages of load application. Next, inclined web shear cracks at mid-height of the web started to spread in the shear span region as the applied load was increased. Upon further loading, the inclined web shear cracks started to extend towards the support and point of load application. With further increase in load, the inclined shear cracks become more distinct and widened until failure. Once again, a shear compression failure occurred due to crushing of the concrete in the main compression strut. Strain guage data indicated that the steel stirrups yielded but none of them ruptured.

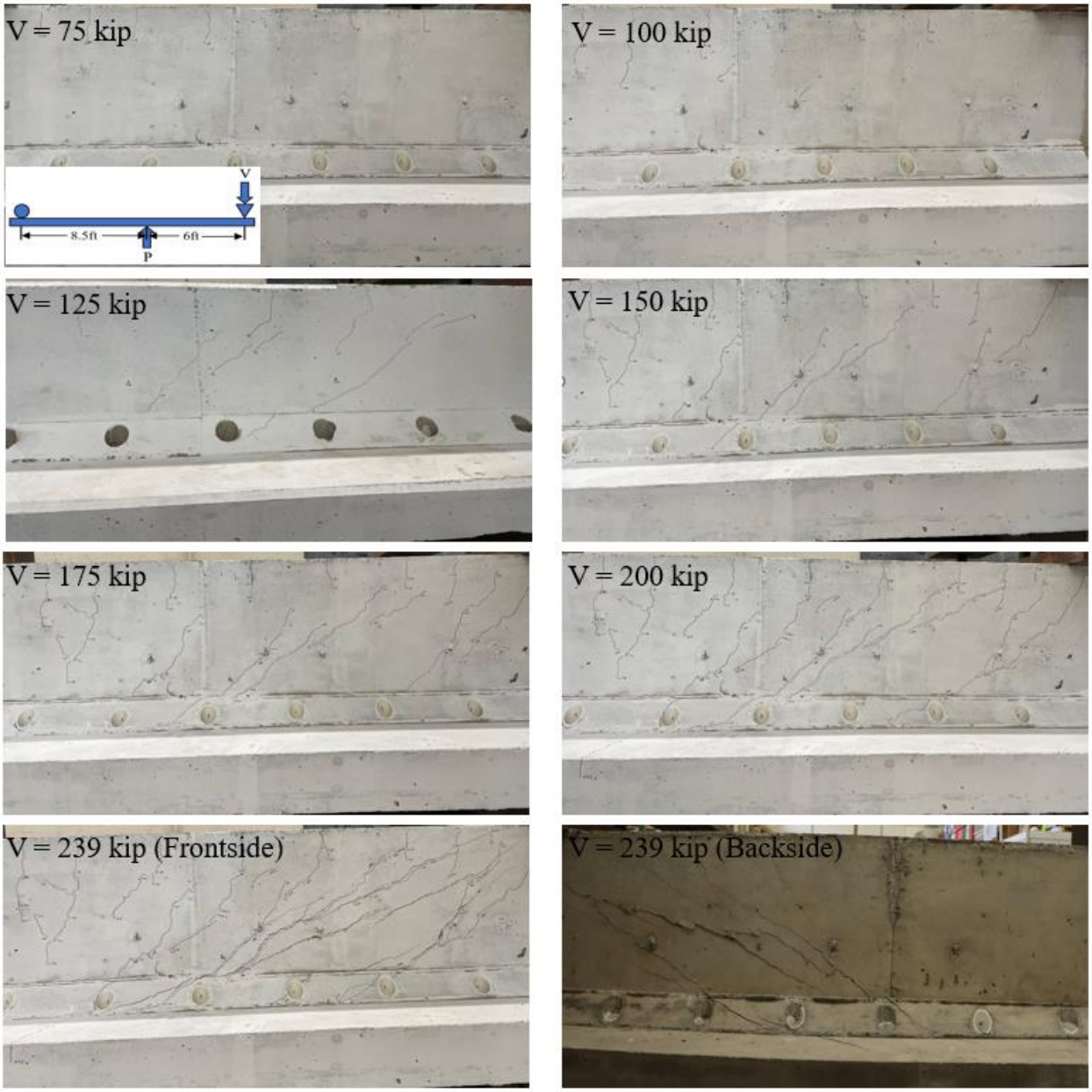

Figure 3-14: Crack development in Control II specimen

4.0 PREDICTED RESPONSE OF CONTROL AND STRENGTHENED SPECIMENS USING FINITE ELEMENT MODELING

Numerical simulations through finite element modeling (FEM) of the tested specimens were carried out to gain some insight into the increased shear resistance provided by the proposed strengthening schemes. But first it is necessary to develop a model that can be validated with the control tests presented in the previous section. Thus, a series of finite element (FE) simulations of the tested specimens were carried out to reproduce the observed shear-displacement responses and failure mechanisms and to generate a calibrated/validated model that can be utilized in the prediction of the shear enhancement with the proposed strengthening methods. This chapter describes the details of the numerical models developed for the present study.

4.1 Numerical Modeling

In the present study, the commercial software ATENA (Cervenka et al. 2021) was used in the numerical simulations. Within ATENA Science, two fully integrated software packages are utilized, namely GiD and ATENA. GiD (https://gidhome.com) is used as a pre-processor for defining the geometric and material properties, along with the generation of the finite element mesh. As the finite element model is completed within the GiD environment, the model can be loaded automatically into either ATENA Console or ATENA Studio wherein the nonlinear analysis is executed. For the presented study, ATENA Studio was employed. Post-processing of the results can take place either in real-time while the analysis is still in progress in ATENA Studio or through GiD after the analysis is complete. The ATENA software was developed to specifically simulate the behavior of concrete and reinforced concrete structures including concrete cracking, crushing, and reinforcement yielding. Another feature of the software that was also appealing for the present study was the ability to model reinforcing steel and CFRP bars as discrete bars.

4.2 Constitutive Modeling

4.2.1 Concrete

Concrete is modeled using 3D continuum finite elements. Many constitutive models are available in ATENA to represent the behavior of concrete (Cervenka et al., 2021). In this study, the concrete model named CC3DNonLinCementitious2 was utilized as it is recommended by the software developer for 3D models and is based on theory that has been examined by many researchers (Al-Tarafany 2016; Vásquez 2019; Tambusay and Suprobo 2019; Tambusay et al. 2021). The implemented fracture-plastic model combines constitutive models for tensile (fracturing) and compressive (plastic) behavior. The fracture model is based on the classical orthotropic smeared crack formulation and crack band model. It employs the Rankine failure criterion, exponential softening, and it can be used as a rotated or fixed crack model. The hardening/softening plasticity model is based on the Menétrey-Willam failure surface (Cervenka et al. 2021). The parameters used in the simulation are described below:

(a) Basic parameters: The compression strength (*f'c)* specified was obtained from the concrete cylinder compression tests reported in Chapter 3. Young's modulus, Poisson's ratio, and tension strength were calculated based on AASHTO (2017) articles C5.4.2.4-2, 5.4.2.5, and 5.4.2.7, respectively.

(b) Tensile parameters: The formulation proposed by Phillips & Zhang (1993) was used to specify the fracture energy (*Gf*). The smeared fixed-crack model was considered appropriate to represent the cracked concrete of the tested specimens (Godat et al. 2013; Barros et al. 2013; Breveglieri et al. 2016; Brindley 2017). Activation of crack spacing, minimum crack spacing, tension stiffening, the shear factor, and the unloading factor were not necessary as the tested specimens were neither heavily reinforced nor modeled with finite element sizes smaller than the aggregate size. The aggregate interlock model was activated by specifying a maximum aggregate size of 0.75 inches which corresponds to the size of the aggregate used in the concrete mix. By activating this model, the shear strength of cracked concrete is calculated based on that employed by the Modified Compression Field Theory of Vecchio and Collins (1986).

(c) Compressive parameters: The plastic strain at peak load called (εcp) was determined by

subtracting the elastic strain at $f'c$ from the total strain at $f'c$. ($fc0$) corresponded to the onset of nonlinearity and was determined based on the formula reported by Cervenka Consulting. (wd) which corresponds to the critical compressive displacement was set to a value of -0.02 inches as suggested in Cervenka et al., (2021). (*Fc reduction*) is a parameter that reduces the concrete compressive strength due to cracking and it was set equal to the default value of 0.8.

(d) Miscellaneous parameters: The eccentricity is the parameter defining the shape of the failure surface and was kept at the default value of 0.52. The parameter corresponding to the direction of the plastic flow β was also kept at the default value of 0.0. Other parameters not relevant to the simulation were also maintained at default values.

4.2.2 Reinforcement

The ATENA program offers two approaches to model the reinforcement which is designated as *Reinforcement*. In the first approach, the reinforcement can be modeled using a uniaxial material associated with discrete line (truss) elements, and in the second approach, the reinforcement can be represented through smeared reinforcement associated with the concrete material in 3D elements (Cervenka et al., 2021). Given the reinforcement distribution in the tested girders, reinforcing steel bars of the longitudinal (flexural) and transverse (shear) reinforcements are modeled using the first approach in which uniaxial truss elements with a multi-linear stress-strain relationship are used. The bond between concrete and steel was assumed to be perfect (no bond-slip considered). Figure 4-1 shows the multi-linear stress-strain relationship for the reinforcing steel material.

Table 4-1 presents the input parameters used for the steel reinforcement. It is worth noting that only three points of the stress-strain relationship were utilized, and the corresponding values were based on the obtained tensile test results reported in Chapter 3, with the third point representing rupture of the bar. The fourth point can be specified below the 3rd point to simulate post-peak softening due to necking. Additionally, the same behavior is assumed in both tension and compression. Since bar buckling is not expected in the girder simulations, this assumption is reasonable for the present study.

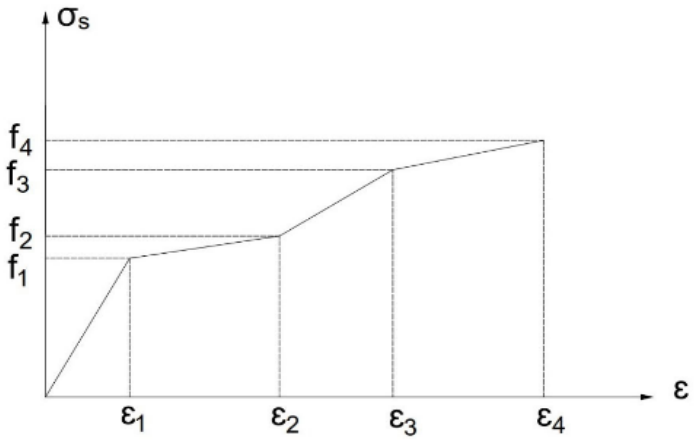

Figure 4-1: Multi-linear stress-strain relationship for reinforcing steel in ATENA (Note: only three points were used in this study as listed in Table 4-1)

Other Materials

A linear elastic tensile model until failure designated as *1D Elastic Isotropic* in ATENA was used to represent the CFRP bars. The rupture point on the stress–strain curve defines the maximum stress and strain of the CFRP bars. The CFRP bars were modeled in the same way as the steel flexural and shear reinforcements wherein each bar was modeled discretely as truss elements. Specified material properties were based on the tensile test results provided in Chapter 3. Steel bearing plates are used to represent the loading plate, plates at the supports, and HSS steel sections used to construct the assemblies of the clamping system. The model used for these steel plates is *3D Elastic Isotropic* as designated in ATENA. The material constitutive model is linear elastic with a Young's modulus of 29,000 ksi and Poisson's ratio of 0.3.

4.3 Geometric Modeling

The concrete in the tested specimens was modeled using 3D solid 8-node hexahedral (brick) isoparametric elements with three degrees of freedom (DOF) per node utilizing a linear shape function with eight nodes. The linear element was chosen to reduce the total number of DOFs since the girder had to be modeled at its full length as the loads and supports were not symmetrical. The longitudinal steel reinforcement, steel stirrups, and CFRP bars in the concrete

were represented by 3D truss elements. Full strain compatibility was assumed between the CFRP bars and the concrete because the CFRP bars remained well attached to the concrete until failure. The steel plates at the loading point and the end supports were modeled using 3D solid 8-node hexahedral (brick) elements with a linear shape function similar to concrete. However, the clamping system bearing plates were modeled using 3D solid 4-node tetrahedral linear elements.

Table 4-1: Input parameters for steel reinforcement modeling

Steel Bar Size:	#3	#4	#6	#11
Basic				
Material Prototype	CCReinforcement			
Young's Modulus [ksi]	30000	29000	290000	29000
Profile [in.]	0.375	0.500	0.750	1.410
Area [in.^{2}]	0.110	0.196	0.441	1.561
Stress-strain properties				
Yield Strength YS [ksi]	50.33	68.00	68.00	68.00
Number of multilinear values	3	3	3	3
eps2	0.024	0.01	0.01	0.01
f2 [ksi]	51.00	70.00	70.00	70.00
eps3	0.06	0.12	0.12	0.12
f3 [ksi]	66.00	94.00	94.00	94.00
Miscellaneous				
Rho-Density [lb./in.^{3}]	0.284	0.284	0.284	0.284
Thermal Expansion Alpha [F^{-1}]	6.7E-06	6.7E-06	6.7E-06	6.7E-06
Active in Compression	Yes	Yes	Yes	Yes
Element Geometry				
Geometrical Non-Linearity	Non-Linear	Non-Linear	Non-Linear	Non-Linear
Geom Type	Normal	Normal	Normal	Normal
Elem Type	CCIsoTruss	CCIsoTruss	CCIsoTruss	CCIsoTruss
Embedded Reinf.	Yes	Yes	Yes	Yes
Minimum [in.]	0.039	0.039	0.039	0.039
Embedded short bars	Yes	Yes	Yes	Yes

4.4 Results of Finite Element Simulations

The main objective of this phase of the study was to establish a FE model that can initially be used to predict the behavior of RC Bridge Girders with and without shear strengthening.

4.4.1 Control Tests

The finite element discretization of the unstrengthened (Control) specimens are shown in Figure 4-2. All reinforcing steel bars are explicitly represented within the finite element model. Preloading features provided in ATENA were used first to apply the post-tensioning forces to the steel bearing plates which represented the HSS steel sections used to construct the assemblies of the clamping system described in Chapter 3. Then, the vertical load at the mid-point of the bearing plate was applied as a prescribed deformation. Both the post-tensioning force and the vertical loads were applied in steps to avoid numerical issues and to mimic the exact loading protocol used in the experimental testing. The steel bearing plates representing the supports in the finite element model were appropriately modeled to simulate experimental boundary conditions (e.g., the end supports restrain vertical movement while allowing free rotation).

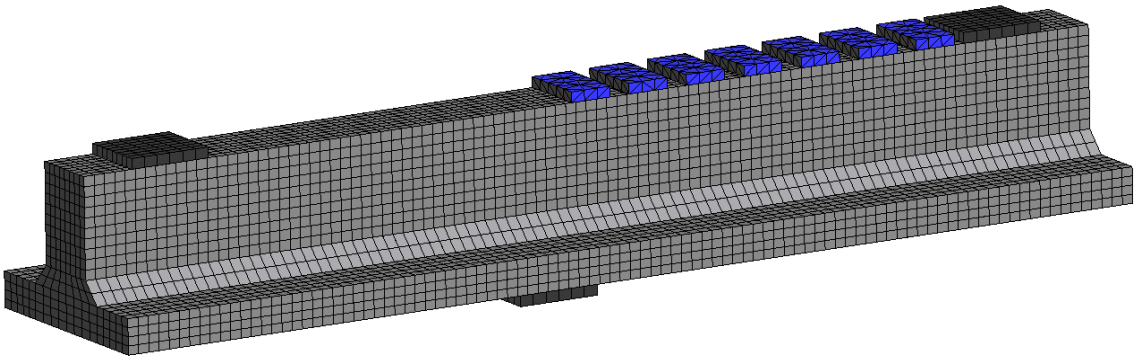

(a)

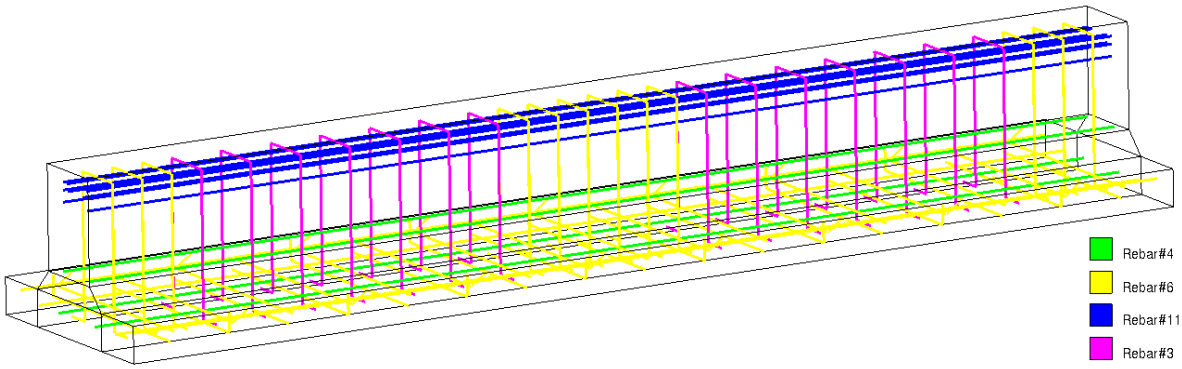

(b)

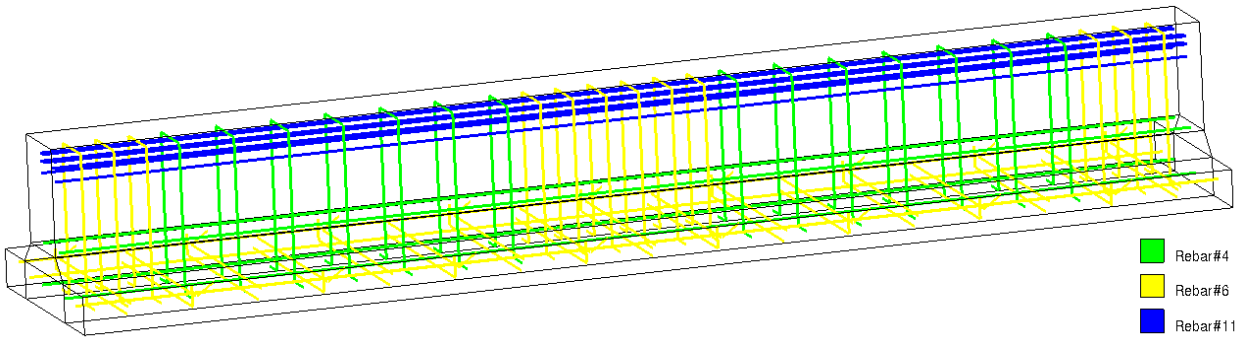

(c)

Figure 4-2: Finite Element model: (a) Girder specimen with the clamping system, loading, and support plates; (b) Control specimen I; (c) Control specimen II

Shear Force-Deflection Response

The predicted shear force-deflection response for the unstrengthened (Control I and II) specimens are plotted in Figure 4-3. For the unstrengthened (Control I) specimen, the numerical simulation resulted in a linear force-deflection response up to a shear force of about 70 kips. Above this magnitude, a nonlinear response is evident. At a shear force level of approximately 92 kips, first yielding of shear reinforcement (stirrups) occurred. The specimen failed due to crushing of the concrete in the main compression strut when the shear in the critical section reached 193 kips. Likewise, the second control specimen (denoted Control II) exhibited a linear response till the occurrence of shear cracks followed by yielding of the stirrups. Failure, in a manner similar to Control I, was recorded at about 240 kips, which corresponds to a 24% increase in shear capacity due to the transverse reinforcement being increased from #3 to #4 bars.

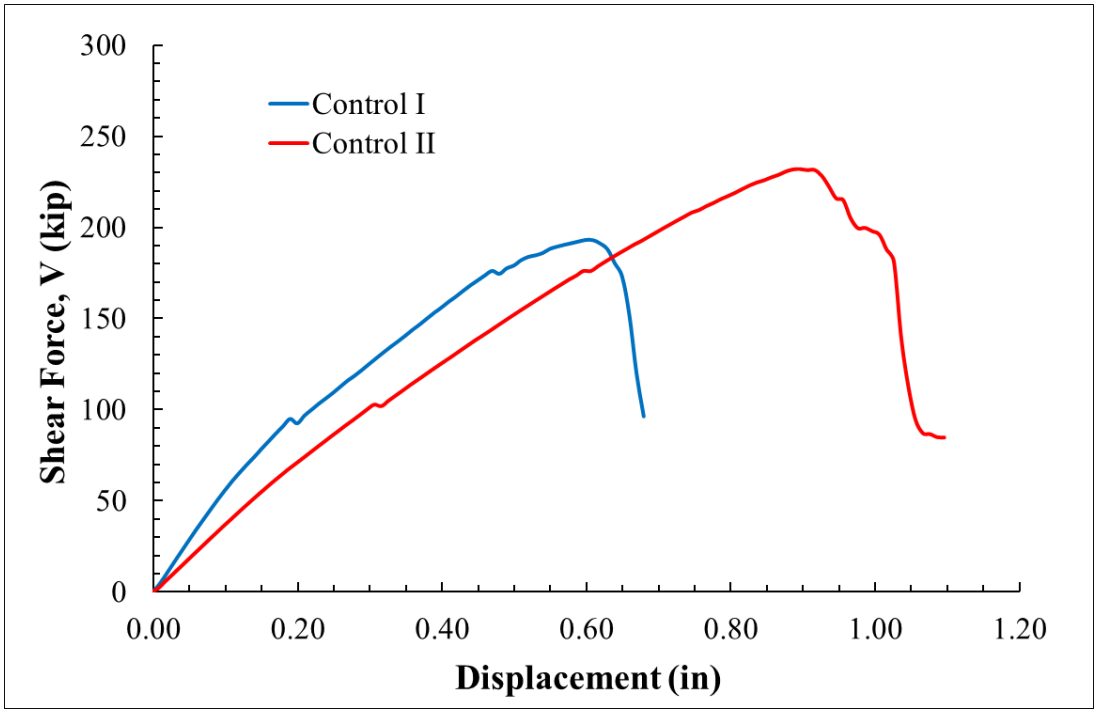

Figure 4-3: FE simultion of shear force vs. displacement response of control specimens

Strains in the Flexural and Shear Reinforcement

As indicated previously, all reinforcing bars in the simulated specimens were modeled with discrete line (truss) elements. This enables the user to easily extract the axial strain and/or stress of any reinforcing bar of interest by setting a monitor for the reinforcement within the ATENA software. The relationships between the shear force in the simulated specimens and the strains registered in longitudinal (flexural) and transverse (shear) reinforcements are shown in Figure 4-4 and Figure 4-5, respectively for the control specimens. The labeling of the monitored bars follows the notation used in the experimental testing and was presented in Figure 3-9 in Chapter 3. In both simulated specimens, the shear force-strain response was essentially linear up to the yielding of the shear reinforcement. The strains in the longitudinal reinforcement remained well below the yielding strain thereby precluding flexural failure of the specimens. Strains in all instrumented stirrups exceeded the yield strain, as expected.

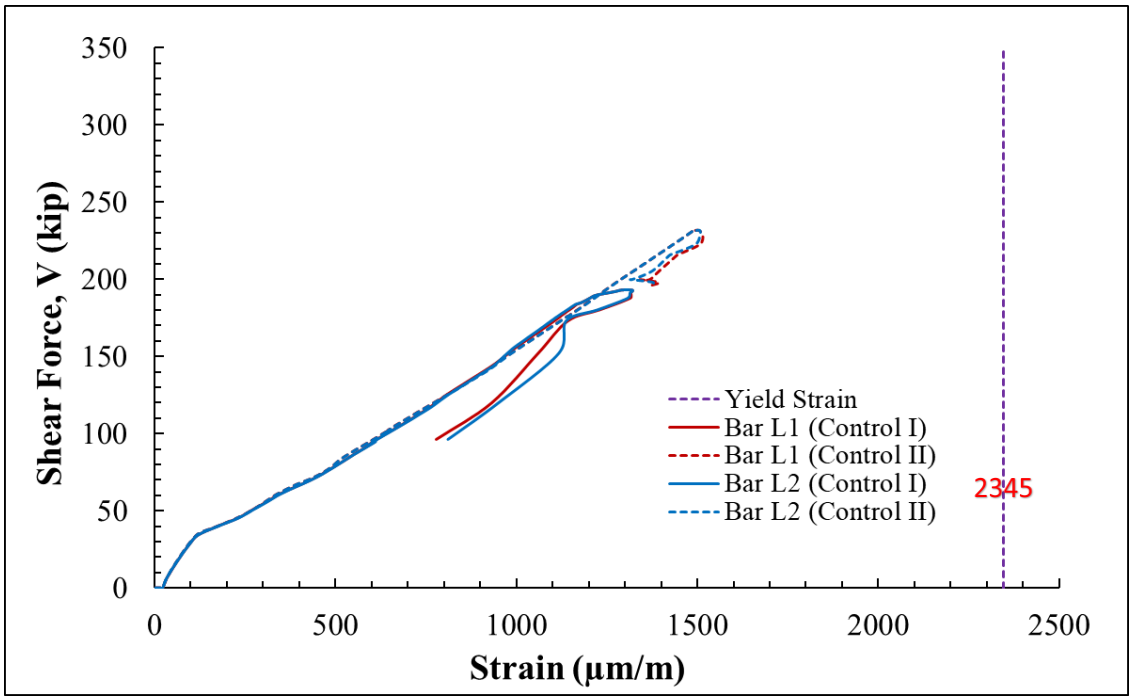

Figure 4-4: Shear force vs. strain in longitudinal reinforcement of control specimens

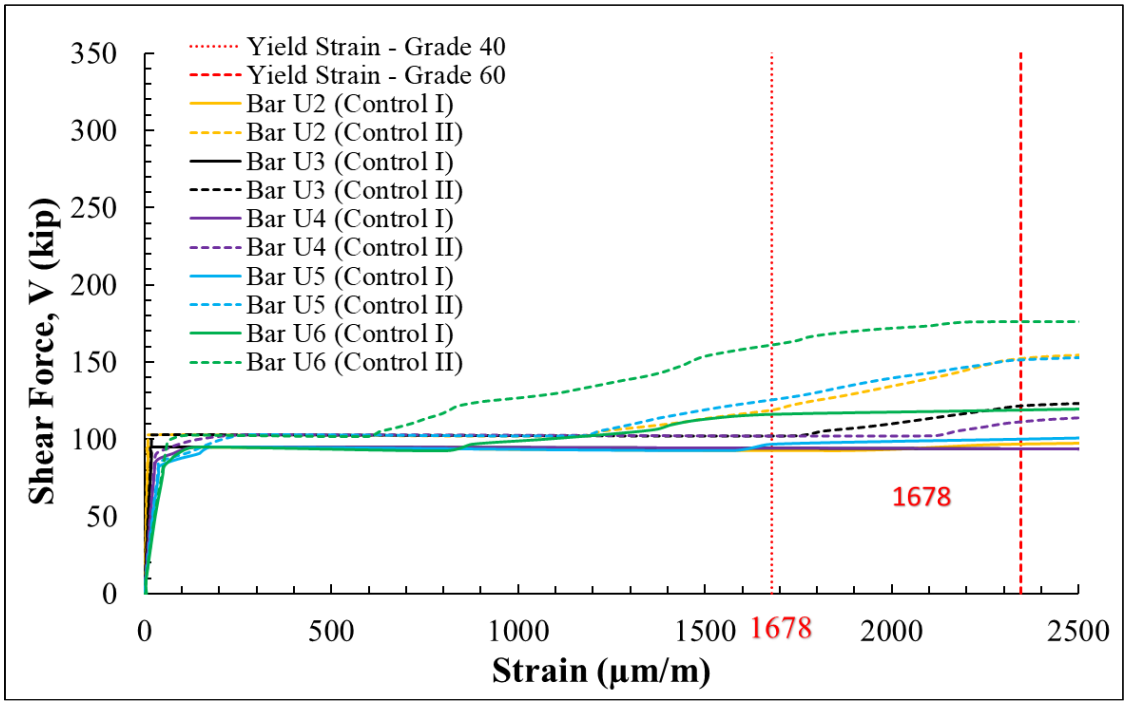

Figure 4-5: Shear force vs. strain in transverse reinforcement of control specimens

Cracking Patterns and Failure Modes

Figure 4-6 presents the simulated crack patterns and crack widths at two stages of loading of the unstrengthened control specimens. Flexural cracks developed initially propagating from the top into the web and across the shear span. With increased loading, it is evident that inclined web shear cracks developed at the mid-height of the web in the shear span region which eventually extended both towards the support and the loading point.

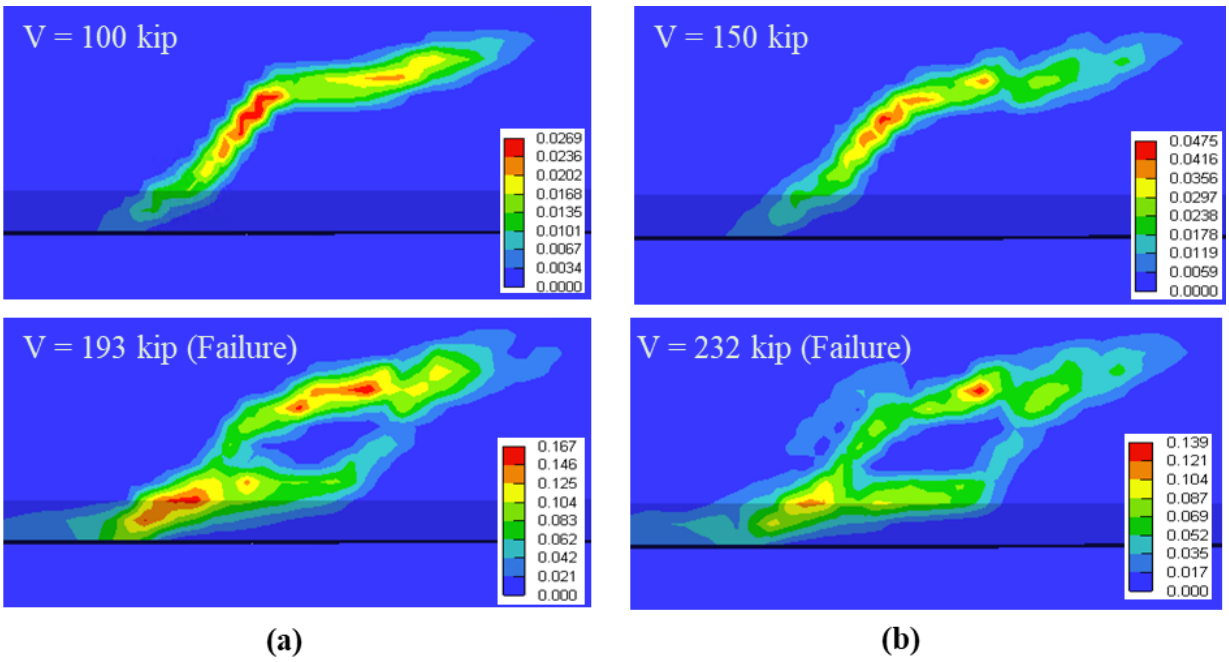

Figure 4-6: Crack progression in control specimens: (a) Control I; (b) Control II (Legend: crack width in inches)

4.5 Validation of FE Modeling

Results of the numerical simulation are compared with the experimental response in Figure 4-7. Overall, the simulations are in agreement with the observed response. Small discrepancies in the response between the experimental and the numerical curves are evident as the response becomes nonlinear. The computed peak load and deflection for Control Specimen I were slightly higher than the observed experimental results (less than 10% and 30% difference in peak load and displacement, respectively).

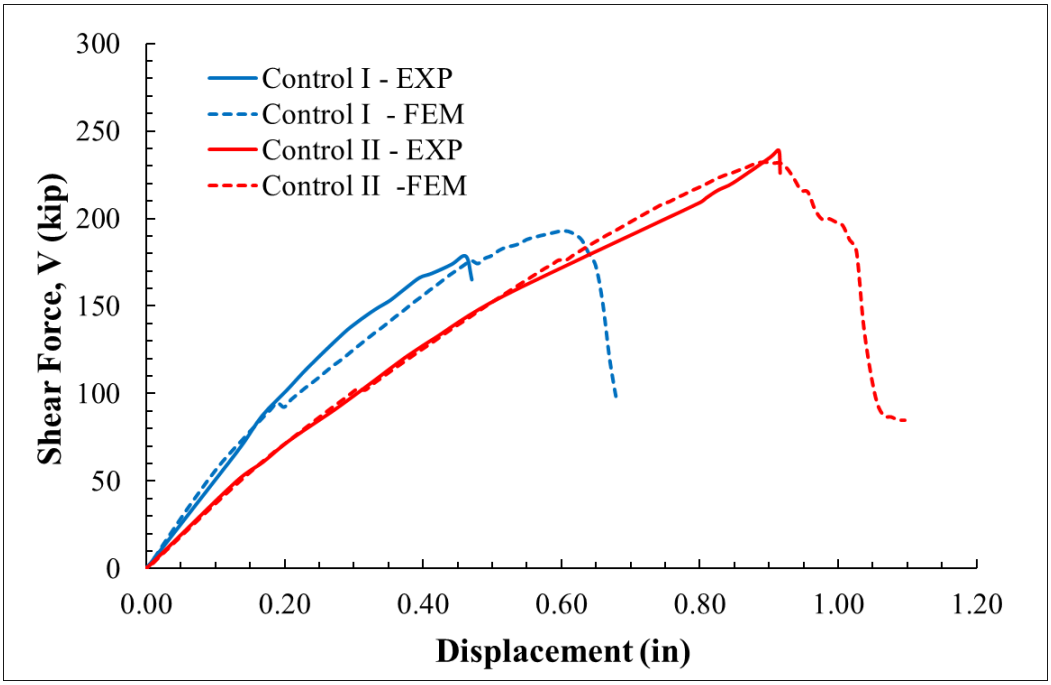

Figure 4-7: Comparison of FE simultion vs. experiment for both control specimens

4.6 Strengthened Specimens

Following the successful validation of the FE model with the control specimens, the numerical modeling was extended to simulate the response of the strengthened specimens.

4.6.1 Strengthening using NSM Bars

The finite element model used is similar to the mesh and associated details shown in Figure 4-2. The only difference is the replacement of cover strips with epoxy and NSM bars. The ATENA documentation specifies that if a bond-slip relationship is included in the model, the stiffness of the epoxy can be incorporated into the bond-slip relationship and therefore does not need to be modeled explicitly around the NSM reinforcement. Simulations were carried out where the epoxy was ignored and when the epoxy was modeled explicitly – the differences in the initial stiffness and peak strength were negligible (see Appendix). Hence NSM bars were embedded in concrete with perfect bond assumed. The resulting mesh is shown in Figure 4-8.

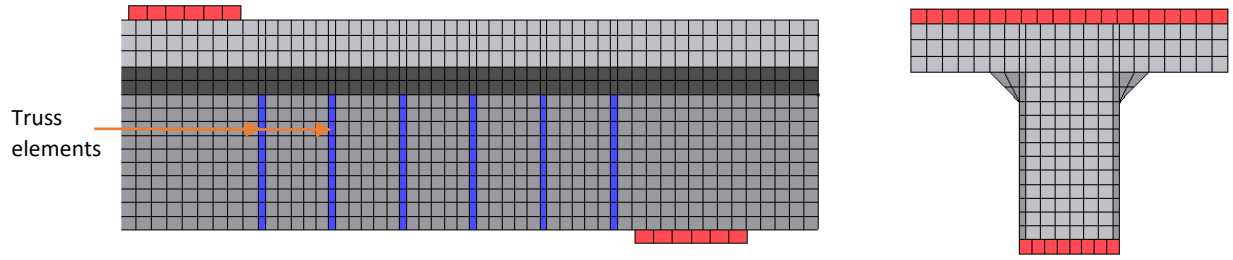

Figure 4-8: Mesh detail for specimen strengthend with NSM

In all, three different strengthening schemes were investigated, as summarized in Table 4-2. In the first phase, the transverse reinforcement in the control specimen consisted of Grade 40 #3 stirrups spaced at 10". In this phase referred to as Scheme NSM 1, #4 (0.5" diameter) FRP bars were also placed at a spacing of 10" wherein an FRP bar on either side of the web was placed mid-way between two stirrups. In the next phase, the transverse reinforcement was increased to #4 bars spaced at 10". Additionally, Grade 60 bars were used. The objective of this phase of the study was to examine the effect of existing shear reinforcement on the effectiveness of the NSM strengthening. Two additional schemes (NSM 2 and NSM 3) were investigated wherein the FRP bars were placed at spacings of 10" and 5", respectively. The resulting shear force vs. displacement response for all three schemes are displayed in Figure 4-9.

Table 4-2: NSM strengthening schemes considered

Label	Stirrup size/spacing (in)	Stirrup yield strength (ksi)	NSM spacing (in)	NSM rupture strength (ksi)
Control 1	#3 @ 10" o.c.	40	-	-
NSM 1	#3 @ 10" o.c.	40	#4 @ 10" o.c.	300
Control 2	#4 @ 10" o.c.	60	-	-
NSM 2	#4 @ 10" o.c.	60	#4 @ 10" o.c.	300
NSM 3	#4 @ 10" o.c.	60	#4 @ 5" o.c.	300

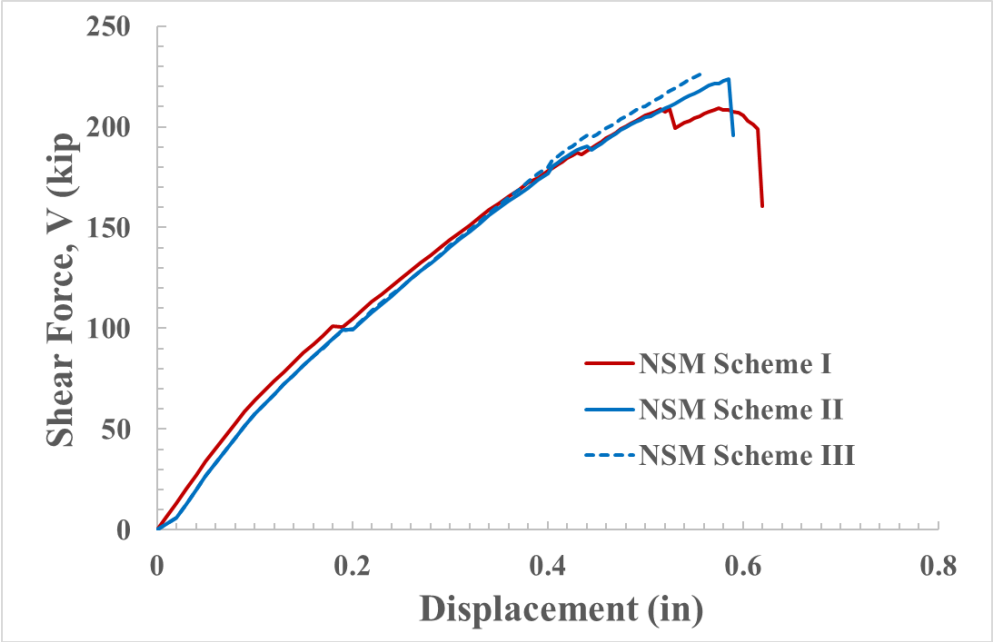

Figure 4-9: Shear force vs. displacement response for all NSM strengthening schemes

Recall, from Section 4.4, the control specimen failed when the shear force in the critical section reached 178 kips. The finite element simulations indicates that NSM strengthening will result in shear enhancements of 17.5% for Scheme 1 but negligible increase in shear strengths for Schemes 2 and 3, respectively. Figure 4-10 shows the variation in strain in the stirrups (see Figure 3-9 for notation) as a function of shear force in the critical section. As expected, all three of the monitored stirrups yield. Also monitored during the FE simulations are the FRP bars used in the NSM strengthening. The variation of the strain in three selected bars is shown in Figure 4-11 – note that these bars correspond to the region where a significant shear crack is evident. The peak strains exceed 5000 micro-strains which is approximately 30% of the ultimate strain of the CFRP bar. Figures 4-12 through 4-15 show similar strain variations in the stirrups and FRP bars for specimens NSM2 and NSM 3, respectively. Finally, the extent and magnitude of cracking for all three strengthened specimens is shown in Figure 4-16.

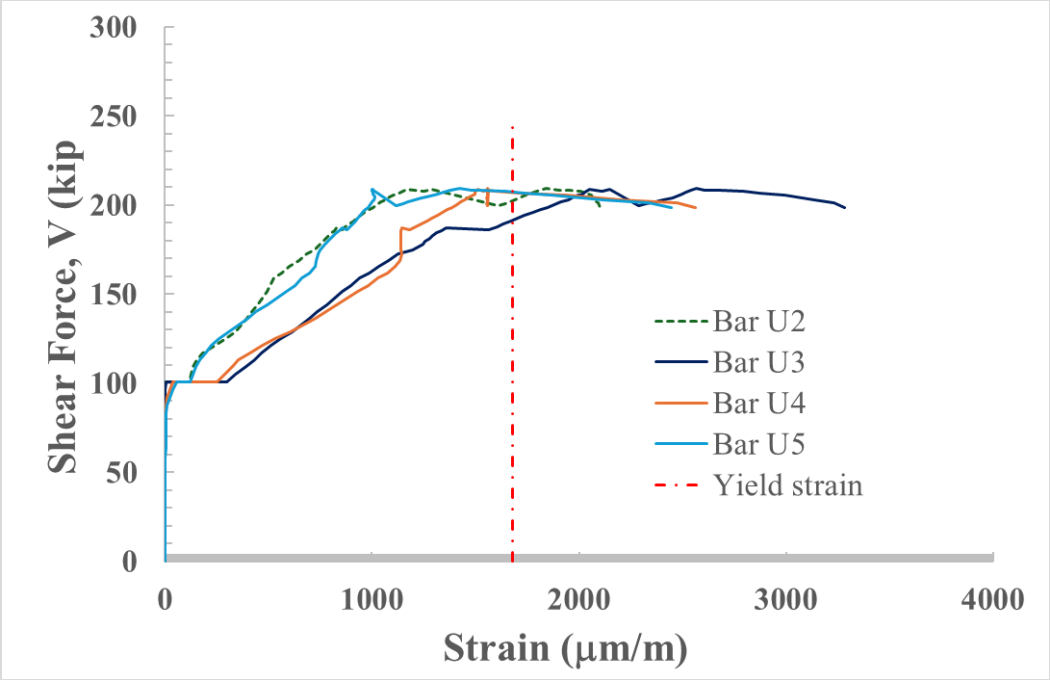

Figure 4-10: Variation of strain in stirrups with increasing shear for specimen NSM 1

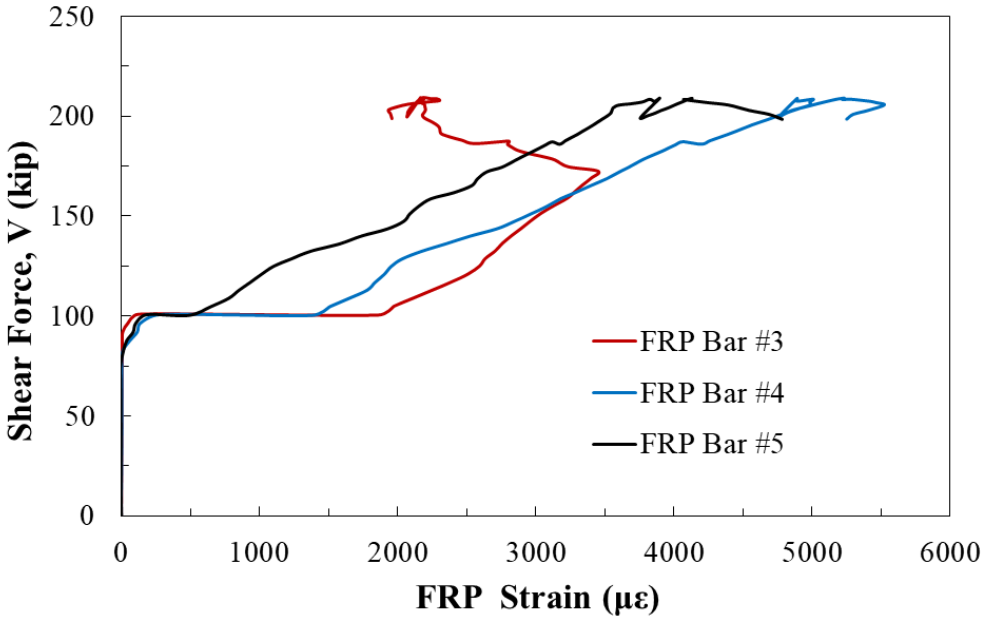

Figure 4-11: Variation of strain in FRP bars with increasing shear for specimen NSM 1

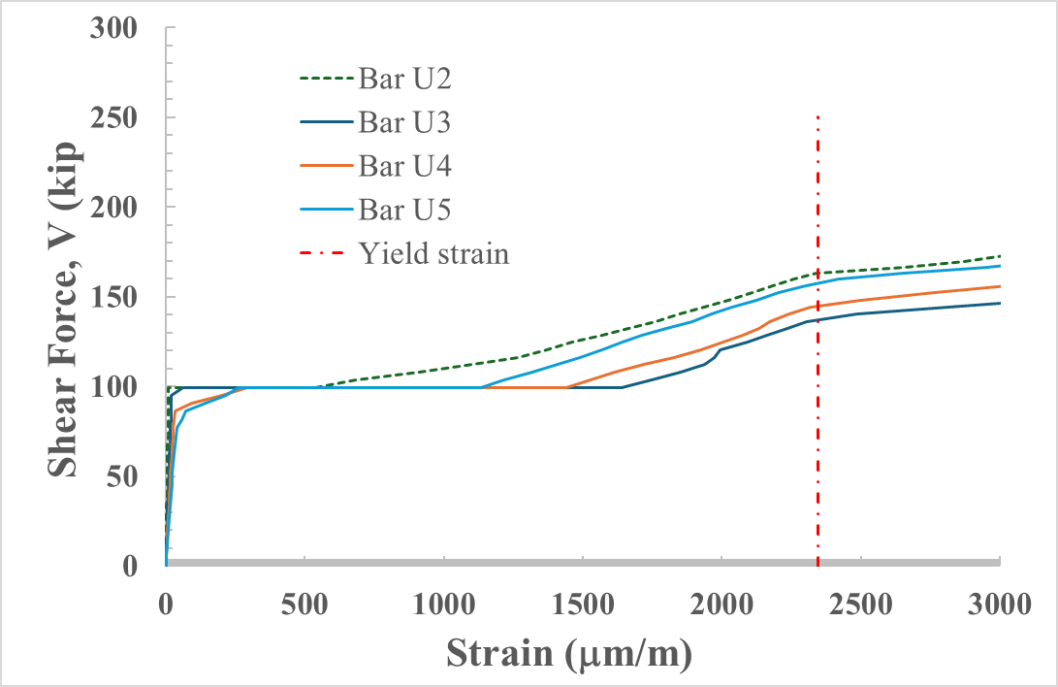

Figure 4-12: Variation of strain in stirrups with increasing shear for specimen NSM 2

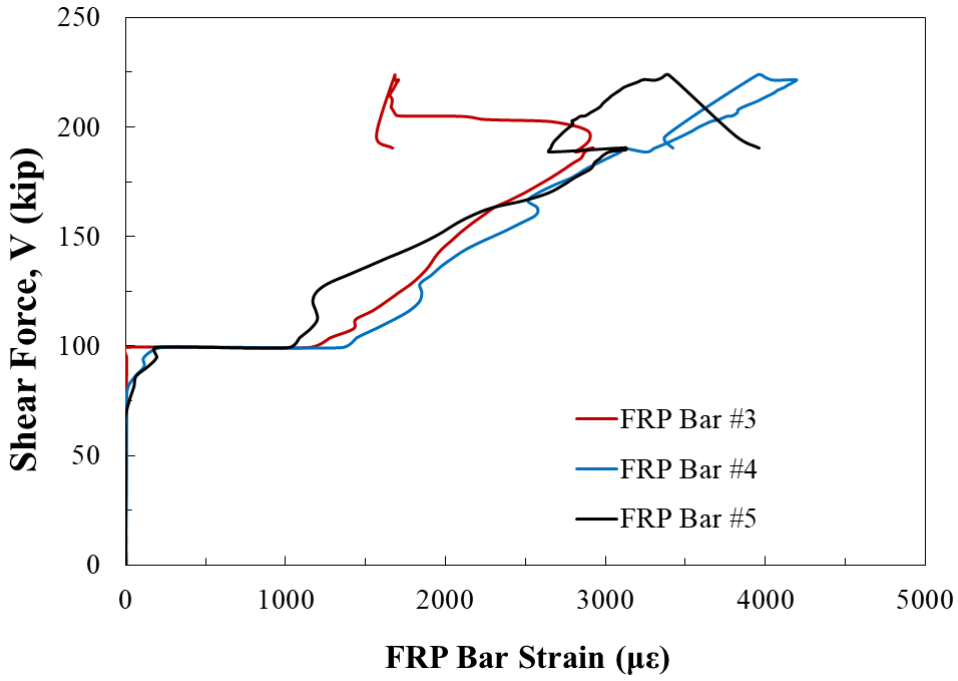

Figure 4-13: Variation of strain in FRP bars with increasing shear for specimen NSM 2

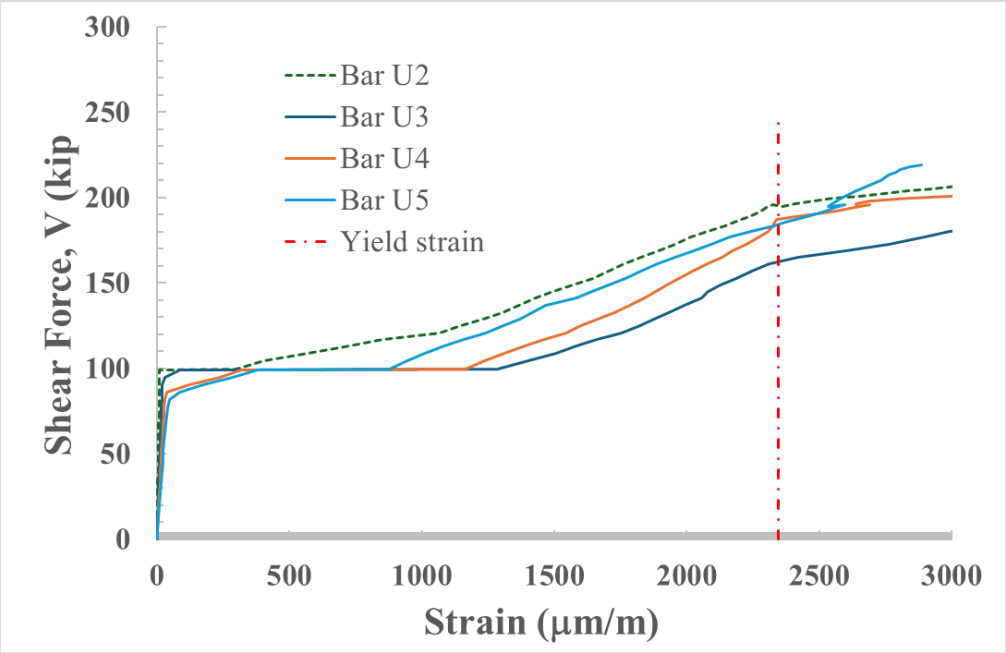

Figure 4-14: Variation of strain in stirrups with increasing shear for specimen NSM 3

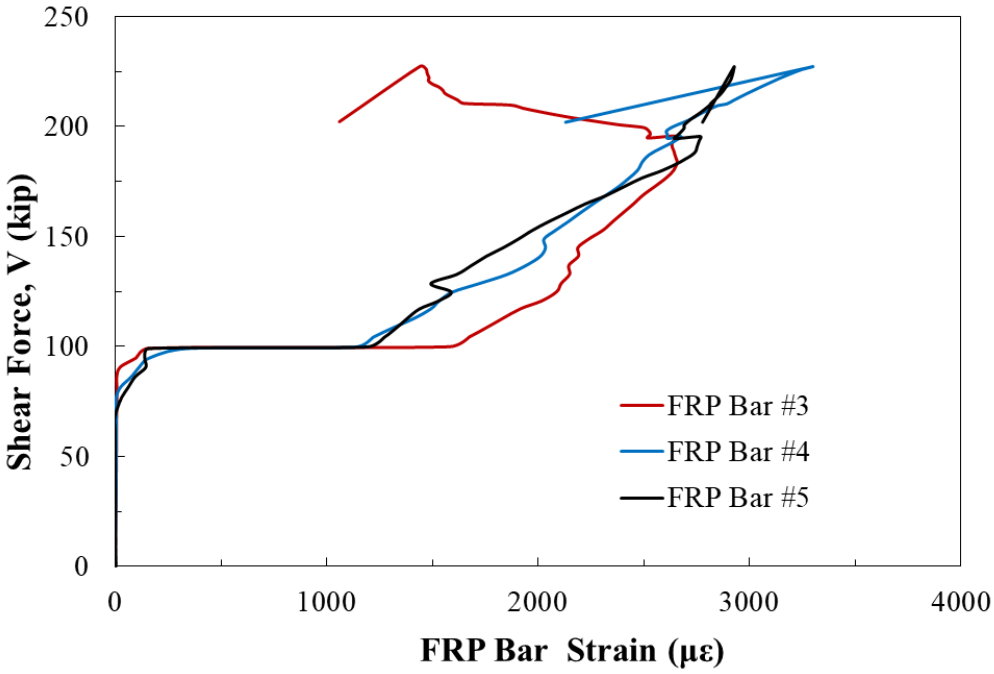

Figure 4-15: Variation of strain in FRP bars with increasing shear for specimen NSM 3

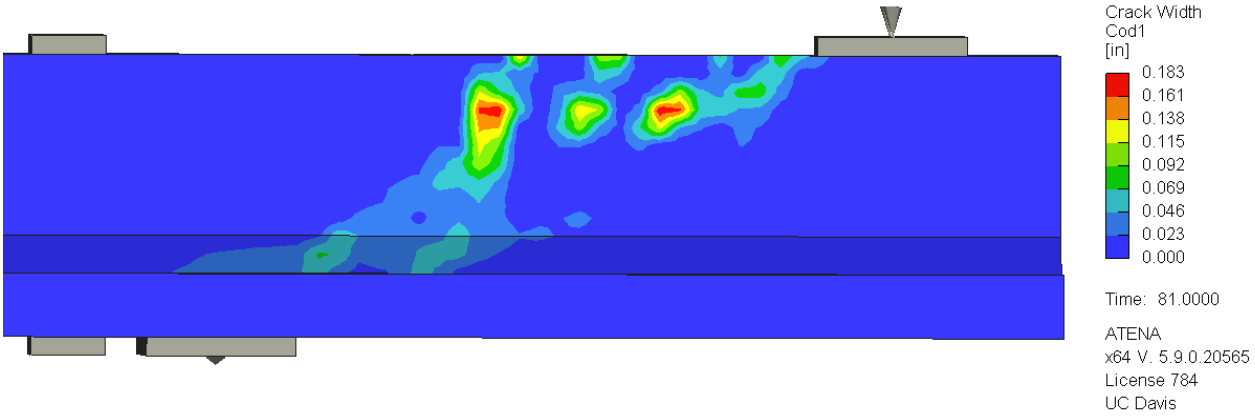

(a) NSM 1 (Shear = 209.2 k)

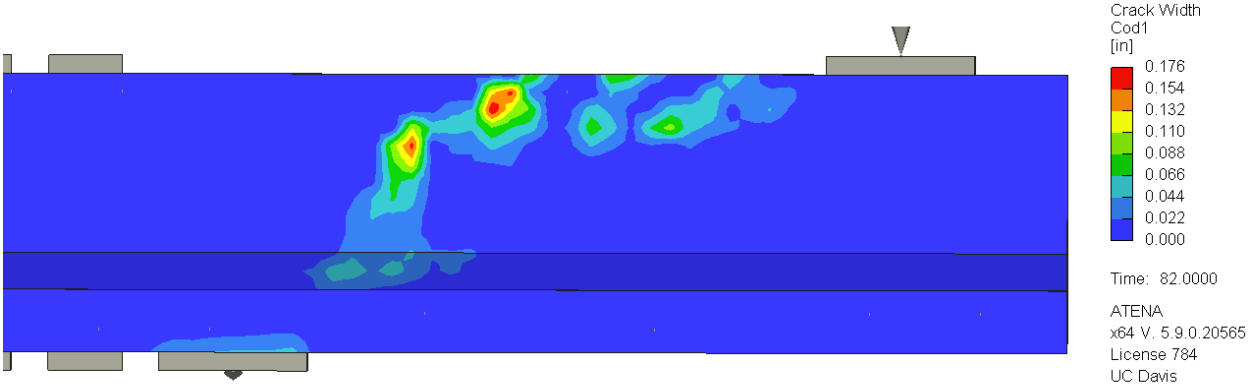

(b) NSM 2 (Shear = 223.6 k)

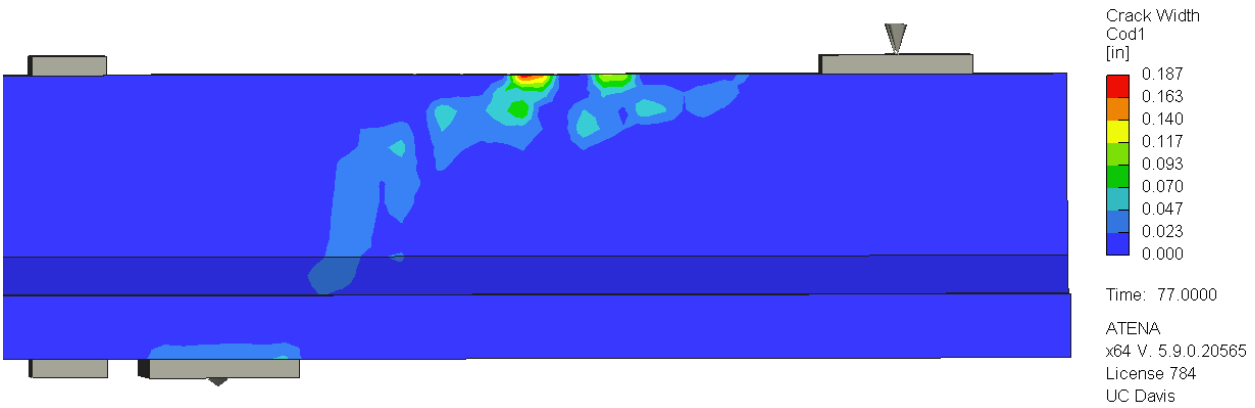

(c) NSM 3 (Shear = 227.3 k)

Figure 4-16: State of cracking in NSM-strengthened specimens at failure

4.6.2 Strengthening using PEBs

The two tests using partially embedded bars were carried out to gain further insight into the effect of increasing the existing shear reinforcement ratio on the overall performance of the shear strengthened girders with PEBs. Cross-sectional and longitudinal reinforcement details in both specimens were identical. However, the shear reinforcement in Control II consists of #4 bars spaced center to center at 10 inches with Grade 60 steel reinforcement compared to Grade 40 #3 bars in Control I. The finite element discretization of both specimens are shown in Figure 4-17.

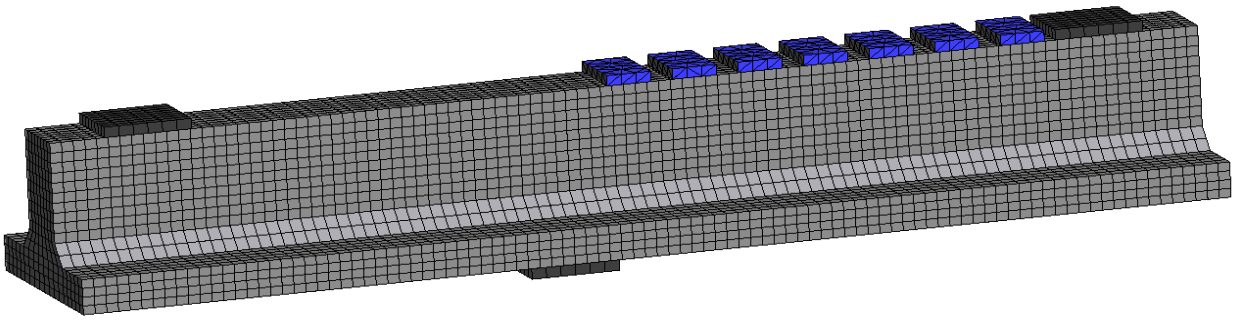

(a)

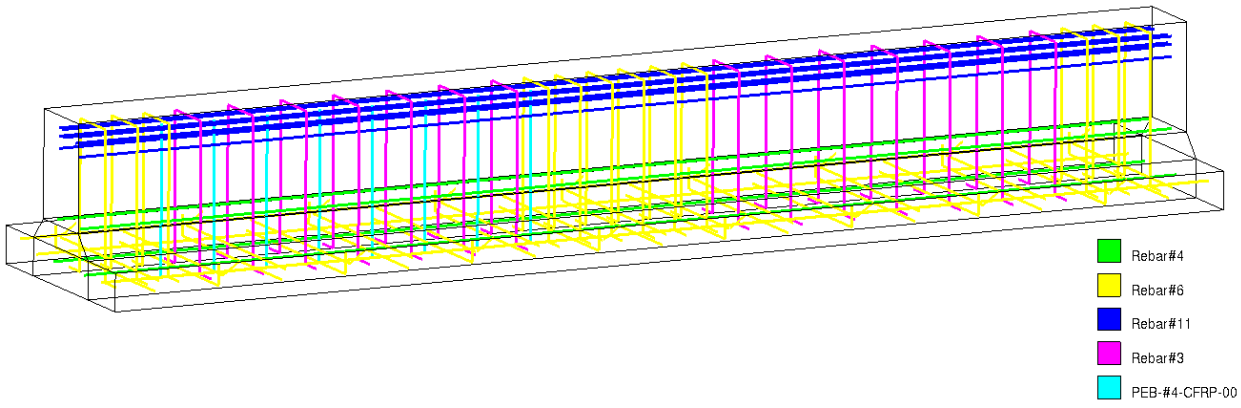

(b)

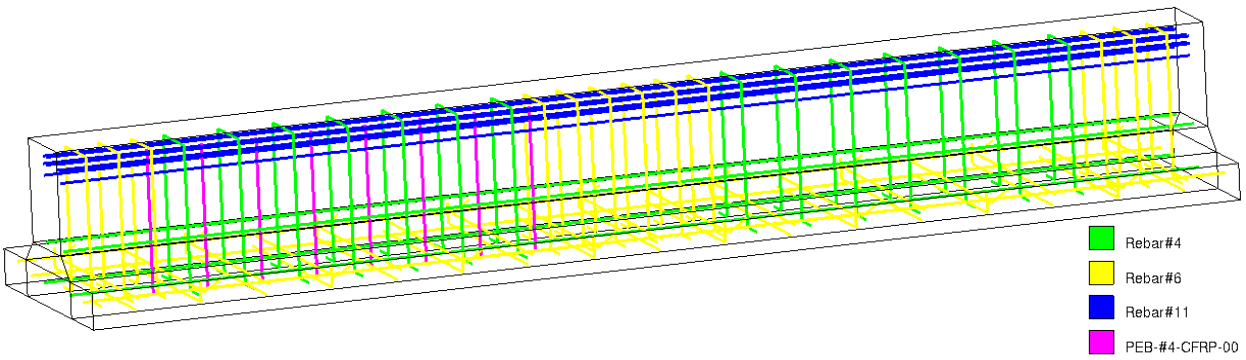

(c)

Figure 4-17: FE model: (a) Phase II specimens with the clamping system, loading, and support plates; (b) #4 CFRP embedded bars with #3 transverse reinforcement; (c) #4 CFRP embedded bars with #4 transverse reinforcement;

Simulated Responses

The numerical (FEM) shear force-deflection response for both strengthened (PEB Scheme I and II) specimens are presented in Figure 4-18. The responses typically consist of an initial elastic branch, the transition to nonlinear behavior, and failure. For PEB I, the FE analysis predicted a 35% increase in shear capacity whereas for specimen PEB II, the increase was only about 18% suggesting an inverse relationship between the quantity of transverse reinforcement and shear enhancement through partially embedded bars. The relationship between the shear force in the simulated specimens and the strains registered in the transverse (shear) reinforcements are shown in Figure 4-19. Additionally, the strain history of each of the PEB CFRP strengthening bar was monitored during the FE analysis and plotted as a function of shear force in Figure 4-20 and 4-21 for specimens PEB I and PEB II, respectively. The PEB bars were labeled from 1 which corresponds to the bar directly beneath the support (reaction) to 8 which correponds to the point of load application. Strains in the bar crossing a major shear crack attained a value of over 9000 micro-strain which is approximately 50% of the ultimate strain of the CFRP bar.

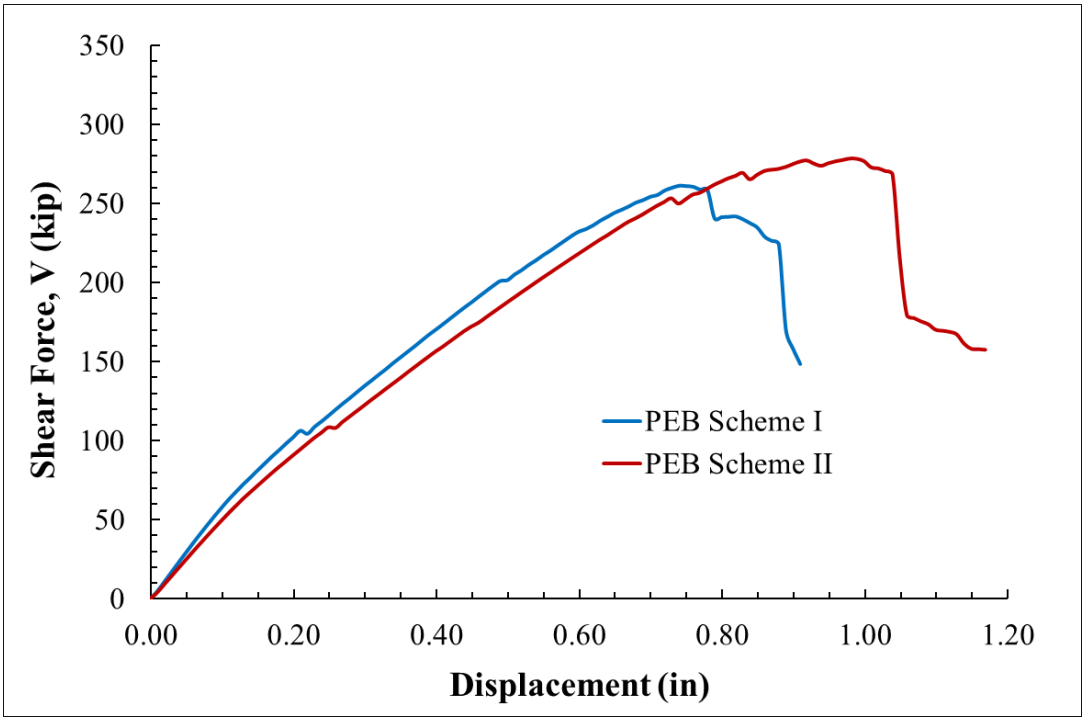

Figure 4-18: Numerically simulated response of specimens strengthened using PEB

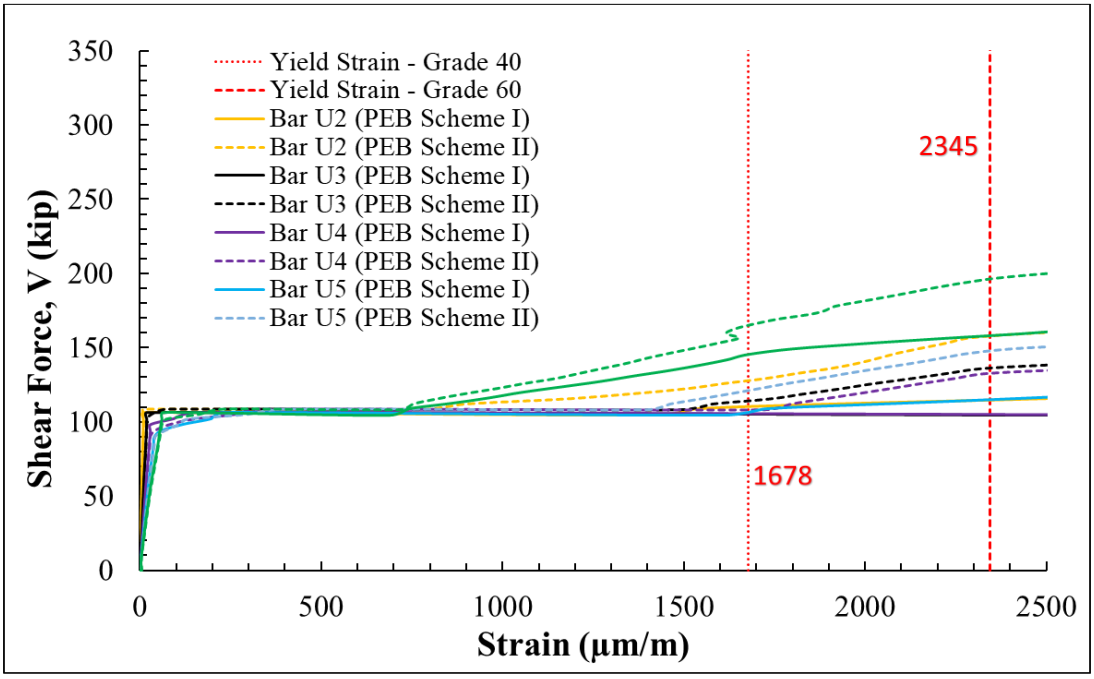

Figure 4-19: Simulated shear force vs. strain in transverse reinforcement

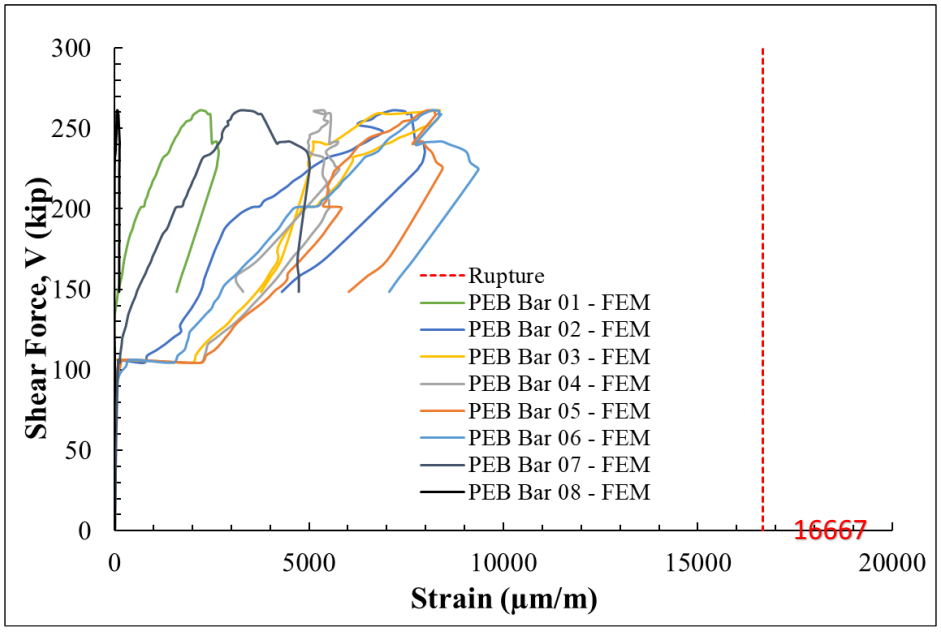

Figure 4-20: Simulated shear force vs. strain in CFRP bars of specimen PEB I

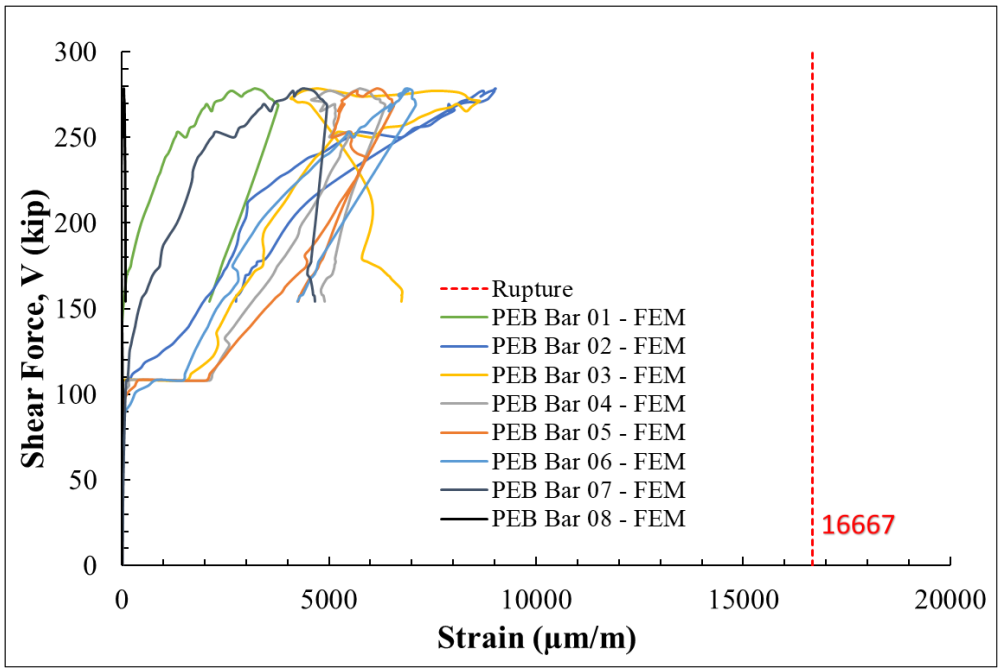

Figure 4-21: Simulated shear force vs. strain in CFRP bars of specimen PEB II

Figure 4-22 shows the simulated crack patterns and crack width at two stages of loading of the strengthened PEB specimens. Overall, it will be observed later that the FEM predictions of the cracking, extent, and orientations of the tested specimens in this phase were comparable to the experimental findings.

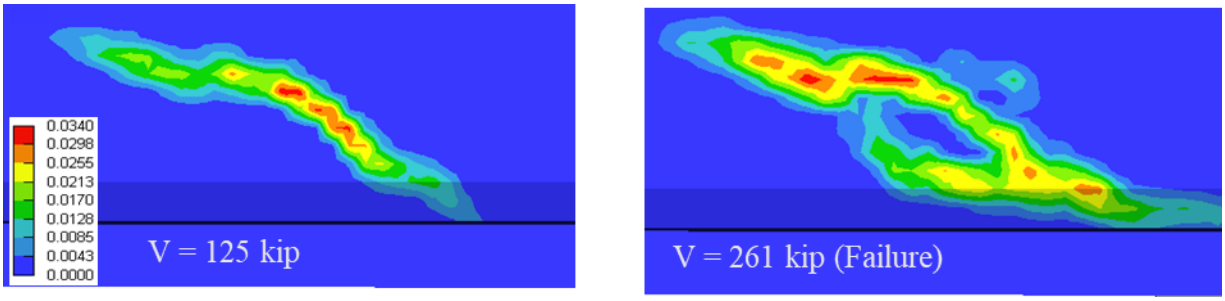

(a) PEB I

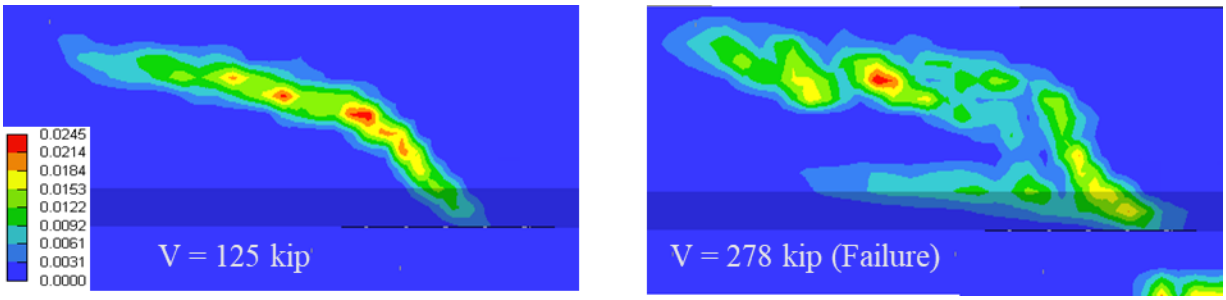

(b) PEB II

Figure 4-22: Crack progression in PEB specimens (legend: crack width in inches)

This chapter summarized the main results of the finite element simulations. Additional details on the modeling, including the incorporation of the epoxy in the NSM study, are provided in the Appendix.

5.0 SHEAR STRENGTHENING METHOD I: NSM FRP BARS

5.1 Specimen preparation

The NSM tests were broken up between phase I and phase II of construction due to lab constraints. The first NSM test, referred to as NSM 1 hereafter, was constructed in phase I along with the first control and PEB tests. The second and third NSM tests (NSM 2 & NSM 3 respectively) were constructed in phase II along with the second control and PEB tests. Specimen dimensions were previously reported in Chapter 3. The differences between phase I and phase II control beam constructions are the concrete strength and steel stirrups used in the test regions. The test parameter for the NSM was varying the spacing relative to the steel stirrups. A complete testing matrix for the NSM tests is included below in Table 5.1.

Table 5-1: Summary of NSM test parameters

Label	f ′c (ksi)	Stirrup size/spacing (in)	Stirrup yield strength (ksi)	NSM spacing (in)	NSM rupture strength (ksi)
C1	6.01	#3 @ 10” o.c.	50.33	-	-
C2	5.24	#4 @ 10” o.c.	68.0	-	-
NSM 1	5.85	#3 @ 10” o.c.	50.33	#4 @ 10” o.c.	300
NSM 2	5.50	#4 @ 10” o.c.	68.0	#4 @ 10” o.c.	300
NSM 3	5.60	#4 @ 10” o.c.	68.0	#4 @ 5” o.c.	300

The NSM rods used in this experiment were commercially available sand-coated and spirally-wound carbon FRP (CFRP) rods with a half-inch diameter. Per the manufacturer’s specifications, the rods have an ultimate tensile stress of 300 ksi and a modulus of elasticity of

18,000 ksi. The epoxy used was a 2-part high viscosity mix with a compressive strength of 13 ksi and tensile strength of 2.7 ksi.

Installation of the NSM rods began 2 weeks after the concrete was poured by cutting 1-inch square grooves into the face of the web using a specialty saw similar to a dado blade, see Figure 5.1 below. The groove dimensions were designed to be 2 times the bar diameter, which was determined to be the optimal ratio from previous testing (Lee & Cheng, 2013). The grooves were then cleaned with a wire brush, flushed with water and then compressed air to remove any debris. Next, the first half of the grooves were filled with epoxy and the NSM rods were pressed in gently with slight vertical movement to ensure there were no air pockets behind the rod. Then the epoxy was allowed to get an initial set and the remainder of the groove was filled and smoothed roughly even with the face of the concrete. Note that the high viscosity epoxy was selected to allow for placement in the vertical grooves without excessive sagging.

Figure 5-1: Multi-bladed circular saw with diamond blades for cutting concrete

In addition to the strain gauges on the longitudinal bars and steel stirrups, strain gauges were added to the NSM bars near the predicted path of the major shear crack. 4 strain gages were attached to the most likely bar to cross the major shear crack in order to monitor any debonding that might occur along its length. The remaining two gauges were placed at the mid-point of the web on the next two bars for comparison to the adjacent steel stirrups. The layout of the gauges

is shown in Figure 5.2 below. The gauges were labeled 31, 32, 33, 34, 41, and 51 to where the first number indicated which bar they are attached to in the NSM 1 and 2 tests, and the second number is their order descending vertically on the bar. For NSM 3 the numbering was kept the same and location along the span is similar to allow for comparison between the tests.

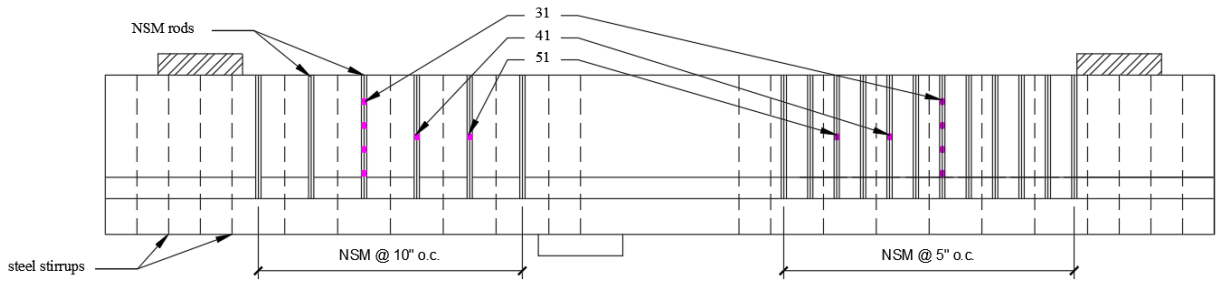

Figure 5-2: NSM strain gauge layout for NSM at 10 inches on center (left) and NSM at 5 inches on center (right).

5.2 Results of testing

The objective of phase I was to confirm the viability of the NSM method of shear strengthening on a practical size beam (a vast majority of previous NSM research used beams with depths <16 inches) and to compare the performance of NSM to the PEB method. In phase II, the objective was to evaluate the effectiveness of the NSM method with a higher steel reinforcement ratio. The second objective was to test if doubling the amount of NSM used would provide additional strength or change the failure mode as compared to the first two NSM tests. The failure modes of each test are discussed in more detail in the following sections.

5.2.1 Strengthening scheme I

As with the control specimens, a monotonically increasing load was applied to the beam through the hydraulic jack bearing on the floor. This resulted in tension on the top face of the girder, which is the bottom of the web. To start the test, the applied load was gradually increased up to 100 kips (corresponding to a shear of 59 kip in the critical section). From that point, the load was increased in increments of approximately 25 kips to monitor the progression of cracks

in the web. The first flexural and web shear cracks both developed at an applied load of 145 kips shown in Figure 5.3 (b). As loading continued, the flexural cracks extended to the mid-height of the web but remained less than 1 mm wide. Likewise, the web shear crack did not exceed a thickness of 1 mm but continued to lengthen in the spaces between the second, third, and fourth NSM bars (counting from the right side of the pictures, which was the supported end of the beam). Secondary shear cracks developed in the spaces between the remaining NSM bars and near the support (top right of pictures). By the time the load reached 350 kips, the cracks between the second and fourth NSM bars began to widen (< 2 mm) and extend into the flange in the direction of the load point (located out of frame in the bottom left corner of the pictures). At this point, the main shear crack had also crossed the third NSM bar.

a) Shear = 0 kip (Applied load = 0 kip)

b) Shear = 85 kips (Applied load = 145 kips)

c) Shear = 147 kips (Applied load = 250 kips)

d) Shear force = 208 kips (Applied load = 355 kips)

Figure 5-3: Crack pattern progression in test region for NSM 1

Failure occurred abruptly at a load of 381 kips with a corresponding shear load of 223 kips as shown in Figure 5.4. At failure, the main shear crack in the web and the largest crack in the web opened significantly and the load abruptly dropped. At failure NSM bars 3 and 4 intersected the primary shear crack. To the right of NSM bar 3, the shear crack turned near vertical and passed behind NSM bars 1 and 2 as shown in Figure 5.5.

Shear force = 223 kips (Applied load = 381 kips)

Figure 5-4: Crack pattern at failure in test region for NSM 1

Figure 5-5: Crack pattern at top face of web, steel support (left), NSM bar 1 (middle left), and NSM bar 2 (center).

The shear displacement graph for NSM 1 is given in Figure 5.6 along with the response for Control 1 for comparison. Since the self-weight is negligible compared to the applied load, the shear force is considered constant in the test span. The displacement was measured at the point of load application. The initial stiffness of the two tests was very similar, but the NSM test exhibited higher stiffness after the shear cracks started to propagate. The peak displacements were similar, but the NSM test had a failure load of 223 kips compared to 178 for the control. It is generally accepted that the FRP contribution can be determined by the equation given below:

$$V_f = V_{fu} - (V_{control}) \tag{5.1}$$

where V_f is the experimental failure load, V_{fu} is the FRP shear contribution, and $V_{control}$ is the total shear contributions from the concrete and steel, which corresponds to the shear capacity of the control specimen. The calculated FRP shear contribution is 44.7 kips, which corresponds to a 25 percent increase in shear capacity of the NSM test relative to the control.

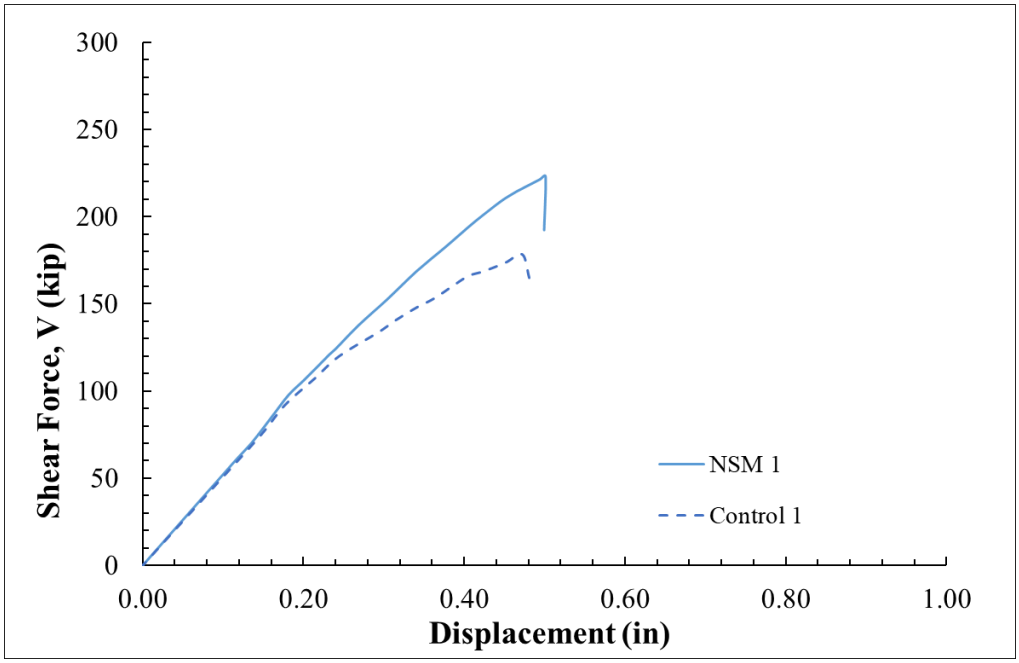

Figure 5-6: Shear-displacement response for NSM 1

As stated previously, the strains in various reinforcing bars were also monitored during the test. Figure 5.7 shows the strain in the main longitudinal reinforcement compared between the control and NSM tests. In both cases, the bars remained well below their yield strains, indicating a shear-controlled failure.

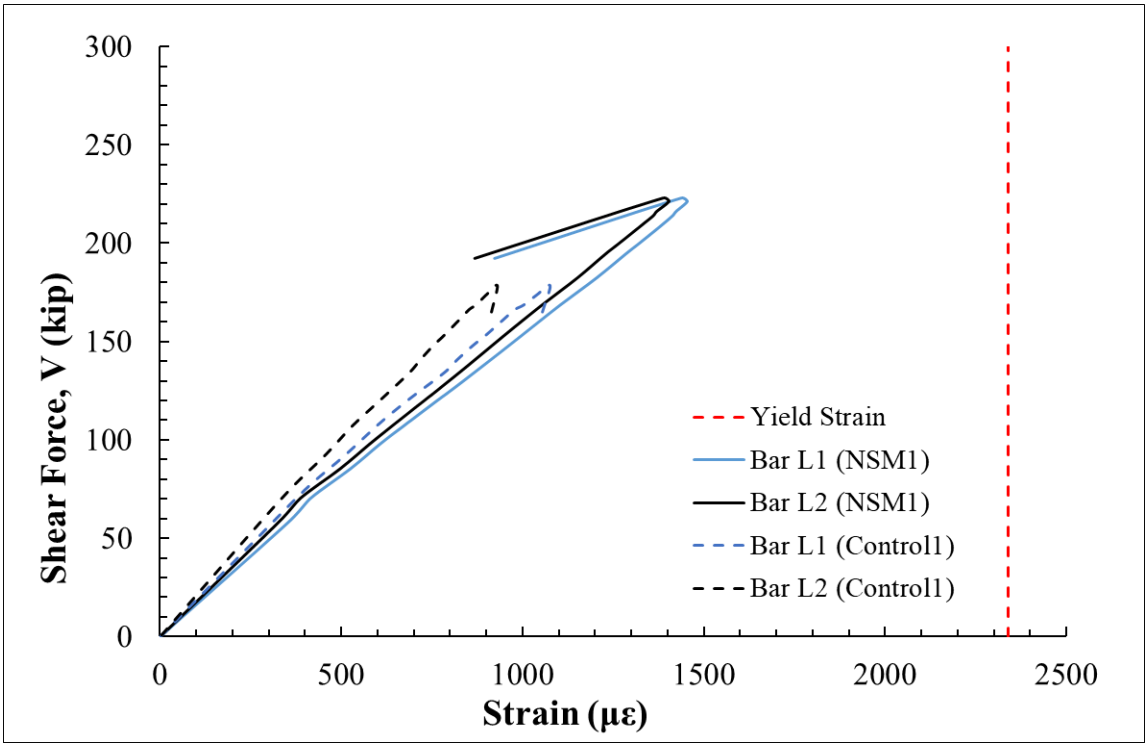

Figure 5-7: Strain versus shear force in main longitudinal reinforcement

Strain in the steel stirrups was also monitored during the tests. Figure 5.8 shows the strain in the steel stirrups compared between NSM 1 and Control 1. The labeling convention starts with U1 (not shown) nearest the support and U6 is the bar closest to the point of load application. Many of the bars yielded (strain at yield is indicated by the red dashed line on the figure), and the shear force for a given strain tended to be higher for the NSM test because of the added capacity of the NSM bars. The gauge on U6 in the Control specimen likely failed during the test.

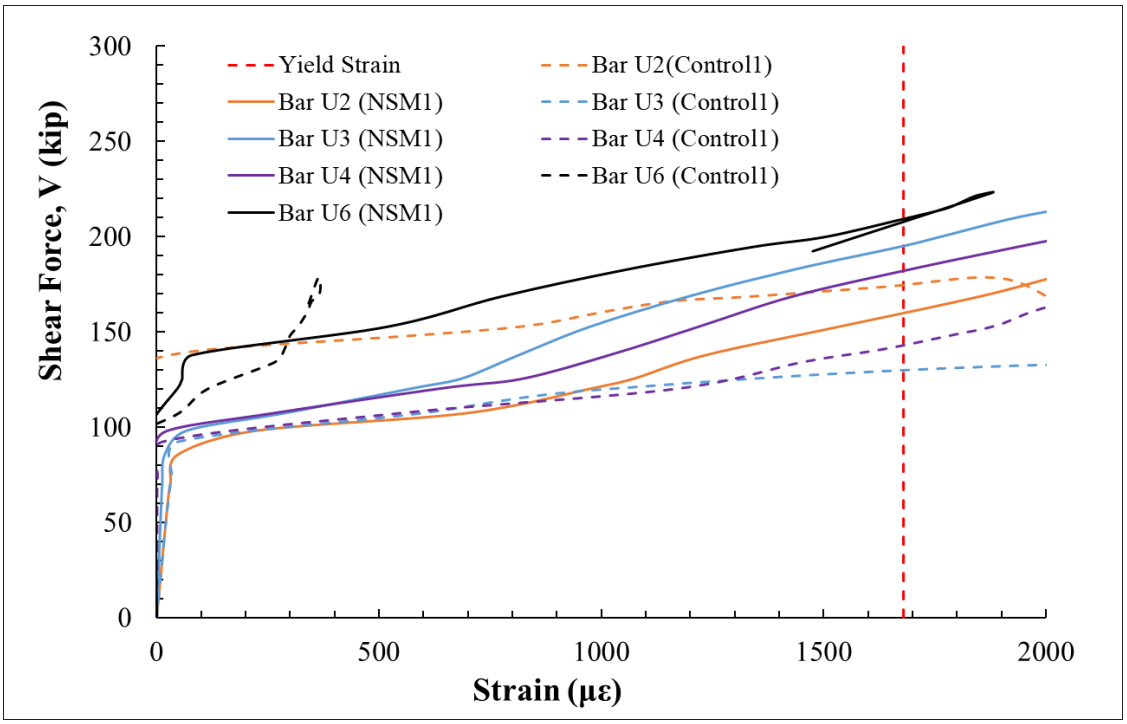

Figure 5-8: Strain-shear force plot in steel stirrups in test region

The strain in select NSM bars was also monitored. Figure 5.9 compares the strain in the NSM reinforcement to the adjacent steel stirrups. It is worth noting that, as shown in Figure 5.2, the NSM bars are staggered at a half spacing between stirrups to minimize stress concentrations in the cover. This results in NSM bar 3 being placed between U3 and U4 for example. Generally, the NSM bar strain was similar to that of the steel stirrups, with the notable exception of FRP 33 which was the closest to the major shear crack. The maximum strain recorded in FRP 33 was 5526 με which is 33 percent of the ultimate strain of the bar. This is a typical strain value for NSM debonding, so it is possible that local debonding occurred in NSM 3 near the shear crack, though no destructive testing was done to confirm debonding occurred.

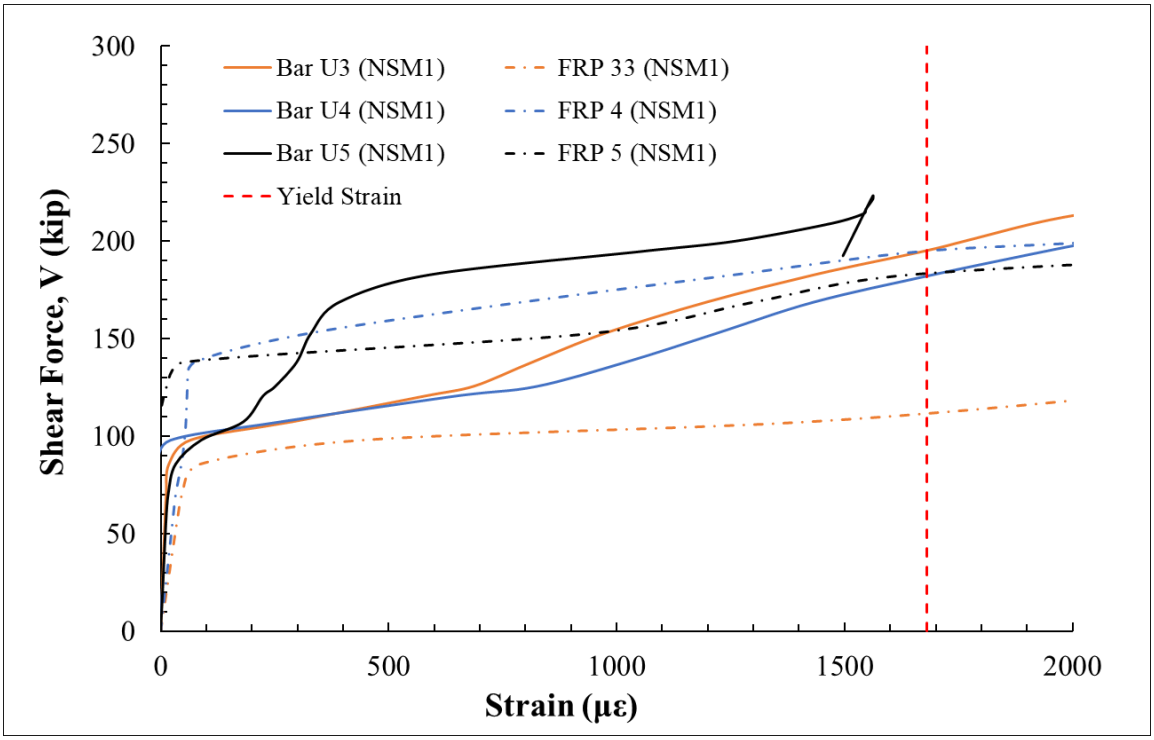

Figure 5-9: Strain-shear force plot for steel stirrups and NSM bars in test region

5.2.2 Strengthening scheme II

The second NSM test, NSM 2, had the same CFRP configuration as NSM 1 with a higher steel reinforcement ratio. Loading was conducted in a similar fashion to NSM 1, where loading started with a 100 kip force being applied and then loaded in 25 kip increments thereafter. The first flexural and web shear cracks both developed at an applied load of 145 kips (corresponding to a shear in the section of approximately 85 kips). The flexural cracks appeared at the top of the web aligned over the loading jack. The web shear crack formed between the third and fourth NSM bars (counting from the right side of the pictures, which was the supported end of the beam) shown in Figure 5.10 (b). With higher loads, the flexural cracks extended to the mid-height of the web, but remained less than 1 mm wide. The web shear crack widened slightly, but continued to lengthen in the space between the third and fourth NSM bars. Secondary shear cracks developed in the spaces between bars 1 and 3 near the support (Figure 5.10 c). Between 375 and 400 kips of load (235 kip shear force), two parallel cracks between the third and fifth NSM bars began to widen (< 2 mm) and cross NSM bar 4 horizontally. The lower of these two

cracks also began to extend into the flange and secondary cracks had developed between all other NSM bars shown in Figure 5.12 d.

a) Shear force = 0 kip (Applied load = 0 kip)

b) Shear force = 85 kips (Applied load = 145 kips)

c) Shear force = 147 kips (Applied load = 250 kips)

d) Shear force = 235 kips (Applied load = 400 kips)

e) Shear force = 249 kips (Applied load = 424 kips)

Figure 5-10: Progression of crack pattern in test region for NSM 2

Failure occurred abruptly at a load of 424 kips with a corresponding shear force of 249 kips. At failure, the upper of the two significant shear cracks opened abruptly including crossing the NSM epoxy and the load abruptly dropped. The two cracks did not fully join at failure, where the upper separated the web and the lower extended into the chamfer. Unlike the previous test, the shear crack did not extend into the flange. At the top of the web, the shear crack passed behind NSM bars 3, 2, and 1 deeper (further back from the face of the web) than the previous test, as shown in Fig. 4.11.

Figure 5-11: Top face of web at failure for NSM 2

The shear displacement graph for NSM 2 is presented in Figure 5.12 below, along with the same plot for Control 2 for comparison. The loading and displacement measurement was identical to all previous tests. Though the curves are slightly offset, the stiffness between the control and NSM tests were similar. The behavior matched the phase I experiment where the concrete began to crack at roughly 150 kips, the control began to soften while the NSM test remained more linear until failure. The peak displacement was significantly less for the NSM 2 test at 0.76 inches verse 0.91 inches for the control test. The peak shear forces were almost identical, with 248 kips for the NSM 2 test and 239 kips for the control. This leads to a calculated FRP shear strength, V_f, of 10 kips, which is much lower than expected.

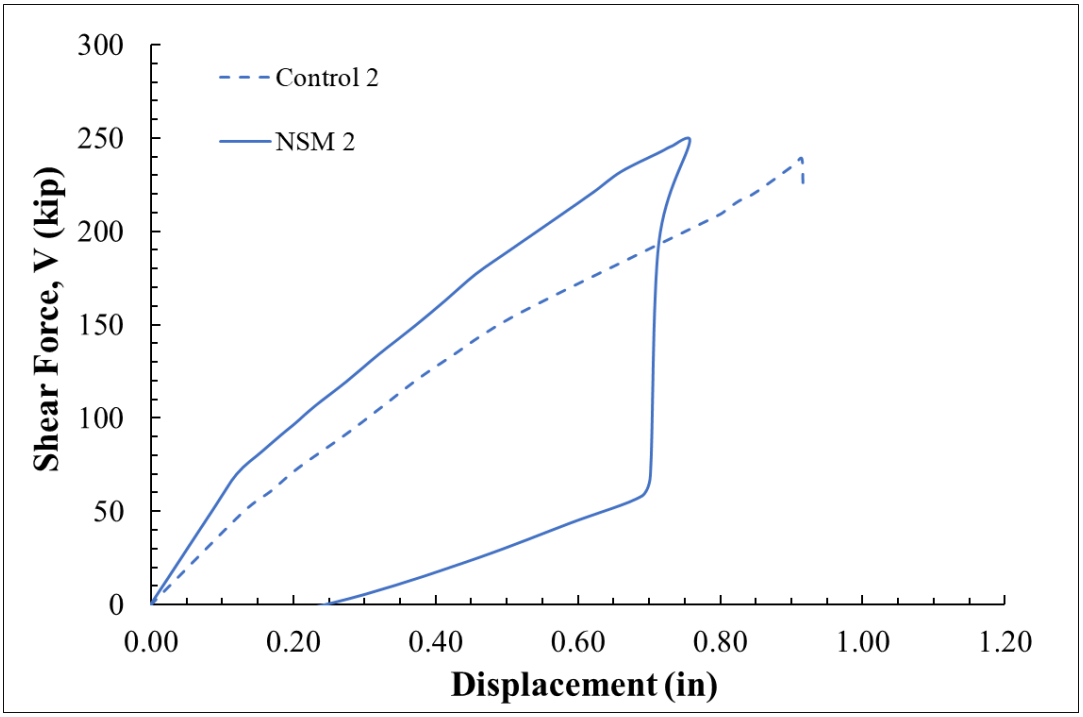

Figure 5-12: Shear-displacement response for NSM 2

Similar to the phase 1 results, the longitudinal bars remained well below their yield strains, indicating a shear-controlled failure as shown in Figure 5.13. Both the control and reinforced tests displayed larger longitudinal strains, but that was expected to the increase in shear capacity of the phase II control. Figure 5.14 shows the strain in the steel stirrups compared between NSM 2 and Control 2. The labeling convention starts with U1 (not shown) nearest the support and U6 is the bar closest to the point of load application. Most of the bars yielded and the strains from NSM 2 were consistent with the results from phase I. The gauge on U6 NSM 2 was damaged prior to the start of the test and recorded no data.

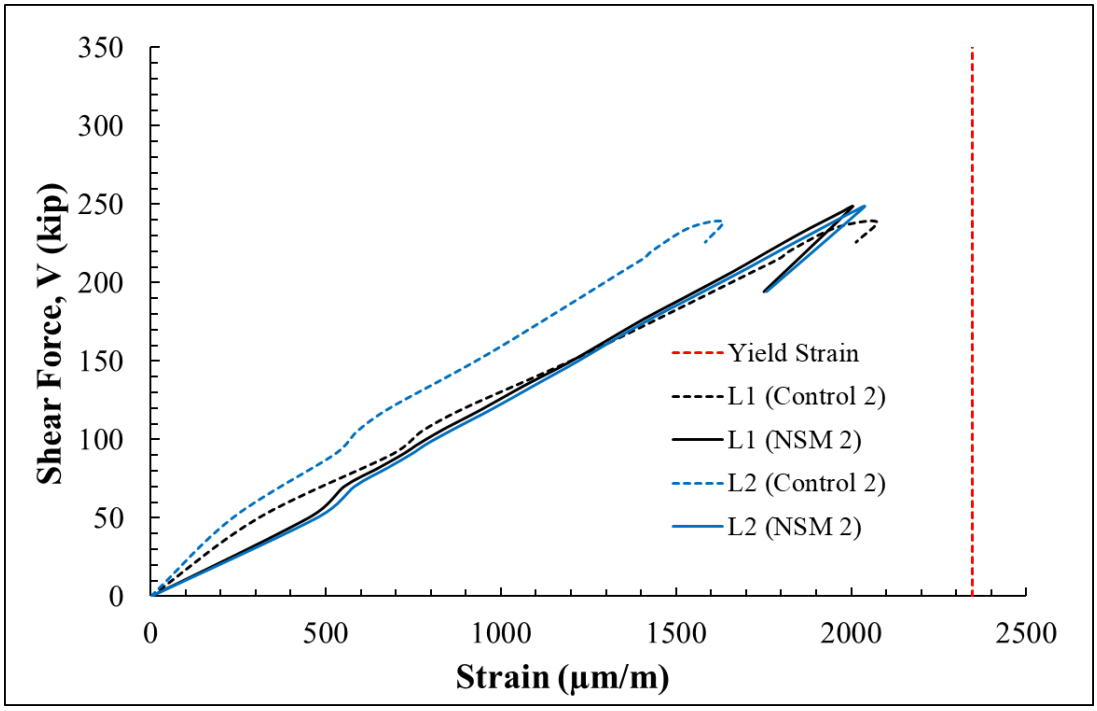

Figure 5-13: Strain vs. shear force plot for main longitudinal reinforcement

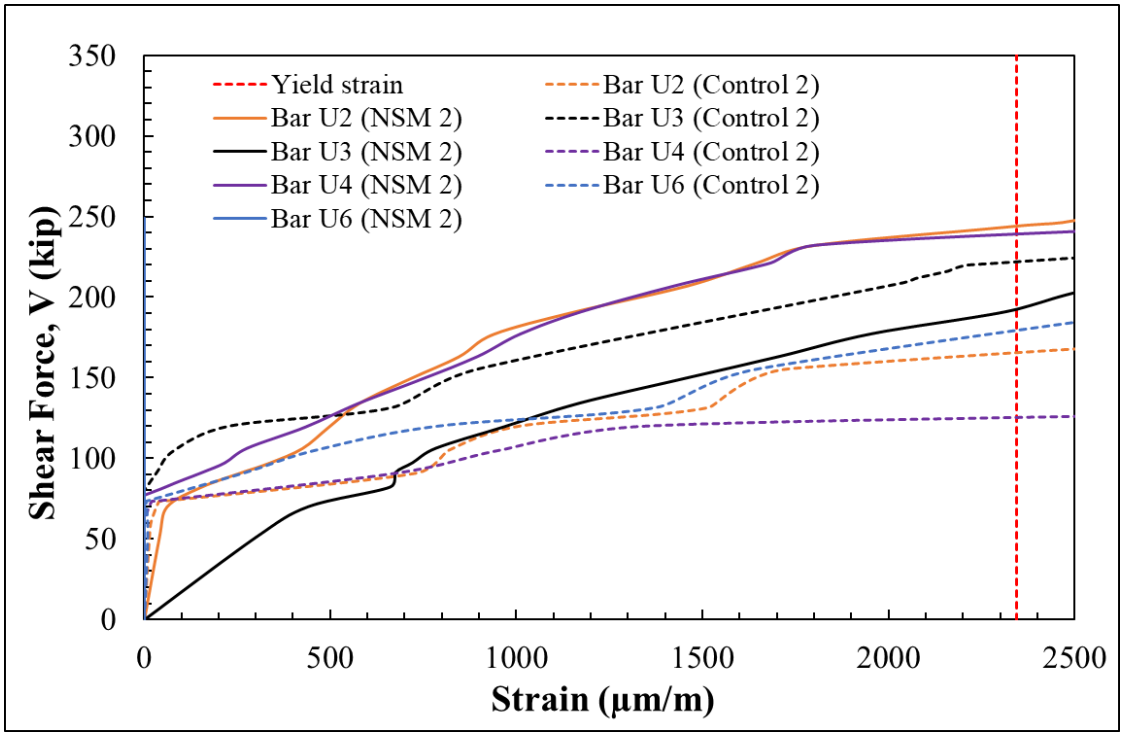

Figure 5-14: Strain vs. shear force plot for steel stirrups in test region

The strain in select NSM bars was also monitored at similar locations to NSM 1, as shown in Fig. 4.2. Figure 5.15 compares the strain the NSM reinforcement to the adjacent steel stirrups. NSM bars 4 and 5 behaved similarly to the adjacent stirrups, but the strain NSM 33 started to decline prior to failure. Looking at the pictures after the test, it appears that the shear crack developed behind NSM bar 3 around the load level when the strain started to decline, see the top of Figure 5.13. This indicates a side cover detachment failure, as the rod was not able to fully develop its strength at failure but debonding was not observed. The major shear crack did cross NSM bar 4 near the mid height of the web, as shown in Figure 5.10 e. The maximum strain recorded in bar 4 was 4544 με which is 27 percent of its ultimate strain.

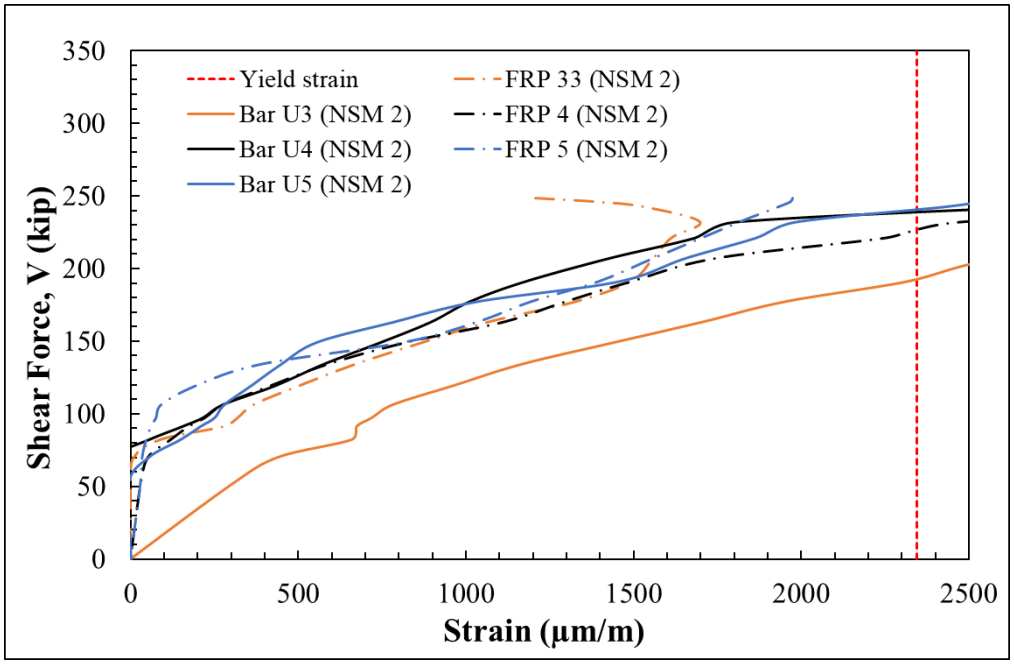

Figure 5-15: Strain vs. shear force plot for steel stirrups and NSM bars in test region

5.2.3 Strengthening scheme III

The third NSM test, NSM 3, had twice as many CFRP as NSM 1 and 2, with a spacing of 5 inches on center and the same steel reinforcement as NSM 2. Loading was conducted in a similar fashion to the previous tests. Both flexural and web shear cracks both developed at a load of approximately 150 kips. The flexural cracks appeared at the top of the web aligned over the loading jack and between some of the NSM grooves near the loaded end. The web shear crack formed between the fifth and sixth NSM bars (counting from the left side of the pictures, which was the supported end of the test region) shown in Figure 5.16 b below.

a) Shear force = 0 kips

b) Shear force = 103 kips

Figure 5-16: Crack pattern progression in test region for NSM 3

As the load continued past 200 kips, very narrow (< 0.4 mm) shear cracks developed between the first and eight NSM bars (Figure 5.12c). Unlike previous tests, near vertical flexural cracks at the top of the web between the sixth and eighth NSM bars developed and continued to widen. The shear cracks in the mid height of the web grew only minimally, with the largest cracks developing in the chamfer in the spacings beneath the vertical cracks, see Figure 5.16 d. Failure (see Fig. 4.17) occurred abruptly at a load of 417 kips with a corresponding shear load of 244 kips.

c) Shear force = 191 kips

d) Shear force = 234 kips

Figure 5.16 (continued): Crack pattern progression in test region for NSM 3

Shear force = 244 kips

Figure 5-17: Crack pattern at failure in test region for NSM 3

At failure, the vertical crack between NSM bars 7 and 8 extended straight down to connect with secondary cracks in the chamfer. At the same time two large horizontal cracks developed in the flange starting from the loading point, similar to the control tests and NSM 1. The major crack did not cross any of the NSM bars with a significant development length, only crossing at bar 8 about 3 inches from the end of the NSM rod (in the beam chamfer). At the top of the web, the shear crack passed behind NSM bar 7 and all subsequent bars to the support as shown in Figure 5.18. It is worth noting here that the first two NSM tests experienced relatively symmetric crack patterns on each face of the web. However, NSM 3 had some asymmetry at failure. The opposite face of the web (see Fig. 4.19) had a more inclined crack pattern that effectively intersected NSM bars 5 and 6 and there were signed that debonding of the NSM had occurred in bar 5 (where the 31-34 strain gauges were applied). Additionally, the horizontal cracks in the flange did not propagate more than half the transverse width of the flange.

Figure 5-18: Top face of web at failure for NSM 3

Figure 5-19: Failure pattern of NSM 3 with debonded NSM

The behavior of NSM 3 was very similar to that of NSM 2, as shown in Figure 5.20. The load and displacement were measured identically to all previous tests. The peak load and displacement were almost identical to NSM 2, despite having twice as much NSM reinforcement. The maximum shear force for NSM 3 was 244 kips and 239 kips for the control.

This leads to a calculated FRP shear strength, V_f, of 5 kips, which is much lower than expected but similar to NSM 2.

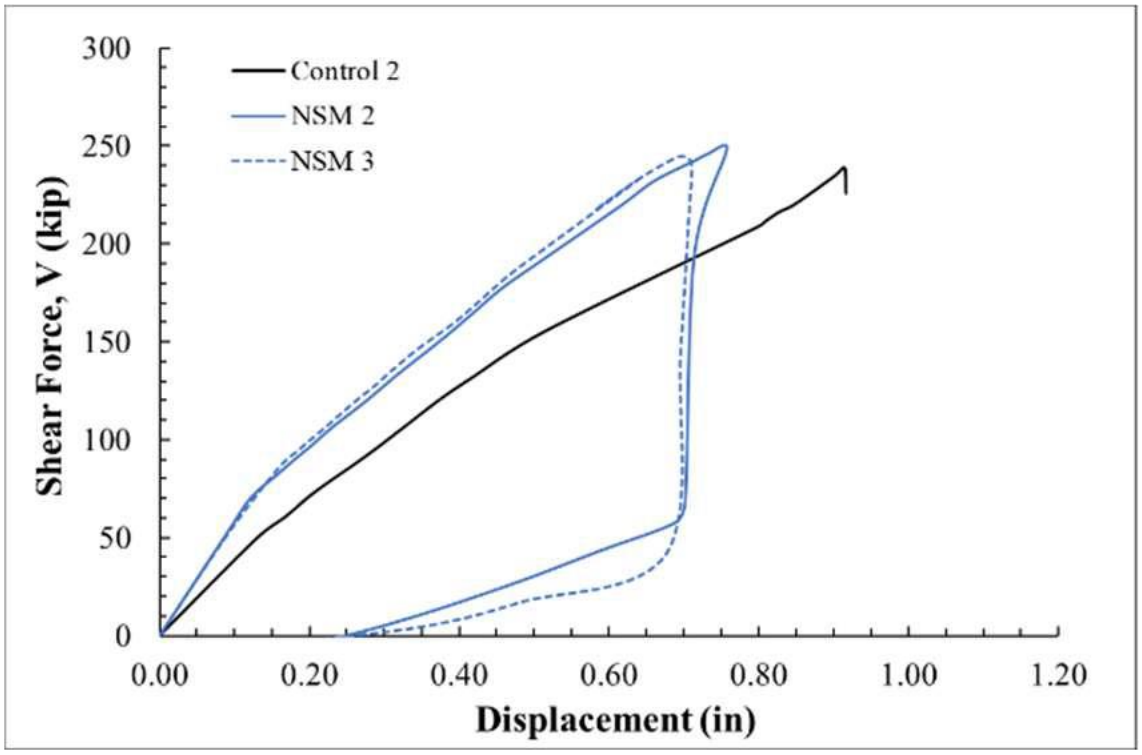

Figure 5-20: Shear-displacement response for NSM 3 and comparison with NSM2 and control test

Figure 5.21 shows that the longitudinal bars stayed well below their yield strength. L2 for NSM 3 did not record any strain values for this test, as it was likely damaged prior to the start of loading. Figure 5.22 shows the strain in the steel stirrups compared between NSM 3 and Control 2. The labeling convention starts with U1 (not shown) nearest the support and U6 is the bar closest to the point of load application. The strains from NSM 3 were consistent with the results from phase I. Similar to the previous tests, most of the bars yielded except NSM U6.

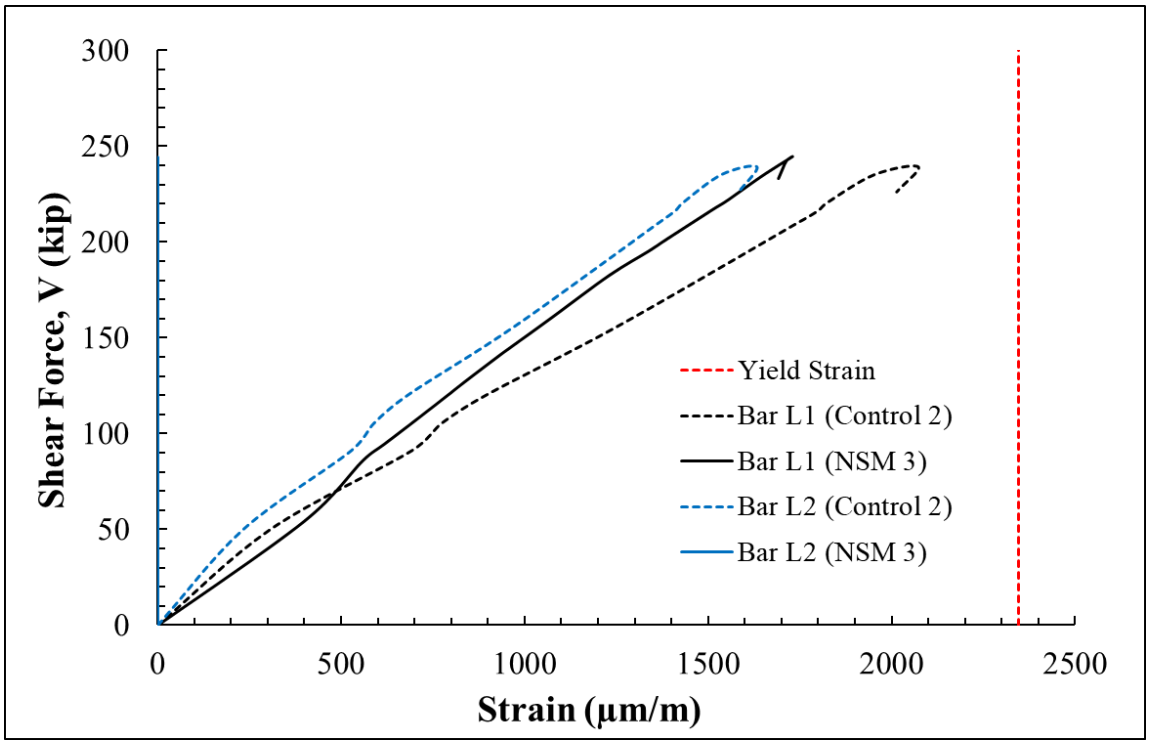

Figure 5-21: Strain vs. shear force plot for main longitudinal reinforcement

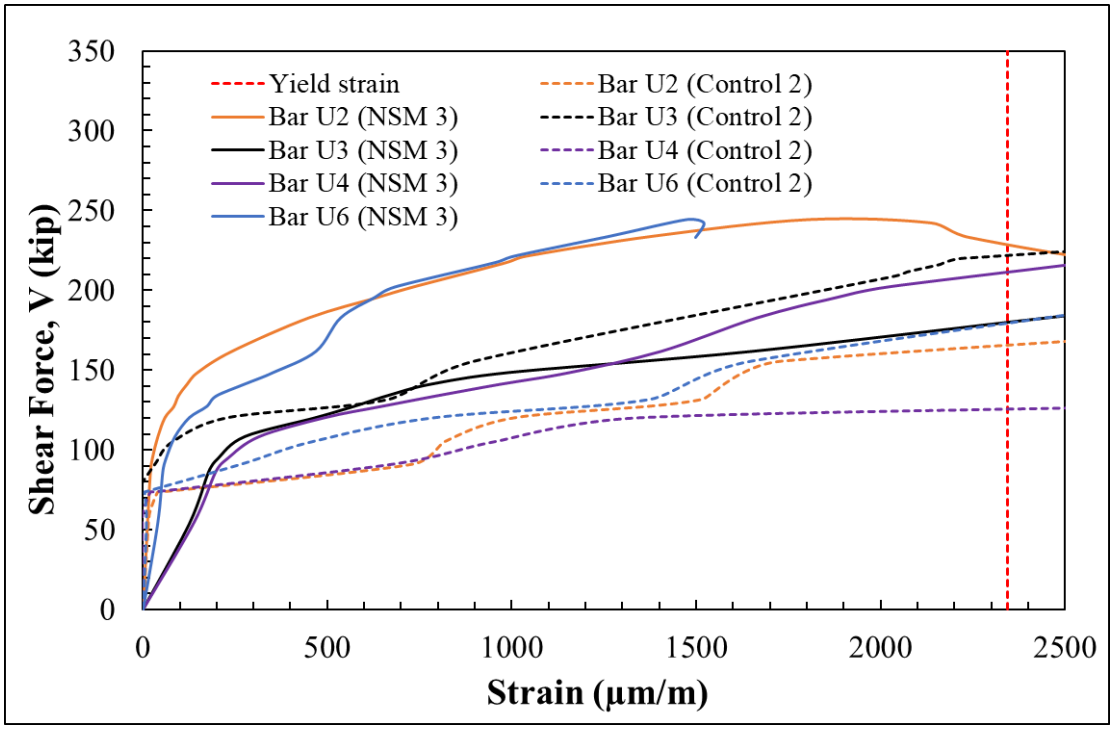

Figure 5-22: Strain vs. shear force plot for steel stirrups in test region

The FRP rods for the NSM 3 test were at a different spacing from the previous two tests, but the strain gauges were placed at similar distances from the supported end of the beam. As shown in Figure 5.23 below, the strains in the NSM rods remained significantly lower than NSM 2, because there were twice as many bars to achieve the same shear strength. It is worth noting again that this crack pattern was not symmetric, and the pictures shown above were for the side opposite to where the strain was recorded. None of the NSM bars achieved strains larger than 2000 με (12 percent of ultimate strain). The maximum strain recorded in any NSM rod was FRP 34 which experienced 1980 με which is 12 percent of the ultimate strain of the bar. There was evidence of debonding at the top face of the web, but a section of epoxy and concrete spalled off in this area which explains why it debonded at such a low strain.

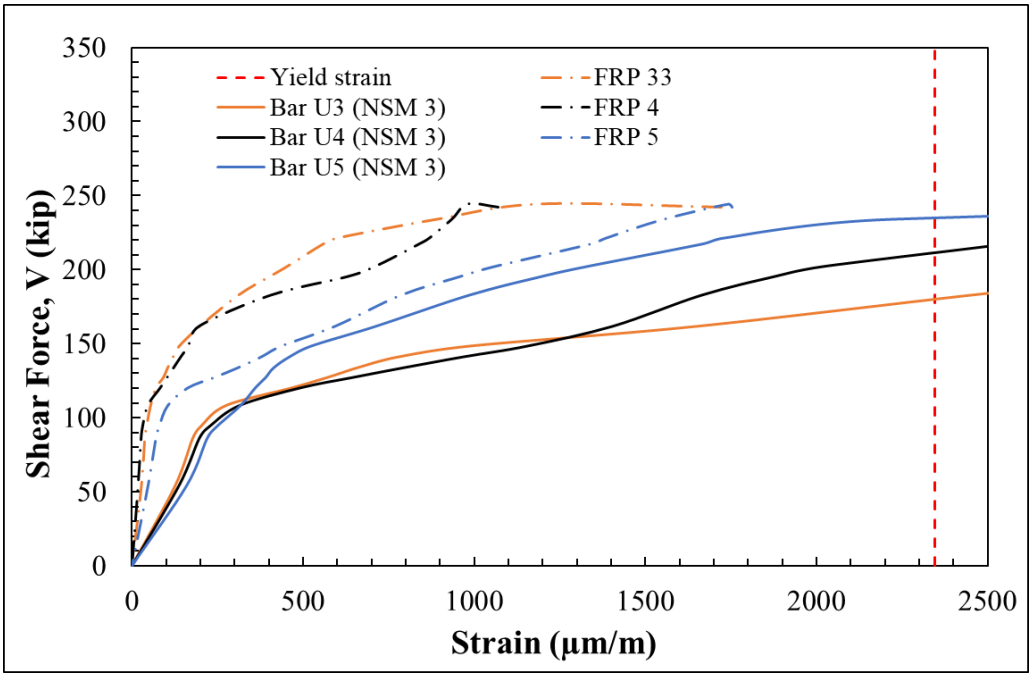

Figure 5-23: Strain vs. shear force plot for steel stirrups and NSM bars in test region

5.2.4 Failure of the NSM Schemes in Phase II: An Explanation

A close examination of Figs. 5-11 and 5-18 shows that, at failure, the dominant crack is local to the support and the NSM reinforcement and has found a path of least resistance and avoids the NSM bars with the result that the NSM reinforcement does not contribute to shear resistance. This can therefore be classified as a cover detachment failure.

First, from a review of the literature, Dias and Barros (2013) and Shomali et al. (2020) have observed that increasing the amount of transverse steel reinforcement in an NSM strengthened specimen will decrease the effectiveness of the NSM. In phase I we use Grade 40 #3 bars as the existing transverse reinforcement whereas in phase II, the transverse reinforcement consisted of Grade 60 #4 bars (an increase in the Vs contribution of over 100%). This validates the findings from the experiments conducted by Dias & Barros and Shomali et al. It is therefore likely, as suggested in the literature, that there may be a practical limit on using NSM. Tightly spaced NSM rods have been shown to have worse performance than fewer larger bars with the same reinforcement ratio. In the literature, because the beams are small, it is possible to get reasonable reinforcement ratios without using NSM spacings less than half the beam depth. For our test, our NSM bar spacing to beam depth ratio is much lower in order to achieve a similar reinforcement ratio.

Secondly, and more significantly, size effect may have played an important role. Most beams tested in the past using NSM have depths ranging from 8” – 16” and web widths varying from 6” – 10”. One series of tests had beams with dimensions of 8” width and 16” depth and another 24” deep beam had a tapered web with the bottom stem being only 4”. The tests carried out in this study were the first of a kind – where the girder depth was 30” and the web width was 14”. The web was wide enough to allow for the nonsymmetric 3D failure mechanism that developed. A thinner web might lean towards 2D behavior (meaning a symmetric response on both sides), where the NSM reinforcement would be more effective.

6.0 SHEAR STRENGTHENING METHOD II: PARTIALLY EMBEDDED BARS AS WEB REINFORCEMENT

In this next phase of testing, the second strengthening scheme was investigated wherein CFRP bars were partially embedded in the web of the girder. Two tests will be carried out to investigate the effect of existing stirrups on the shear enhancement. Results and relevant findings are reported in this chapter.

6.1 Specimen preparation

Installation of the PEB rods began two weeks after the concrete was poured. The main implementation steps of the PEB are shown in Figure 6-1 and can be summarized below:

(1) The locations of the strengthening PEB bars were marked on the girder's flange within the shear span of the strengthening specimen exactly at the girder's cross-section centerline. In this experimental program, the hole's locations were pre-marked on the formwork and copied into the concrete flange to ensure the precise location of the PEB bars between the existing shear reinforcement (stirrups). Of course, this is not ideal in the case of a real-world application. However, the as-built drawings and the help of a rebar detector could be utilized to verify the location of the existing longitudinal (flexural) and transverse (shear) reinforcement.

(2) Holes with a diameter of about 1.5 times the bar diameter ($1.5d_b$) were drilled vertically first with a wet core drilling machine using a diamond core drill bit up to approximately 14 inches to ensure the straightness of the drilled hole. Then a drilling machine with a hammer drill bit is used up to approximately 26 inches to avoid drilling through the flexural reinforcement (The main difference between ETS/DE method and the PEB technique), this drill bit provides a non-uniform (rougher) hole surface than the diamond core drill bit which is generally favorable to achieve substantially higher

characteristic bond stresses between the epoxy adhesive and the surrounding concrete. It is worth noting that in the later drilling process, the concrete dust was drawn out using a vacuum system simultaneously with the drilling process.

(3) As stated in the previous step, the cleaning process of the drilled holes takes place while drilling took place and continues after the drilling process is completed. Prior to the chemical adhesive deployment and bar installation, the drill hole was cleaned using a wire brush and compressed air and following the manufacturers' bonding material recommendations and procedures regarding preparing the drilled holes.

(4) The Hilti HIT-RE 500 V3 epoxy adhesive was deployed to fill two-thirds of the hole. Starting at the bottom of the hole and moving upward, with the selected chemical adhesive, manufacturer-specified mixing nozzle, and dispenser. The used quantity of epoxy adhesive ensured that there were no air voids at the bottom of the hole or surrounding the post-installed CFRP reinforcing bar.

(5) Afterward the selected reinforcing bar: the sand-coated and spirally-wound carbon FRP Carbon fiber reinforced polymer (CFRP) rod with a bar diameter (d_b) of 0.5 in. (#4) was inserted vertically into the hole using a twisting motion to ensure that the chemical adhesive coated the entire surface area. The appearance of the epoxy at the top of the hole suggested that the epoxy was equally distributed along the length of the holes and no air bubbles were trapped. Then excess epoxy adhesive was removed from the top surface of the hole and the epoxy was left to cure for 24 hours. Finally, the bar was cut, and the girder's flange surface was smoothed with a grinder.

After all the installation operations are completed, the strengthening section/specimen was left to cure for fourteen days at the laboratory environmental conditions before the testing of the girder is started.

Figure 6-1: PEM Strengthening Technique Preparations

6.2 Results of testing

6.2.1 Strengthening scheme I

As indicated previously, the first scheme consisted of using #4 CFRP bars spaced at 10 inches on center and placed midway between the existing stirrups. Results of the unstrengthened (control) specimen were reported in Chapter 3. Figure 6-2 compares the shear force-displacement curves of the unstrengthened and strengthened beams. It is seen that both specimens had similar linear shear force-deflection response up to a shear force of about 70 kip. Above this shear force level, the shear force-deflection curves become nonlinear due to the propagation of both flexural and shear cracks. The stiffness of both beams remained comparable up to a shear force of about 135 kip. Upon further loading, the strengthened (PEB Scheme I) specimen starts showing stiffer response than the unstrengthened (Control I) specimen indicating the effect of the presence of the PEB CFRP bars. Failure of the control specimen occurred at a shear load of 178 kip with a corresponding displacement of 0.46 inches at mid-span. However, the PEB Scheme I specimen at the same shear force showed a stiffer response with no degradation in stiffness. As the load increased, the strengthened specimen was able to resist higher shear force indicating the

effectiveness of the PEB CFRP bars in resisting the inclined shear cracks by utilizing the axial strength of the CFRP bars and consequently enhancing the concrete's contribution to the shear resistance. Upon further loading, a sudden drop in load took place at a peak shear force of 272 kip and a corresponding displacement of 0.84 inches at mid-span were recorded. The observed failure mode indicates a shear failure of the strengthened (PEB Scheme I) specimen similar to the unstrengthened control specimen. Comparing the collected results, the strengthened specimen with PEB method obviously demonstrated not only improvement in the shear force capacity with up to 53% increase, but also enhanced the deflection capacity with an increase of 83% over the mid-span deflection at failure in comparison with the control specimen. These enhancements are a testament to the feasibility of the PEB method as a retrofitting technique of RC bridge girders.

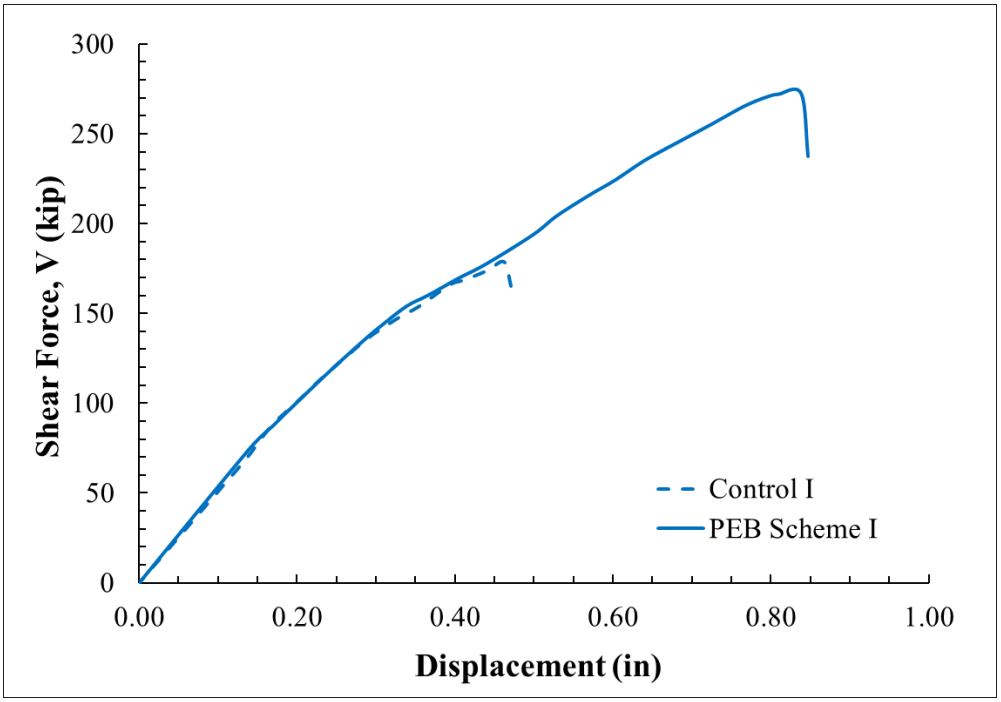

Figure 6-2: Shear force vs. displacement response of phase I specimens

Strains in the Flexural and Shear Reinforcements

Strains in the flexural and shear reinfrocements were monitored through the use of strain gauges bonded to selected longitudinal (flexural) and transverse (shear) reinforcements. The strain gauge

locations and labeling are identified in Fig. 3-19 (see Chapter 3). The relationships between the shear force in the specimen and the strains registered in longitudinal (flexural) and transverse (shear) reinforcements are shown in Figure 6-3 and Figure 6-4, respectively, for both the unstrengthened (Control I) and strengthened (PEB Scheme I) specimens. It is worth noting that to ensure a good bond between the PEB CFRP bars, epoxy material, and the surrounding concrete, a decision was made to not place strain gauges on the CFRP bars. Thus, no strain history is available for the strengthening bars.

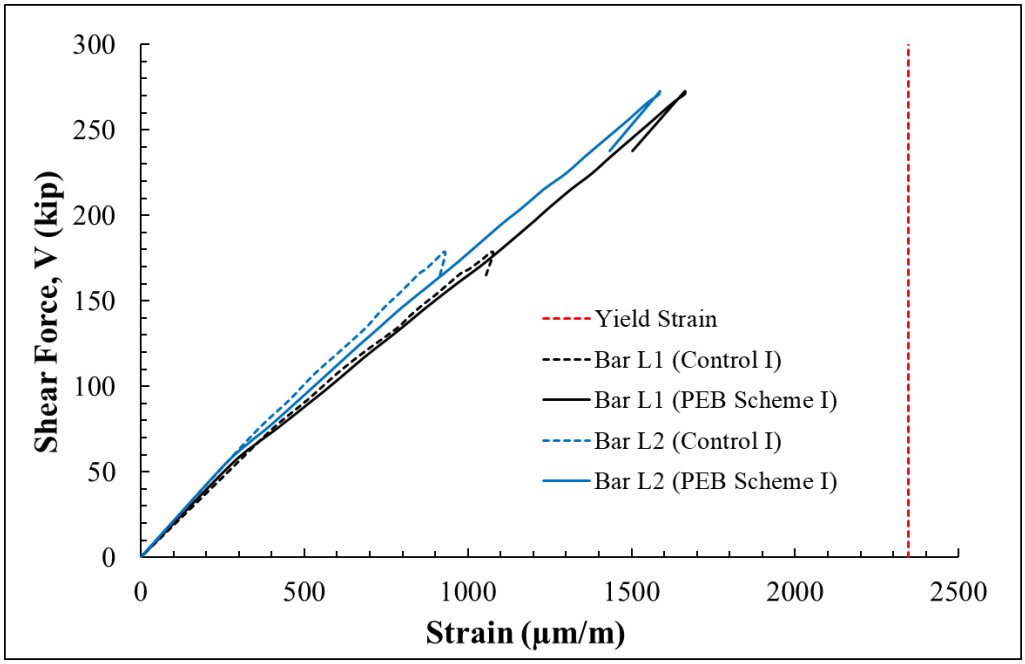

Figure 6-3: Shear force vs. strain in longitudinal reinforcement of phase I specimens

Strains recorded in the longitudinal reinforcement for both the unstrengthened (Control I) and strengthened (PEB Scheme I) specimens were well below the yielding strain which is about 2345 μm/m for Grade 60 steel reinforcing bars which confirms that both tested specimens failed in shear. For both specimens, the shear force-strain response was linear up to the peak (failure) load. Indeed, the strengthened specimen with PEB shear-strengthening technique exhibited higher shear load capcity and consequently much higher strain values were observed in the bars as shown in Figure 6-3.

Figure 6-4 depicts the evolution of strains in the shear stirrups as a function of the shear force for both the control I and PEB Scheme I specimens. The recorded strain values on the shear stirrups dependent on the distance between the location of the stirrups and the shear cracks. With either the unstregthened (Control I) or strengthened (PEB Scheme I) specimen, the relationship between the shear force and the recorded strain can be categorized into three phases. In the first phase, the recorded strains are very low and clearly the steel stirrups provided minial shear resistance. Upon further loading and the formation of the inclined shear cracks which crossed many of the stirrups, the recorded strain values increased rapidly indicating the activation of the steel stirrups and their contribution to the shear capacity of the tested RC member – this is represented by the ascending parts of the curves and marking the second phase. The third phase is marked by the yielding of the steel stittups. Many steel stirrups in both tested specimen yielded (recorded strains exceeded the yielding strain for Grade 40 steel reinfrocement which is about 1678 μm/m). However, the yielding of the steel stirrups of the PEB Scheme I specimen occurred at much higher magnitude (comparing the shear force at yielding of the stirrup designated as Bar U4 between the unstrengthened and strengthened specimens as shown in Fig. 6-4) which indicates that the presence of the PEB CFRP bars slowed the rate of strain development in the steel stirrups through controlling the development of shear cracks.

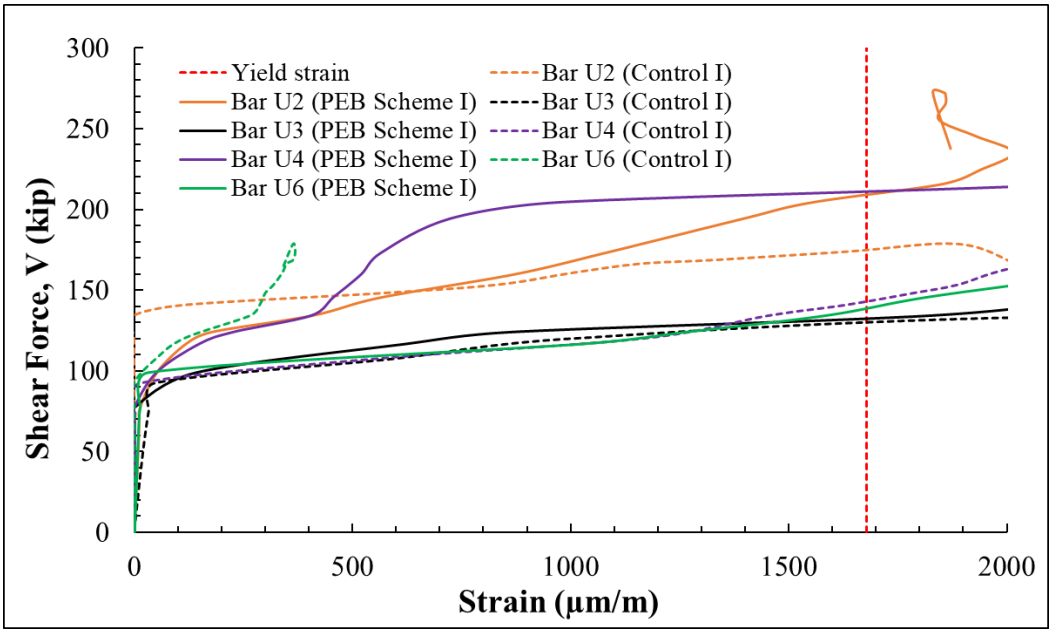

Figure 6-4: : Shear force vs. strain of transverse reinforcement of phase I specimens

Cracking Patterns and Failure Modes

The crack development and failure mode of the unstrengthened (Control I) specimen was reported in Chapter 3. The strengthened (PEB Scheme I) specimen failed in shear as well and was preceded by popping sounds suggesting debonding of some of the PEB CFRP bars, however, the main inclined shear crack had two branches in the girder's web, the outer (top) branch had an inclination of about 27° with respect to the girder's longitudinal axis whereas the inner (bottom) branch had an inclination of about 35°. Both branches merged at the support, however, they did not merge at the point of load application and only the bottom branch continued propagating further towards the flange and ended up at the point of load application, see Figure 6-5. The cracking development of the strengthened specimen appears to be in a similar manner to the unstrengthened (Control) specimen, however, the inclined web shear cracks were more widespread along the shear span region and developed at higher shear force levels compared to the control specimen. Figure 6-5 presents the crack progression of the PEB Scheme I specimen at different shear force levels with locations of the PEB CFRP bars identified.

Post-exanimation of the tested specimen indicated debonding at the CFRP bar/adhesive interface for some of the bars as shown in Figure 6-6. Only the bars where shear cracks crossed experienced slip at failure but the bars themselves were generally undamaged. Despite the lack of strain data for the CFRP bars, the bond between the bar and adhesive interfaces preformed well and was capable of mobilizing the strength of the CFRP bars up to a significant degree and this is obvious given the substantial increase in the shear capacity of the strengthened specimen comparing to the control. Similar to the control specimen, shear reinforcement yielded with no signs of the rupture in the steel stirrups.

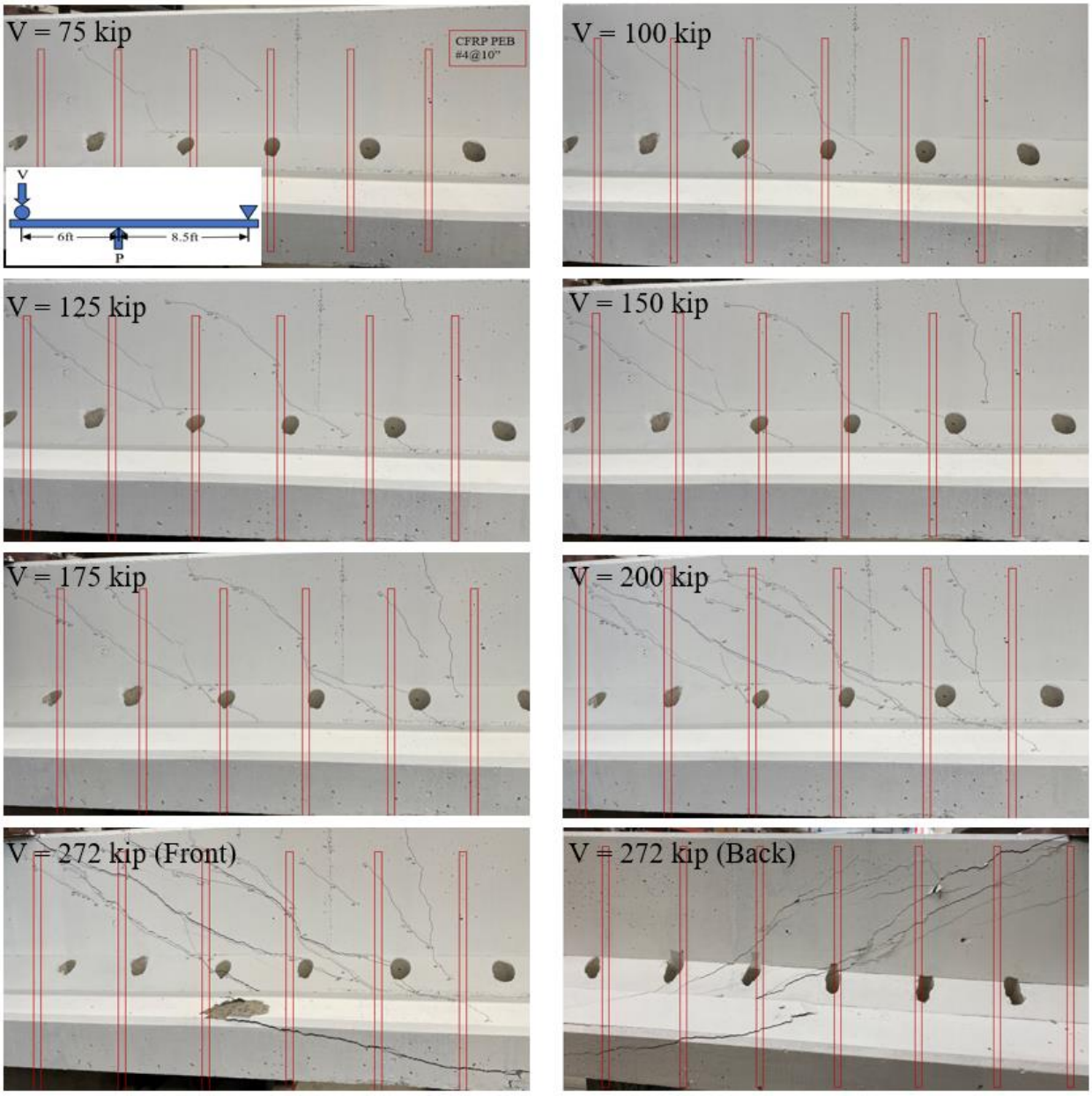

Figure 6-5: Crack development in PEB Scheme I specimen

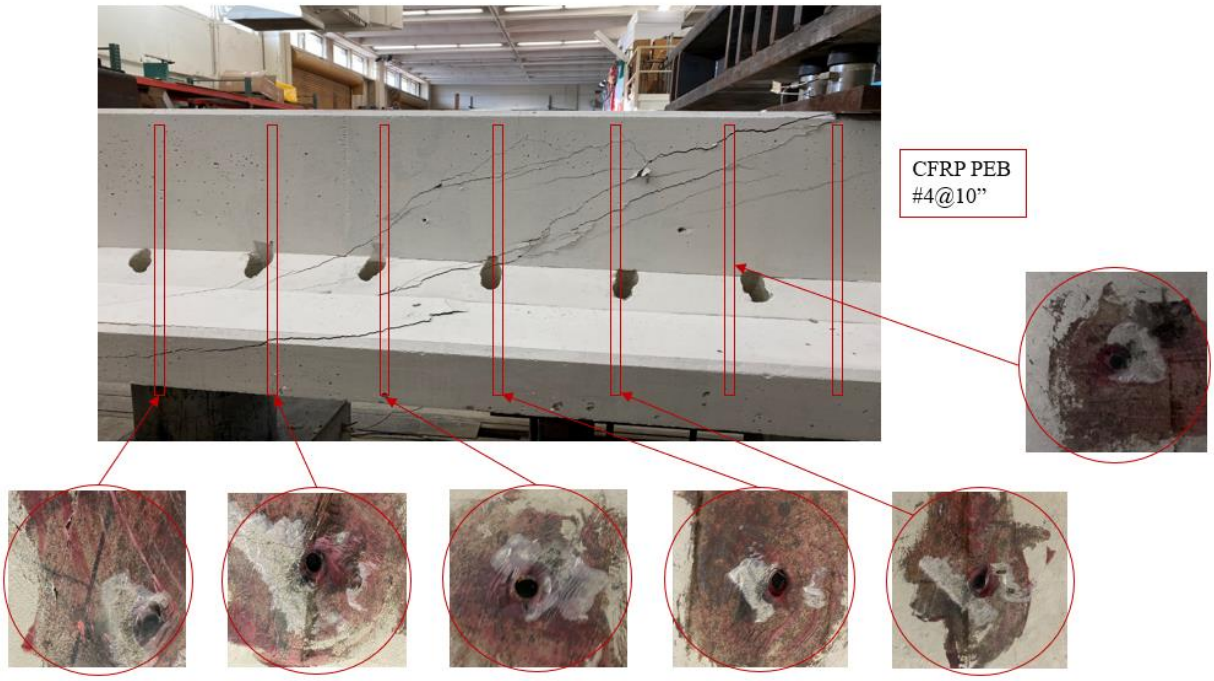

Figure 6-6: CFRP bars examined after testing in Specimen PEB Scheme I

6.2.2 Strengthening scheme II

In this phase, the geometry and testing configuration of the specimens were similar to the first phase. However, the shear reinforcement was increased by using #4 bars spaced center to center at 10 inches with Grade 60 steel reinforcement. Based on the literature review in Chapter 2, it appears that the interaction between the existing shear reinforcement and the embedded bars of the Embedded Through Section (ETS) or Deep Embedment (DE) technique and its effect on the overall performance of the shear strengthened girders is not well understood. Thus, it was deemed necessary to examine this effect on the performance of RC bridge girders strengthened with the PEB method. In addtion, it was in Caltran’s interest to evalaute the effectiveness of the proposed method using Grade 60 shear reinforcement (which is most commnly used) with bar diameter larger than #3 used in phase I. Thus, this phase aims to provide a better understanding of the interaction between the used embedded CFRP bars utilized in the PEB method and the existing transverse (shear) reinforcement by increasing the shear reinforcement ratio.

Shear Force-Deflection Response

Figure 6-7 compares the shear force-displacement curves of the control (unstrengthened) and strengthened specimens. Both specimens exhibit similar linear shear force-deflection response up to a shear force of about 60 kip. Above this magnitude, the response becomes nonlinear due to the propagation of both flexural and shear cracks. Unlike phase I, the specimens in this phase show divergence in stiffness from an early stage of loading with the strengthened (PEB Scheme II) specimen exhibiting a higher stiffness compared to the unstrengthened (Control II) specimen. The unstrengthened specimen failed at a shear force of about 239 kip and a corresponding displacement of 0.91 inches at mid-span. However, at the same shear force, the PEB Scheme II specimen showed a stiffer response with no degradation in stiffness. With increasing load, the strengthened specimen exhibited both higher shear force and displacement capacity indicating the effectiveness of the PEB CFRP bars in controlling the width of the inclined shear cracks. Finally, at a peak shear force of 310 kip and a corresponding displacement of 0.98 inches at mid-span a sudden drop in load took place with ensuing shear failure of the specimen. Comparing the observed results, the strengthened specimen with PEB method obviously demonstrated an improvement in the shear force capacity with up to 30% increase as well as an increase of 8% in the mid-span deflection at failure in comparison with the control specimen. Thus, the observed behavior herein confirms the feasibility of the PEB method as a shear strengthening technique though the increase in existing shear reinforcement resulted in an adverse effect with a net reduction in the percentage shear enhancement.

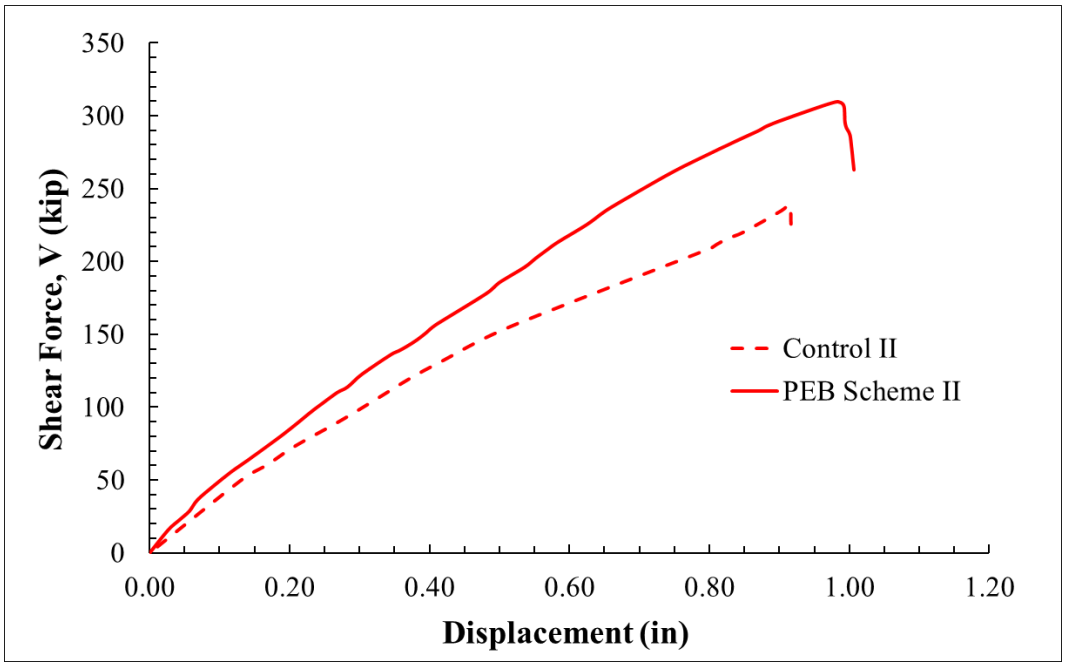

Figure 6-7: Shear force vs. displacement response of phase II specimens

Strains in the Flexural and Shear Reinforcements

Similarly to phase I specimens, the strains in the flexural and shear reinfrocements were monitored through the use of strain gauges. The strain gauge locations and labeling were identical to phase I specimens. The relationships between the shear force in the specimen and the strains registered in longitudinal (flexural) and transverse (shear) reinforcements are shown in Figure 6-8 and Figure 6-9, respectively, for both the the unstrengthened (Control II) and strengthened (PEB Scheme II) specimens. Again, no strian data was recorded for the PEB CFRP bars in the strengthened (PEB Scheme II) specimen. Similar to the specimens in phase I, strains recorded in the longitudinal reinforcement for both the unstrengthened (Control I) and strengthened (PEB Scheme I) specimens were below the yielding strain of Grade 60 steel reinforcing bars. However, higher strain values were recorded especially with the strengthened specimen in this phase resulting in the higher shear force capacities. For both tsted specimens, the shear force-strain response was essentially linear up to the peak (failure) load as evident in Figure 6-8.

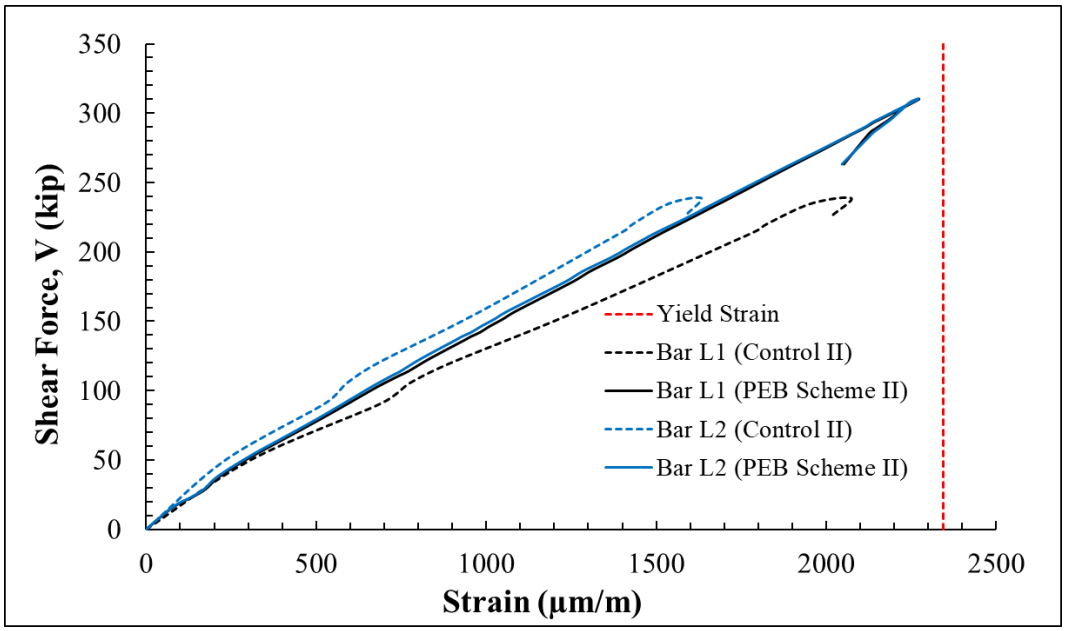

Figure 6-8: Shear force vs. strain in longitudinal reinforcement of phase II specimens

Figure 6-9 dispalys the evolution of strains in the strain gauges installed on the shear stirrups as a function of shear force for both the control II and PEB Scheme II specimens. The general relationship between the shear force and the recorded strain in the steel stirrups can be categorized as similar to the response of the tested specimens in phase I. All steel stirrups within the shear span in both tested specimens yielded (recorded strains exceeded the yielding strain for Grade 60 steel reinfrocement which is about 2345 µm/m). It is evident that yielding of the steel stirrups of the PEB Scheme II specimen occurred at much higher magnitude (comparing the shear force at yielding of the stirrups designated as Bar U2, Bar U5, and Bar U6 between the unstrengthened and strengthened specimens) indicating once again that the presence of the PEB CFRP bars reduced the rate of strain development in the steel stirrups through controlling the rate of increase in the shear crack widths.

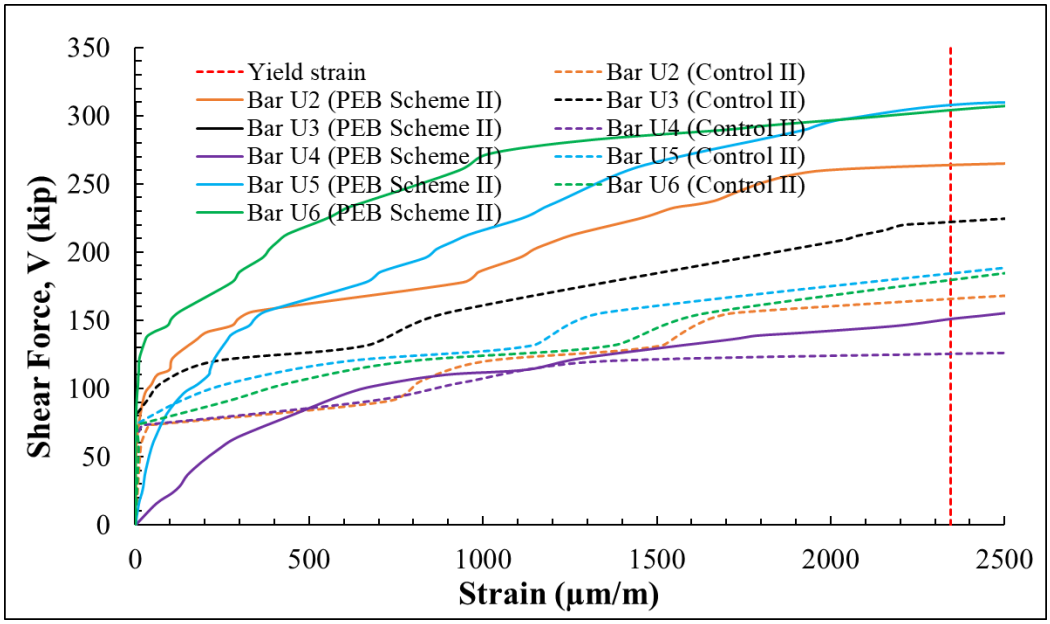

Figure 6-9: Shear force vs. strain in transverse reinforcement of phase II specimens

Cracking Patterns and Failure Modes

The crack patterns in the unstrengthened (Control II) specimen were previously presented in Chapter 3. Figure 6-10 displays the crack development in Control II specimen at different shear force levels. As in the case of the Control I specimen, hairline flexural cracks developed in the web at the point of load application and in the shear span regions during the early stages of load application. Next, inclined web shear cracks at mid-height of the web started to spread in the shear span region as the applied load was increased. Upon further loading, the inclined web shear cracks started to extend towards the support and point of load application. With further increase in load, the inclined shear cracks become more distinct and widened until failure. Strain guage data indicated that the steel stirrups yielded but none of them ruptured.

The strengthened (PEB Scheme II) specimen failed in shear and was preceded by popping sounds suggesting debonding of some of the PEB CFRP bars in a manner similar to PEB Scheme I specimen. Despite the widespread web shear cracks within the shear span region, a major inclined shear crack shear with an angle of approximately 45° can be seen distinctly in Figure 6-10.

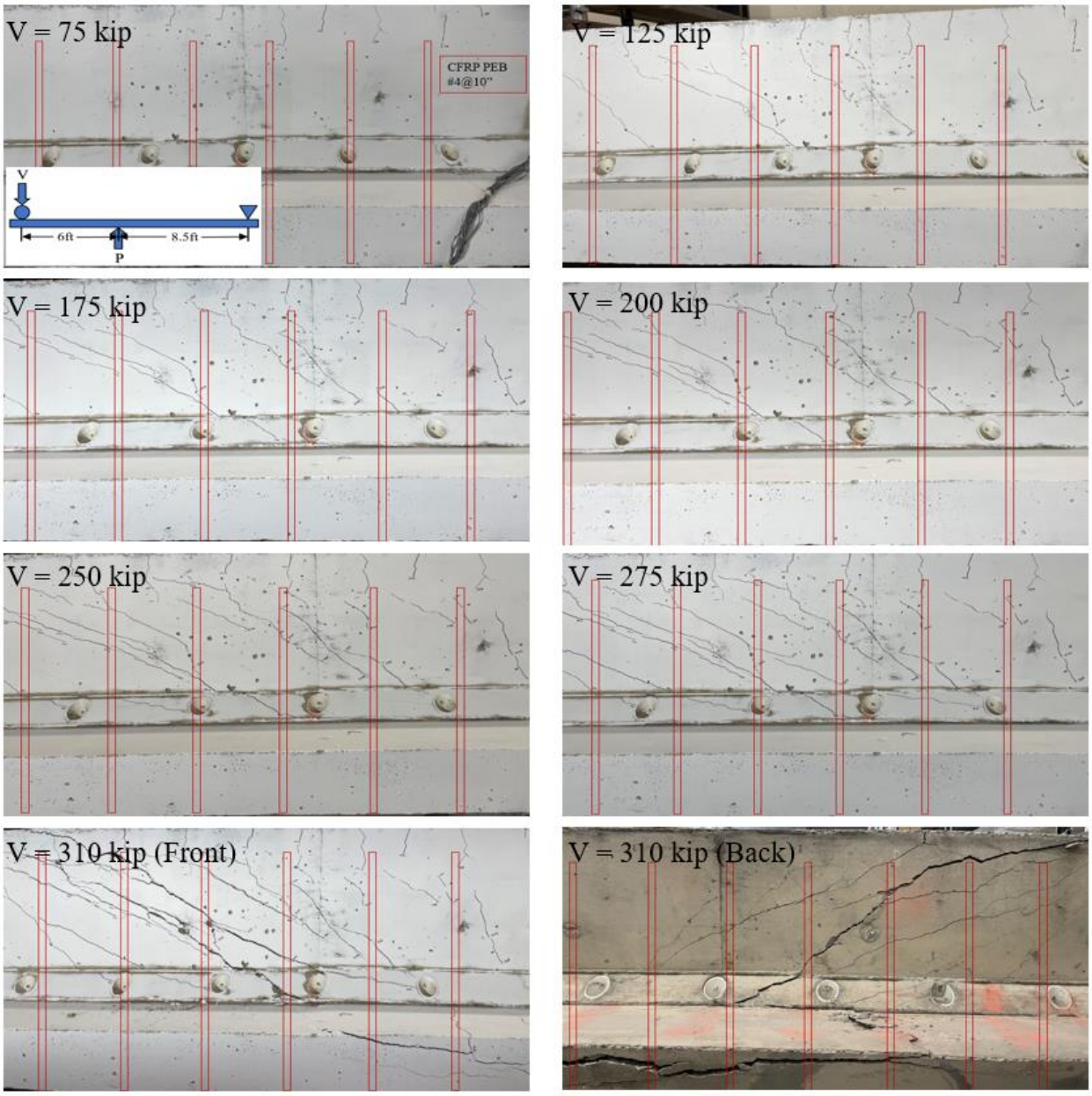

Figure 6-10: Crack development in the PEB Scheme II specimen

The crack growth of the strengthened specimen was comparable to the unstrengthened (Control II) specimen, however, the inclined web shear cracks were more widespread along the shear span region and developed at higher shear force levels compared to the control specimen. But unlike the unstrengthened (Control II) specimen, shear cracks extended to the girder's flange and a major almost horizontal crack can be seen in Fig. 6-11. Post-exanimation of the tested specimen revealed the debonding at the CFRP bar/adhesive interface in three of the CFRP bars (where inclined shear

cracks passed through) as shown in Figure 6-11. In general, there was adequate bond between the bar and adhesive interfaces during loading leading to the increase in the shear capacity of the strengthened specimen.

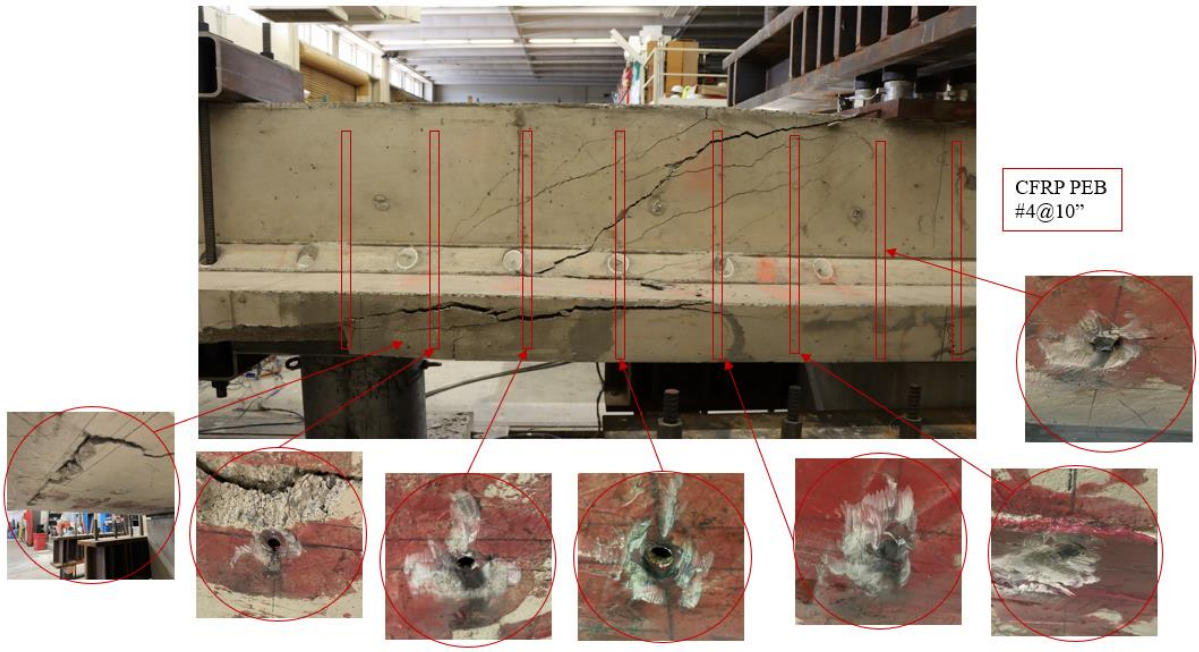

Figure 6-11: CFRP bars in Specimen PEB Scheme II examined after testing

7.0 RECOMMENDATIONS & CONCLUSION

The feasibility and effectiveness of two shear-strengthening techniques in enhancing the shear capacity of existing reinforced concrete girder bridges was investigated in this study. The first scheme consisted of using Near-Surface-Mounted (NSM) bars while the second scheme comprised Partially Embedded Bars (PEB) in the web of the girder. The NSM-based approach is an existing method that has been studied by other researchers though some unresolved issues remain and the present testing was expected to contribute to the existing literature on NSM strengthening. In contrast, PEB is a variation of an existing method referred to as Embedded Through Section (ETS) where the bar is embedded through the full depth of the section. In the proposed PEB method, shear strengthening is achieved by inserting steel or FRP bars into holes bored through the partial depth of the girder web and then bonded with an epoxy adhesive. A testing program was undertaken to assess the effectiveness of each strengthening method. In all, two control tests and five tests of strengthened sections were conducted. Details of the experimentally observed results were presented in Chapters 5 and 6. Relevant findings from the testing are reported in this chapter.

7.1 Summary of Research Tasks

The research objectives were accomplished through the following tasks:

(a) A prototype bridge was first identified following a review of the Caltrans bridge inventory. The selection was based on the ability of the UC Davis strong floor and reaction system to test a specimen whose cross-section represents either a full-scale or near full-scale bridge girder. Reinforcing details of the specimen were modified so as to induce shear failure prior to flexural yielding of the specimen.

(b) A preliminary series of pull-out tests were carried out to establish the most suitable anchorage scheme (for NSM) and bar material and bonding agent for PEB..

(c) The experimental testing was conducted in different phases: two control tests were conducted on unstrengthened specimens cast with different batches of concrete; the next phase consisted of three tests using NSM CFRP bars; and the final phase involved strengthening of the specimens using PEB.

7.2 Primary Research Findings

The utilized test configuration, with the use of a clamping system and the design of the RC bridge girder to produce two test specimens, was successful and effective as no shear cracks were observed and very low strain values were recorded on the shear stirrups in the untested region of the specimens. With the exception of the NSM specimens, all other specimens failed in a shear cracking mode, accompanied by a loss of continuity of the load path between the loading device and one of the supports. In other words, the shear cracks associated with failure ran from one of the supports, through the web and compression flange, to the edge of the plate used to distribute the applied load. Due to crack propagation through the compression flange and the concomitant disruption of the load path, crushing of the concrete in the compression struts could not develop. Crack openings were sizable such that the benefits of aggregate interlocking were lost to some degree. However, the maximum crack width was less than half of the nominal maximum aggregate size, hence there was likely no complete loss of aggregate interlock.

The primary findings from the experimental studies are grouped into two categories. The first set of conclusions are based on the NSM tests and summarized below:

1. The NSM shear strength contribution varied widely between the phase I and phase II results ranging from 5 kips - 45 kips (2% - 25% increases compared to the respective control tests). The phase I results showed the only meaningful improvement in the shear strength while the phase II results were ineffective in increasing the shear strength of the specimen.
2. Stirrups adjacent to the major shear cracks yielded in all tests, meaning the NSM rods do not negatively impact the performance of stirrups, which is in line with previous test results.
3. The primary failure mode of all 3 NSM tests was side cover detachment. This was marked by the crack angle following a steeper path to pass vertically between NSM bars and then wrapping behind them at the top face of the web.
4. Though f_c' is a main parameter in determining the bond strength of NSM reinforcement, the difference in f_c' between test phases cannot fully account for the difference in the NSM shear contribution between phase I and phase II. It is therefore likely that there is an inverse relationship between the amount of existing transverse reinforcement and the shear contribution of the NSM reinforcement. Doubling the amount of NSM reinforcement used in phase two was not effective at increasing the NSM shear contribution. In fact, the

literature suggests there may be a practical limit on using NSM. Tightly spaced NSM rods have been shown to have worse performance than fewer larger diameter bars with the same reinforcement ratio. In previous tests, because the beam cross-sections were small, it is possible to get reasonable reinforcement ratios without using NSM spacings less than half the beam depth. In the current research, the NSM bar spacing to beam depth ratio is much lower in order to achieve a similar reinforcement ratio. This is because manufacturers don't make NSM rods larger than 1/2" diameter but using larger diameter bars may not be feasible given the available cover. Given the limit on bar diameter, the only option to increase the reinforcement ratio was to decrease the spacing, which probably resulted in an ineffective strengthening scheme.

5. Finally, it is hypothesized that "size effect" played an important role. In the past, most beams tested using NSM have depths ranging from 8" – 16" and web widths varying from 6" – 10". One series of tests had beams 24" deep beam but had a tapered web with the bottom stem being only 4". The tests conducted in this study were the first of a kind – where the girder depth was 30" and the web width was 14". The web of the tested girders was wide enough to allow for the strongly 3D failure mechanism that developed. A thinner web might lean toward 2D behavior (meaning a symmetric response on both sides), where the NSM reinforcement would be more effective.

The next set of research findings are based on the PEB testing:

1. Results from the pull-out testing demonstrated that, regardless of the bonding material, sand-coated CFRP bars provided the highest pull-out force capacity compared to other tested bars. Smooth CFRP bars had the least resistance to the applied pull-out force due to premature bar-slip. Traditional Grade 60 bars and high-strength steel (Grade 80) bars failed by yielding and rupture of the bars, respectively. Finally, all of bonding materials – either the adhesives (epoxy) or cementitious material (grout) – exhibited good performance regardless of the embedded bar material.
2. The proposed shear-strengthening technique using Partially Embedded Bars (PEB) is an effective shear-strengthening method. An increase in shear strength of 53% and 30% compared to the unstrengthened (control) specimens was obtained for PEB Scheme I and II, respectively.

3. Results from the load test on PEB Scheme II specimen highlighted the fact that the existing shear reinforcement ratio (ρ_s) has a significant influence on the effectiveness of PEB. Doubling the ρ_s in the PEB Scheme II specimen resulted in a reduction in shear strength of approximately 23%.
4. In both Phase I and II specimens, the presence of PEB CFRP strengthening bars resulted in more distributed cracking confirming that the embedded bars helped control the opening of shear cracks and led to a larger section of the shear span participating in resisting the applied shear force.

In summary, the PEB method is significantly more effective than the NSM method at increasing the shear capacity of reinforced concrete T-beams, as summarized in Table 6-1.

Table 7-1: Summary of shear gain for both methods

Label	V_u (kips)	V_{frp} (kips)	$\frac{V_{u\_strengthened}}{V_{u\_control}}$
C1	178	-	-
C2	239	-	-
PEB 1	272	94	1.53
PEB 2	310	71	1.30
NSM 1	223	45	1.25
NSM 2	248	9	1.04
NSM 3	244	5	1.02

7.3 Design Guidelines for Shear Strengthening

Two approaches for shear strengthening of existing RC girders were evaluated. Of the two methods considered, strengthening using NSM was inconclusive, hence no effort was made to develop an expression for the shear enhancement using NSM. It is worth mentioning that efforts to understand the NSM shear strengthening began over two decades ago, but its integration into the design standards and codes has been lagging. Early analytical formulations for NSM FRP did not include multiple failure modes, instead focused primarily on debonding. As research progressed, concrete

cover detachment as a potential limit state has been incorporated in more models, leading to improved accuracy in prediction. Three models were assessed in this study:

(1) The model proposed by Kotynia (2007) which is based on the strut-and-tie concrete model and does not consider the side cover detachment failure mode.
(2) The model by Mofidi et al. (2023) which is also based on the strut-and-tie concrete model but accounts for both debonding and side cover detachment by considering the effective strain for each failure mode separately and selecting the critical failure mode.
(3) The model by Baghi and Barros (2017) which is based on a combination of the simplified modified compression field theory (SMCFT) and a NSM shear strength model initially introduced by Bianco et al. (2014).

The predictions using the above three analytical models are compared with the tests results in Table 7-1. All three models provide somewhat conservative (R > 1.0) or very conservative (R > 1.5) predictions for specimen NSM 1. However, all three models fail to provide meaningful predictions for the other two specimens.

Table 7-2. Comparison between analytical predictions and test results

Specimen	V_{fexp} (kip)	V_{fKot} (kip)	R	V_{fMof} (kip)	R	V_{fBah} (kip)	R
NSM 1	45	26.76	1.68	27	1.67	36.6	1.23
NSM 2	9	26.76	0.34	24.9	0.36	28.6	0.31
NSM 3	5	53.53	0.09	37.9	0.13	45.4	0.11

V_{fKot} = Kotynia 2007, V_{fMof} = Mofidi et al. 2023, V_{fBah} = Baghi and Barros (2017)
$R = V_{exp}/V_{model}$

7.3.1 Shear Enhancement with Partially Embedded Bars

Of the two methods investigated for shear strengthening, the use of Partially Embedded Bars (PEB) was found to be effective. Consequently, a simplified expression is proposed to determine the added shear gained from the PEB. The total shear strength V_f is given by:

$$V_f = V_{control} + V_{PEB} \quad (7\text{-}1)$$

In the above expression, $V_{control}$ is the combined shear contribution from plain concrete and the transverse reinforcement and both terms can be estimated using current AASHTO specifications. In the present study, this quantity is directly available from the control tests. The additional term V_{PEB} is the contribution from the partially embedded CFRP bars. Since only two tests were carried out with varying shear reinforcement, an additional data point was generated from a finite element simulation (see FE model description in Chapter 4) assuming #5 stirrups at a spacing of 10 inches. The additional shear is due to the contribution of the partially embedded bars, as summarized in Table 7-3.

Table 7-3. Estimation of shear contribution from PEB

	Scheme I	**Scheme II**
$V_{control}$, from Control tests	178.0 k	239.0 k
V_f of strengthened specimens	272.0 k	310.0 k
Contribution from PEB, V_{PEB}	94.0 k	71.0 k
A_v / A_{PEB}	1.1	2.0
V_{PEB} / V_s	2.14	1.15

V_s in Table 7-3 is computed using the following AASHTO expression:

$$V_s = A_v f_y d_v \cot(\theta) / s \quad (7.2)$$

In the above expression, V_s is the shear contribution of the transverse steel reinforcement, A_v is the area of the shear stirrups, d_v is the effective shear depth as defined in AASHTO, s is the spacing of the transverse reinforcement, and θ is the angle of inclination of the diagonal compression strut and is a function of the shear and moment in the critical section. For both specimens, $\theta = 32°$ at the failure load.

It is observed that increasing the transverse reinforcement decreases the effectiveness of the PEB. This can be attributed to the fact that delaying the yielding of the stirrups does limits the strain buildup in the partially embedded CFRP bars and reduces their contribution to shear

resistance. The variation in the shear resistance provided by PEB (normalized by the shear contribution of steel) is plotted as a function of the reinforcement ratio (area of stirrups to area of PEB) in Figure 7-1. The third data point is extracted from one of the FE simulations discussed in Chapter 4 and corresponds to Grade 60 #5 stirrups spaced at 10 inches.

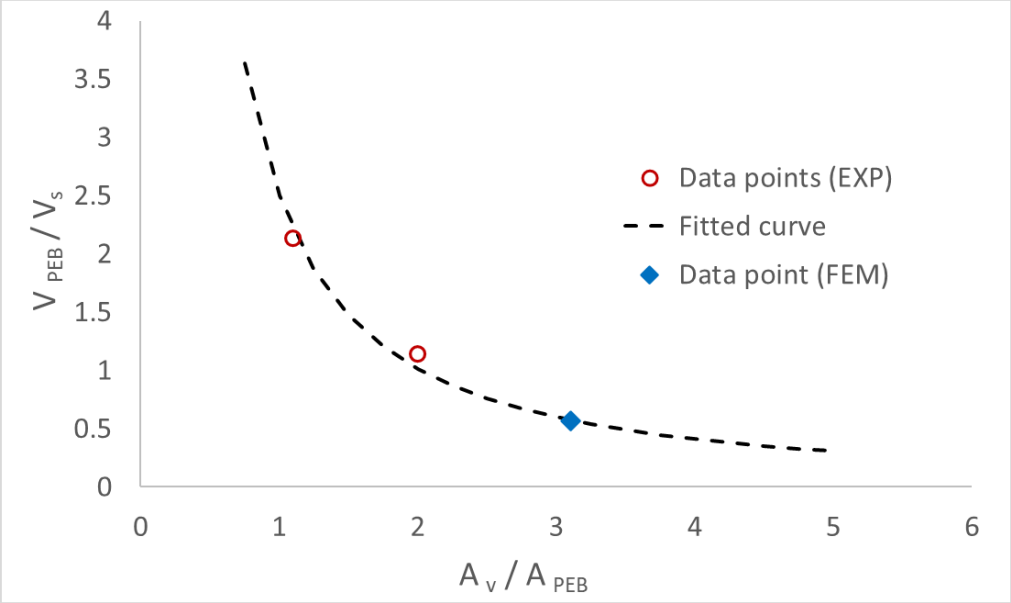

Figure 7-1: Shear contribution from PEB as a function of existing transverse reinforcement

The following expression was derived for the fitted curve:

$$V_{PEB} = 2.5\, V_s \cdot \left(\frac{A_v}{A_{PEB}}\right)^{-1.3} \tag{7-3}$$

The shear resistance provided by the partially embedded bars, V_{PEB} can be estimated using Equation (7-3).

7.4 Future Work

In the present study, strengthening using NSM was limited to three tests. The specimen dimensions, reinforcement details, and boundary conditions were chosen to represent the conditions of an existing simply supported T girder. Though useful information was generated from the testing,

there remains a need for future work to further our understanding of the behavior of T-girders strengthened with NSM reinforcement.

1. The two specimens in phase II experienced premature side cover detachment failure. This is attributed to "size effect". The size of specimens in this study was significantly larger than those tested in prior research. Additional large-scale testing is needed to confirm this finding.
2. The effectiveness of NSM appears to have diminishing returns as the ratio of existing transverse reinforcement to NSM reinforcement increases. To verify this observation and gain more insight into this phenomenon, further testing complemented by numerical simulations is needed.

In the case of PEB, the conducted experimental campaign was limited to two large-scale specimens. The experimental data gathered during testing provided ample useful information that confirmed the success of the PEB method. Yet, the generated data is still somewhat limited and not adequate to draw general conclusions regarding the proposed method. The following additional tasks are proposed to gain a more comprehensive understanding of the PEB technique:

1. Additional large-scale testing that extends the range of the investigation: tests where the ratio of the strengthening embedded bars is varied for a fixed ratio of the existing shear reinforcement and ratio of the existing shear stirrups is varied for a fixed ratio of the embedded bars.
2. Additional large-scale testing that investigates other critical parameters such as the influence of the embedded bar diameter and material; the position of the embedded bars relative to the locations of existing shear reinforcement; the inclination of the embedded bars; and using more than one PEB bar per cross-section of the girder.
3. The present study was limited to girders with a T cross-section. Hence, there is a need to test additional configurations including other cross-sections (e.g. box girder), varying shear spans and varying support conditions.

Finally, it is proposed that the finite element models developed as part of this study be utilized in a wider parametric study following additional experiments to aid in the improvement of the expression proposed in Equation (7-1) to predict the shear enhancement due to PEB.

8.0 REFERENCES

AASHTO. (2017). AASHTO LRFD Bridge Design Specifications, 8th Edition, American Association of State Highway and Transportation Officials, Washington DC.

ACI 318-19 (2019), Building Code Requirements for Structural Concrete, American Concrete Institute, Farmington Hills, MI.

ACI 355.4 (2019), Qualification of Post-Installed Adhesive Anchors in Concrete, American Concrete Institute, Farmington Hills, MI.

ACI 440.1R-15 (2015), Guide for the Design and Construction of Structural Concrete Reinforced with Fiber-Reinforced Polymer (FRP) Bars, American Concrete Institute, Farmington Hills, MI.

Al-Tarafany, D. (2016). "Analysis of the Shear Behavior of Prestressed Concrete Spliced Girders." Ph.D. Dissertation, University of Texas at Austin, TX.

Alwash, D., R. Kalfat, R. Al-Mahaidi, and H. Du. 2021. "Shear strengthening of RC beams using NSM CFRP bonded using cement-based adhesive." Construction and Building Materials, 301: 124365. https://doi.org/10.1016/j.conbuildmat.2021.124365.

ASTM. (2021). "Compressive Strength of Cylindrical Concrete Specimens." ASTM C39 / C39M – 21, West Conshohocken, PA, 2021.

ASTM. (2021). "Standard Test Method for Tensile Properties of Fiber Reinforced Polymer Matrix Composite Bars." ASTM D7205 / D7205M-21, West Conshohocken, PA, 2021.

ASTM. (2022). "Standard Test Methods and Definitions for Mechanical Testing of Steel Products." ASTM A370 – 22, West Conshohocken, PA, 2022.

Baghi, H., and J. A. O. Barros. 2016. New Approach to Predict Shear Capacity of Reinforced Concrete Beams Strengthened with Near-Surface-Mounted Technique. *ACI Structural Journal*, 114(1). https://doi.org/10.14359/51689433.

Barros, J. A. O., and G. M. Dalfré. 2013. "Assessment of the effectiveness of the embedded through-section technique for the shear strengthening of reinforced concrete beams: Effectiveness of the ETS technique." Strain 49 (1): 75–93. https://doi.org/10.1111/str.12016.

Belarbi, A., S.-W. Bae, and A. Brancaccio. 2012. "Behavior of full-scale RC T-beams strengthened in shear with externally bonded FRP sheets." Construction and Building

Materials, Strengthening and Retrofitting of concrete structures with Fiber Reinforced polymer material, 32: 27–40. https://doi.org/10.1016/j.conbuildmat.2010.11.102.

Bianco, V., G. Monti, and J. A. O. Barros. 2014. Design formula to evaluate the NSM FRP strips shear strength contribution to a RC beam. *Composites Part B: Engineering*, 56: 960–971. https://doi.org/10.1016/j.compositesb.2013.09.001.

Breveglieri, M., J. A. O. Barros, A. Aprile, and A. Ventura-Gouveia. 2016. "Strategies for numerical modeling the behavior of RC beams strengthened in shear using the ETS technique." Engineering Structures, 128: 296–315. https://doi.org/10.1016/j.engstruct.2016.09.027.

Brindley, M. 2017. "Shear assessment and strengthening of reinforced concrete T-beams with externally bonded CFRP sheets." Ph.D. thesis, Dept. of Architecture and Civil Engineering, Univ. of Bath.

Caltrans (2018), Standard Specifications, California Department of Transportation, Sacramento, CA.

Cervenka, V., Jendele, L., & Cervenka, J. 2021. "ATENA Program Documentation", Cervenka Consulting, Prague.

Dias, S. J. E., and J. A. O. Barros. 2013. "Shear strengthening of RC beams with NSM CFRP laminates: Experimental research and analytical formulation." Composite Structures, 99: 477–490. https://doi.org/10.1016/j.compstruct.2012.09.026.

Godat, A., O. Chaallal, and K. W. Neale. 2013. "Nonlinear finite element models for the embedded through-section FRP shear-strengthening method." *Computers & Structures*, 119: 12–22. https://doi.org/10.1016/j.compstruc.2012.12.016.

Grayson-Wallace, B., Aljasar, A., Cheng, L., Bolander, J. and Kunnath, S.K. (2022). "Advances in Shear Strengthening of Concrete Bridge Girders." *ASCE Journal of Bridge Engineering*, 27 (6). https://ascelibrary.org/doi/full/10.1061/(ASCE)BE.1943-5592.0001880.

Kalfat, R., R. Jumaah, R. Al-Mahaidi, K. Abdouka, and J. Hashemi. 2020. "Post-Tensioned Concrete Beams Strengthened in Shear Using Fiber-Reinforced Polymer Laminates and Patch Anchors." J. Compos. Constr., 24 (2): 04019065. https://doi.org/10.1061/(ASCE)CC.1943-5614.0000989.

Kim, Y., Quinn, K., Garcia, J., Sun, W., Ghannoum, W., and Jirsa, J. 2012. "Shear strengthening of reinforced and prestressed concrete beams using carbon fiber reinforced polymer

(CFRP) sheets and anchors." Technical Rep. 0-6306-1, Center for Transportation Research, Univ. of Texas, Austin, TX, 326.

Kotynia, R. (2007). Efficiency of RC T-Section Beams Shear Strengthening with NSM FRP Reinforcement. In: Ye, Feng and Yue (eds) *Advances in FRP Composites in Civil Engineering*. Springer, Berlin, Heidelberg. https://doi.org/10.1007/978-3-642-17487-2_171.

Lee, D., & Cheng, L. (2013). Bond of NSM systems in concrete strengthening – Examining design issues of strength, groove detailing and bond-dependent coefficient. *Construction and Building Materials*, *47*, 1512–1522. https://doi.org/10.1016/j.conbuildmat.2013.06.069

Mofidi, A., L. Cheng, O. Chaallal, M. Rajabifard, and Y. Shao. 2023. Code-Formatted Theoretical Design Equations for Shear Strengthening of RC Beams Using Near-Surface Mounted FRP Reinforcement. Zenodo. https://doi.org/10.5281/ZENODO.8133277.

Phillips, D.V. & Zhang, B. 1993." Direct tension tests on notched and un-notched plain concrete specimens." Magazine of Concrete Research, 45(162), 25-35.

Shomali, A., D. Mostofinejad, and M. R. Esfahani. 2020. "Effective strain of CFRP in RC beams strengthened in shear with NSM reinforcements." Structures, 23: 635–645. https://doi.org/10.1016/j.istruc.2019.10.020.

Tambusay, A., and P. Suprobo. 2019. "Prediction the flexural response of a reinforced concrete beam using the fracture-plastic model." Journal of Civil Engineering, 34 (2): 61. https://doi.org/10.12962/j20861206.v34i2.6470.

Tambusay, A., P. Suprobo, B. Suryanto, and W. Don. 2021. "Application of Nonlinear Finite Element Analysis on Shear-Critical Reinforced Concrete Beams." *J. Eng. Technol. Sci.*, 53 (4): 210408. https://doi.org/10.5614/j.eng.technol.sci.2021.53.4.8.

Vásquez, V. A. 2019. "Detailed Finite Element of a Type II Bridge Column Shaft Reinforced with High-Strength Steel." PhD Dissertation, UC San Diego. ProQuest ID: VxE1squez_ucsd_0033M_18105. Merritt ID: ark:/13030/m5r83d02.

Vecchio, F.J., and Collins, M.P. 1986 "The Modified Compression-Field Theory for Reinforced Concrete Elements Subjected to Shear." ACI Journal, Vol. 83, No. 2, pp. 219-231.

Wang, X., and L. Cheng. 2021. "Bond characteristics and modeling of near-surface mounted CFRP in concrete." *Composite Structures*, 255: 113011. https://doi.org/10.1016/j.compstruct.2020.113011.

APPENDIX

Additional Details on the Finite Element Modeling

The details presented in Chapter 4 of this report summarized the main features of the finite element (FE) model and compared numerical simulations to observed experimental results. In this Appendix, additional details of the modeling scheme are provided. After the Phase 1 test was completed and the FE simulations were compared to the experimental results, it was noted that the initial stiffnesses of the models were substantially stiffer than the physical test. A large portion of this difference was attributed to deformations in the reaction frame, the nature of the supports and the loading process (see Fig. 3.8). Since the beam was loaded against gravity, the loading jack had to first pick up the beam (i.e., carry the self-weight of the beam) and then the four tie rods at each end of the beam were fully engaged. Moreover, the supports are not a point or line on the beam, rather it is a finite region since the load is transferred through plates to the reaction beams. In order to capture this in the model, the zero-displacement Y restraints were replaced with linear-elastic springs with stiffnesses equivalent to the area of the steel tie rods as shown in Figure A.1.

Figure A.2 shows a comparison of the initial stiffness of the physical experiment and two FE models, one with springs and one with zero vertical displacement boundary conditions. Note that the “FEM no springs” model was not run to failure since the goal was to match the initial stiffness, so a complete force-deformation curve was not generated. The stiffness of the springs was tuned to match the initial stiffness in the experimental results. The model with vertical spring supports were adopted for all models presented in Chapter 4.

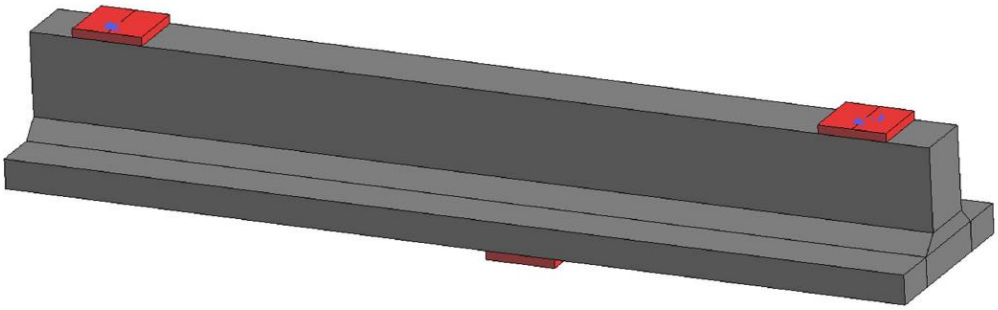

a) Zero displacement line B.C.'s

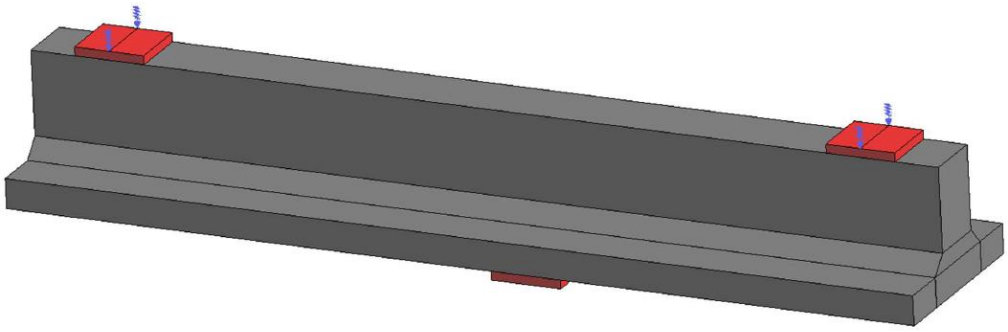

b) Spring supports for vertical reaction frames.

Figure A-1: Modeling of the finite support regions

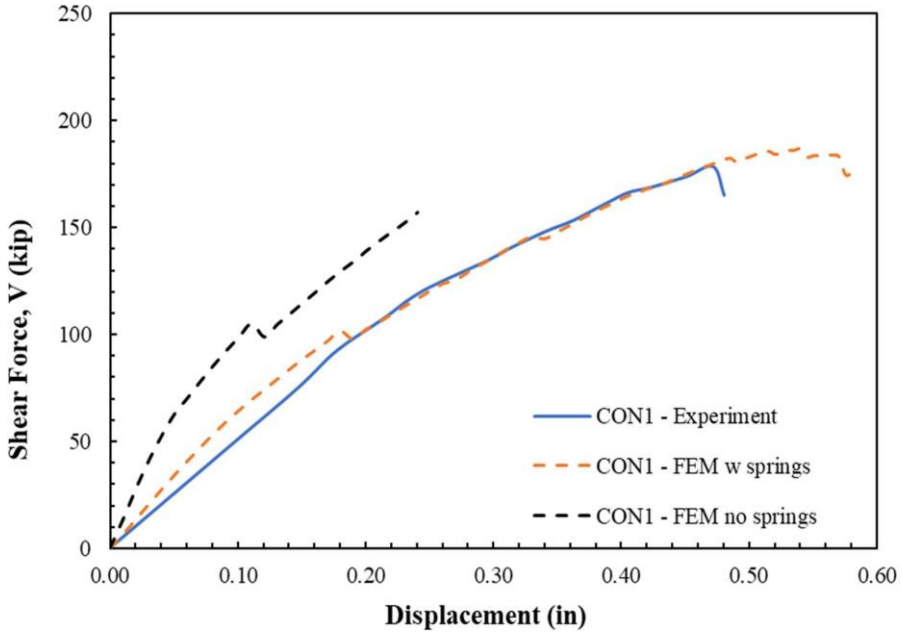

Figure A-2: Comparison of initial stiffness of physical specimen with FE models

FRP-Epoxy Bond Model

There are several established strategies for modeling NSM FRP in concrete elements with varying degrees of complexity and applicability. The approach that requires the most information on the part of the modeler is incorporating a bond law for the NSM. The ATENA software allows for 1D reinforcement elements to have a perfect bond to the surrounding concrete, or perfectly bonded ends and a bond-slip relationship along its embedded length or rely solely on a bond-slip relationship to connect it to the concrete. The ATENA documentation asserts that if a bond-slip relationship is included in the model, the stiffness of the epoxy can be incorporated into the bondslip relationship and therefore does not need to be modeled explicitly around the NSM reinforcement. Obviously, this approach is necessary for reinforcement schemes where debonding is possible, but for instances where debonding is not present, modeling simplifications can be made. There are two different methods to modeling NSM without bonds, one is to embed perfectly bonded 1D reinforcement elements directly into the concrete and the other is to explicitly model the adhesive layer (typically epoxy or mortar) and embed the reinforcement in that element. Since debonding was not expected or observed in this experiment, both perfectly bonded modeling options were tested against the NSM1 experimental results. Figure 5.8 compares the V-D curves for the experiment and the explicit epoxy model ("+epoxy" label) and the model with no epoxy modeled ("no epoxy" label). The initial stiffness of both models matches well with the experimental results, though the no epoxy model is slightly better. The ultimate load of both the no epoxy model and epoxy model was 209 kips, meaning that the differences between these models is negligible. However, as will be discussed in the following paragraph, the model is sensitive to the differences in the mesh between these models meaning there is some small difference between these models.

The general meshing strategy was discussed in a previous section, but the explicit epoxy modeling approach merits some further discussion. By including accurate groove sizes and distinct macro-elements for the epoxy, it is impossible to maintain a consistent mesh size unless a mesh size equal to the groove size is used. Since the selected mesh size is not the same size as the groove, explicitly modeling the epoxy creates a non-uniform mesh which may have implications for the overall accuracy of the results, these meshes are shown in Figure 5.9. To verify this, the V-D curve

for the CON 1 specimen is compared to a uniform 2-inch mesh and the mesh used for the NSM 1 +epoxy model (but with concrete instead of epoxy) in Figure 5.10. In this comparison, the only difference between the models is the mesh, all material properties and reinforcement layouts are the same. The initial stiffnesses of both models are similar to the experiment, but the uniform mesh is slightly better. The ultimate loads for the uniform mesh and NSM mesh are 187 kips and 194 kips which are 4% and 8% over the control specimen, respectively. These differences are larger than the differences observed in the NSM FEM models, meaning that there is a difference between those models, but it is smaller than the differences observed here due to the mesh.